Title
Node-Pore Sensing Techniques for Biomarker Discovery

Author
Li, Brian

Publication Date
2021

Peer reviewed|Thesis/dissertation

Node-Pore Sensing Techniques for Biomarker Discovery

By

Brian Li

A dissertation submitted in partial satisfaction of the

requirements for the degree of

Joint Doctor of Philosophy

with the University of California, San Francisco

in

Bioengineering

in the

Graduate Division

of the

University of California, Berkeley

Committee in charge:

Professor Lydia L. Sohn, Chair

Professor Zev J. Gartner, UCSF

Professor Sarah A. Stanley

Fall 2021

Abstract

Node Pore Sensing Techniques for Biomarker Discovery

By

Brian Lanjing Li

Joint Doctor of Philosophy in Bioengineering

University of California, Berkeley and University of California, San Francisco

Professor Lydia L. Sohn, Chair

Microfluidic technologies have in conjunction with the field of biomedical research for their utility in making highly precise measurements of biological and chemical specimens. These measurements help us search for specific analytes that can be associated with biological states such as disease in a process called biomarker discovery. The analytes in question are the biomarkers of the states they represent, and these associations become part of the greater body of knowledge that guide other researchers in the recognition and study of other biological phenomena. Eventually, this work helps guide clinicians in making diagnostic and prognostic decisions. In this dissertation, I will describe work done to engineer and implement two microfluidic technologies designed to perform biomarker discovery via different modalities, albeit with both analyzing single-cell phenotypes. The first of these devices, called mechano-node-pore sensing, focused on the mechanical properties of cells, and how the mechanics of the cell as a material can reveal information about drug resistance in acute promyelocytic leukemia. The second of these devices instead analyzed cells for surface proteins using a novel scheme for chemical immobilization of antibody probes. In both cases, I demonstrate how mechanical properties and surface proteins can be used as biomarkers to discriminate between cell phenotypes, and how such measurements can help us more deeply understand a variety of biological phenomena, and eventually make advancements in biomedicine.

Table of Contents

Acknowledgements

It goes without saying that this dissertation is not the work of solely one person – countless other people are involved in the support and progression in pursuing a doctoral degree. However complex the network of people may be, I would nevertheless like to more formally recognize several individuals.

First and foremost, I would like to thank my advisor, Professor Lydia L. Sohn. The work finally enclosed in this dissertation and our exciting findings have been a long time coming, propelled by your supervision, mentorship, and enthusiasm. As things here come to an end, I cannot help but feel a sense of satisfaction at what we have accomplished in working together.

I would also like to thank the faculty who served on my dissertation committee and qualifying exam committee: Professors Aaron Streets, Sanjay Kumar, Lin He, Zev Gartner, and Sarah Stanley. Your backgrounds and expertise cover a wide breadth of topics relevant to bioengineering, and it is an honor to have learned from you all. Not to mention – it is no small comfort that the ideas and work enclosed here have all been shaped by your input, helping it to be the best that it can be.

I am grateful to have worked in research groups full of bright and enthusiastic colleagues and mentors. Thank you to all who have taken the time to train me and help me learn over the years: François Rivest, Junghyun Kim, and Olivia Scheideler from my time at the University of California, Berkeley; Professors Jeanne Stachowiak and Tim Yeh at The University of Texas at Austin, and Justin Houser, Ryan Woodall, and Avinash Gadok also from my time at The University of Texas at Austin. Thank you as well to those who worked alongside me in the Sohn Lab: Nahyun Cho, Roberto Falcón-Banchs, Sewoon Han, Thomas Carey, Kristen Cotner, Nate Liu, Molly Kozminsky, Sean Kitayama, Rachel Rex, Andre Lai, and Stephanie Eberly. And thank you to all of the undergraduate students I have had the pleasure of training, teaching, and instructing over the years.

The last people to thank are, of course, my family and friends for their support and encouragement through this time. Above all, I would like to recognize my brother Kris, who is now pursuing his own doctorate in Electrical Engineering at Rice University, perhaps to the chagrin of our very-much-scientist-and-not-engineer parents. It is funny to see how the two of us have made the same decisions in our careers – there are simply too many fun things to learn about to pass up opportunities like these.

Chapter 1: Introduction

In this dissertation, I will describe our efforts to develop microfluidic devices for two applications in biomarker discovery. The term “biomarker” refers to measurable signs of biological activity that can be associated with, or perhaps even more directly linked to, a specific biological state such as disease. The process of biomarker discovery is frequently concerned with identifying and validating these associations so that a biomarker can be reliably exploited for biomedical applications, such as providing diagnostic information or developing targeted therapeutics. In the past few decades, microfluidic technologies have grown to meet a variety of needs in the similarly growing field of biomarker discovery.

For the research described within this dissertation, we constructed microfluidic devices with integrated electronic sensors to track the size, shape, and trajectory of single cells. These devices are part of a class of techniques known as node-pore sensing (NPS). For much of the research discussed, NPS devices included an especially narrow section of microchannel channel such that a cell is deformed when pushed through the device via fluid flow in a technique called mechano-node-pore sensing (mechano-NPS). The cells’ response to this mechanical stress provides a way to study their mechanical properties, which helps us understand the way these cells sense, respond to, and exert forces. This field of study, generally called “mechanobiology,” is concerned with the mechanical processes of living cells such as cell motility (i.e., crawling), or the reorganization of organelles and subcellular structures.

A chief motivation of this dissertation was to explore this research space for mechanical responses associated with a particular biological state – in other words, searching for “mechanical biomarkers.” Indeed, several pieces of prior research have noted that cells undergoing processes like crawling or morphological changes reflect some of the dynamics of the cells’ mechanical properties [1,2]. With this in mind, we chose to investigate one disease in particular: acute promyelocytic leukemia (APL).

This leukemia affects a type of immature blood cell known as a promyelocyte. In normal physiology, promyelocytes are short-lived as they are undergoing hematopoiesis, a process of differentiating naïve blood cell precursor cells into one of several classes of functional blood cells. However, in this disease, a genetic abnormality halts differentiation, causing an accumulation of immature and non-functional immune cells. Past studies have shown that this differentiation can be resumed with a molecule known as all-trans retinoic acid (ATRA); however, not all cells will fully respond to this drug, meaning it may not fully cure a patient of APL [3–7]. Noting that this differentiation process also involves a significant reorganization of these cells’ internal structure, we set out to investigate whether these morphological changes could be sensed with microfluidic probing of cell mechanics, and whether any changes in mechanical properties might reveal why some cells respond to ATRA, and why some do not. To summarize, this research was focused on the discovery of mechanical biomarkers to investigate drug resistance in APL.

In addition to mechanical biomarkers, we developed novel strategies to functionalize microfluidic devices with antibody probes, which we used to assay single cells for surface

protein biomarkers. As a cell's surface is laden with proteins that help reveal the cell's function, it is extremely commonplace to probe these proteins to identify, for example, disease-associated phenotypes. To this end, we developed a microfluidic device wherein cells pass over regions of different antibodies, where these antibodies can be flexibly arranged within the channel to probe for several proteins at once. If a cell contains the protein that one such antibody is specific to, this binding slows the cell's trajectory, which we measure with our integrated electronic sensors. With this, we were able to use our newly developed functionalization strategy and novel microfluidic channel designs to analyze different cell populations for several surface proteins.

Thus, this body of work will explore two different avenues by which we used microfluidic devices to probe for biomarkers. In Chapter 2, I will discuss several theoretical considerations and physical principles that govern the technologies used. In Chapter 3, I will focus on the engineering principles behind the design of the microfluidic devices used, as well as their manufacture, optimization, and operation. I will also discuss how technical variability in these devices affects their performance, especially their odds of producing statistical errors, and how these error rates may affect the reproducibility of research conducted with this technology. In Chapter 4, I will present my findings regarding how APL cells respond to ATRA, and how this process can be sensed by testing the mechanical responses of said APL cells. In Chapter 5, I will present a novel method for immobilizing antibodies in specific geometric patterns inside a microfluidic channel, providing a newly flexible method of screening cells for surface proteins. Finally, in Chapter 6, I will summarize the primary findings from this dissertation and make note of additional, future work that may be undertaken to explore more fully the topics within this dissertation.

1.1 References

1. Rianna, C., Radmacher, M. & Kumar, S. Direct evidence that tumor cells soften when navigating confined spaces. *Mol. Biol. Cell* **31**, 1726–1734 (2020).
2. Urbanska, M. *et al.* Single-cell mechanical phenotype is an intrinsic marker of reprogramming and differentiation along the mouse neural lineage. *Dev.* **144**, 4313–4321 (2017).
3. Douer, D. *et al.* All-trans retinoic acid and late relapses in acute promyelocytic leukemia: Very long-term follow-up of the North American Intergroup Study I0129. *Leuk. Res.* **37**, 795–801 (2013).
4. Puccetti, E. & Ruthardt, M. Acute promyelocytic leukemia: PML/RARα and the leukemic stem cell. *Leukemia* **18**, 1169–1175 (2004).
5. Tallman, M. S. *et al.* All- trans -Retinoic Acid in Acute Promyelocytic Leukemia. *N. Engl. J. Med.* **337**, 1021–1028 (1997).
6. Douer, D. *et al.* High frequency of acute promyelocytic leukemia among Latinos with acute myeloid leukemia. *Blood* **87**, 308–313 (1996).
7. Park, J. H. *et al.* Early death rate in acute promyelocytic leukemia remains high despite all-trans retinoic acid. *Blood* **118**, 1248–1254 (2011).

Chapter 2: A review of the fundamental theory governing the node-pore sensing devices used to study cell mechanical responses

This chapter is chiefly concerned with the operating characteristics of the microfluidic sensors used throughout the presented work. I will first discuss the transport of fluids within microfluidic channels and how this drives the transport of solid particles (e.g., cells). Next, I will describe the physical principles of the electronic measurement used to track the size, shape, and trajectory of cells transiting our microfluidic channels. Last, I will summarize some of the key theory, models, and assumptions about the mechanics of the cells being tested, and how we sense mechanical responses with our microfluidic technology known as mechano-node pore sensing (mechano-NPS).

2.1 A brief overview of key fluid dynamic considerations for microfluidic channels

The flow of viscous fluids through space are most generally described by a set of fundamental partial differential equations known as the Navier-Stokes equations. While these equations describe several phenomena involved in fluid transport, some key characteristics of the flow regimes of microfluidic transport allow us to use a more straightforward and generalized model of fluid transport. As such, in this section, I will summarize some key points that allow us to *approximate* the fluid flow in our channels according to this generalized model.

To start, our microfluidic devices transport aqueous solutions, which are composed of water containing dissolved organic (e.g., proteins) and inorganic (e.g., ionic salts) species and solid-phase particles (e.g., cells). Despite these additions, it is still true that (1) the water is a Newtonian fluid, meaning the shear rate of the fluid is linearly dependent on the applied shear stress via the fluid's dynamic viscosity, and (2) the density of the fluid does not vary in space, meaning the associated flow is incompressible.

Next, a critical feature of microfluidic devices is that the length scale of fluid transport is small – on the order of 0.1 mm or less. The unitless number known as the Reynolds number, Re, is described by the following equation:

$$Re = \frac{\rho v L}{\mu}$$

(Eq. 1)

Which shows that Re depends on the density ρ, velocity v, characteristic length L, and viscosity μ associated with the fluid flow in question. The Reynolds number is often described as a ratio of inertial forces (the momentum associated with a fluid with density ρ moving at a velocity v) to viscous forces (simply the viscosity, μ). For fluid flow with a low Reynolds number (on the order of 10^3-10^4 depending on flow geometry), these inertial forces dominate the flow regime and fluids move in "sheets," hence, the term: laminar flow.

In microfluidic devices transporting aqueous solutions, the fluid properties (density and viscosity) can be estimated or measured, and the flow properties (velocity and characteristic length) depend on the operating characteristics of the device. For our microfluidic devices where characteristic lengths are expected to be 0.1 mm or less, to achieve a Reynolds number of 10^3, the flow velocity associated with water at 20 ºC would be 10 m/s, which far exceeds the expected operating velocity for our devices. As such, the small characteristic lengths of microfluidic devices mean we can expect the fluid flow to be laminar even up to high velocities.

With these key conditions in mind – a Newtonian fluid undergoing incompressible laminar flow – the velocity profile for this kind of flow through a pipe is today described as the Hagen-Poiseuille equation:

$$\Delta \mathrm{P} = \frac{8\mu L Q}{\pi R^4} \qquad \text{(Eq. 2)}$$

Which relates the volumetric flow rate Q generated by a difference in pressure ΔP by the viscosity of the fluid μ, the length of the circular pipe L, and the radius of the circular pipe R. Most importantly, however, we can now assert that the flow of aqueous solutions through a rectangular microfluidic channel follow Hagen-Poiseuille with corrections to account for the geometric differences between a circular and rectangular pipe. As a result, the flow velocity in our devices is predictable, allowing us to compute theoretical expectations of device operation and performance. This flow velocity is also what drives the transport of solid particles such as cells, so this model gives us the capability to understand the trajectory of these particles apart from purely empirical measurements.

2.2 Fundamental principles for the use of four-terminal measurements in node-pore sensing

Often, the resistivity of a material is assessed using one of several impedance measurement techniques. These measurements take many forms, but for our purposes, we will focus on the use of four-terminal measurements. Generally, a four-terminal impedance measurement involves two pairs of electrodes. One is used to apply an electric potential V and are referred to as the force electrodes, while another pair is used to measure an electric current I and are called the sense electrodes (**Fig. 2-01**). The well-known relationship between electric potential and current is described by Ohm's law:

$$V = IR, \qquad \text{(Eq. 3)}$$

Which states that the current, I, through a conducting material is directly proportional to the voltage, V, with this constant of proportionality being known as the resistance R.

This technique has been used to great effect in microfluidic channels to comprise a technology known as resistive-pulse sensing[1]. Here, a four-terminal measurement is performed across a microchannel containing a conductive fluid (in our case, the same aqueous solution under flow conditions). To do this, the positive leads for each electrode pair are placed in a fluid reservoir on one end of the microchannel. At the other end of the microchannel, the corresponding leads for each electrode pair are placed in another fluid reservoir (**Fig. 2-01**). Using these electrode pairs, a four-terminal measurement can be used to measure the current across the channel, based on the relationship between the applied potential and the conductivity of the fluid within[1].

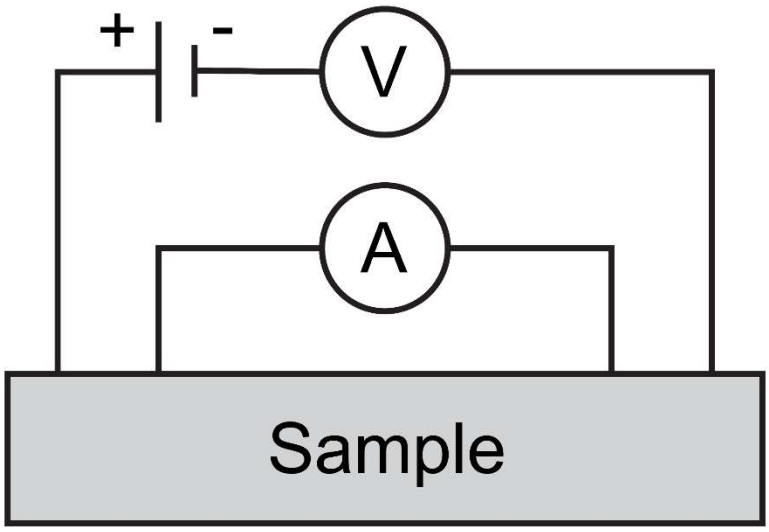

Figure 2-01: An example circuit diagram for a four-terminal measurement. A potential is applied across the two out electrodes, and the current through the sample is measured with an ammeter connected to the two inner electrodes.

A technique called resistive-pulse sensing takes advantage of this microfluidic four-terminal measurement to assess the transit of solid, insulating particles through the microfluidic channel (**Fig. 2-02**)[1]. If one of these particles is of adequate size relative to the channel, it will obstruct the electric field generated by the force electrodes. In such cases, this obstruction causes an increase in the apparent resistivity measured by the four-terminal measurement[1-4]. In our applications, this increased resistivity is measured with the inner electrodes, and manifests as a decrease in electric current. For the case where a solid particle is in motion, the measured current will be at a baseline value while the particle is in the fluid reservoir and not yet obstructing the electric field. The current drops when the particle leaves the reservoir and enters the microchannel, and the current recovers to baseline when the cell reaches the reservoir at the other end. In a plot of current over time, this generates a pulse, where the width of this pulse is dependent on the particle's transit time through the narrow microchannel (**Fig. 2-02**).

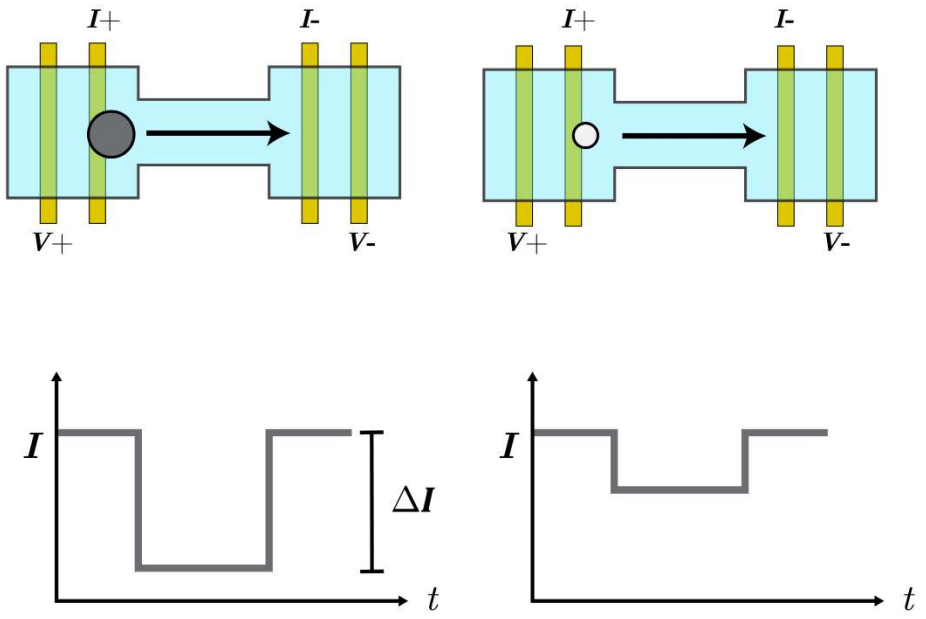

Figure 2-02: Schematic representations of microchannels (top) and current traces (bottom) in resistive pulse sensing. Planar electrodes applying voltage (V) and measuring current (I) are placed in fluidic reservoirs with a substantially larger volume than the microchannel. A larger particle (left) generates a larger current drop (ΔI) than a smaller particle (right).

The degree to which this current decreases, or the amplitude of the aforementioned pulse, is strongly dependent on how much of the electric field is obstructed by the particle, which is obviously a function of the particle's size. Prior work has established a generalized rule for this relationship, and given a spherical particle in a rectangular channel with an effective diameter D_e, the precise diameter of the particle, d, can be determined based on the current pulse amplitude ΔI relative to the baseline current I. This relationship is described by the following equation from Saleh and Sohn, adapted from DeBlois and Bean[1,2]:

$$\frac{\Delta I}{I} = \frac{d^3}{D_e^2 L}\left(\frac{1}{1 - 0.8\left(\frac{d}{D_e}\right)^3}\right) \qquad \text{(Eq. 4)}$$

A newer technique called node-pore sensing (NPS) extends the concepts of resistive-pulse sensing, punctuating single current pulses into several subpulses for a myriad of different applications[5,6]. Node-pore sensing accomplishes this by modulating the microchannel geometry to include widened nodes. These nodes are similar to the reservoirs in the original resistive-pulse sensing concept; the electric field is no longer as substantially obstructed by the solid particle, so the current returns to baseline. In between these widened nodes are pores, or narrow microchannels where the entry of a particle still results in a drop in current. A channel design with a mixture of nodes and

pores generates a series of rectangular subpulses, where the pulse width and amplitude refer to the particle's velocity and size (relative to the pore) in each pore segment (**Fig. 2-03**).

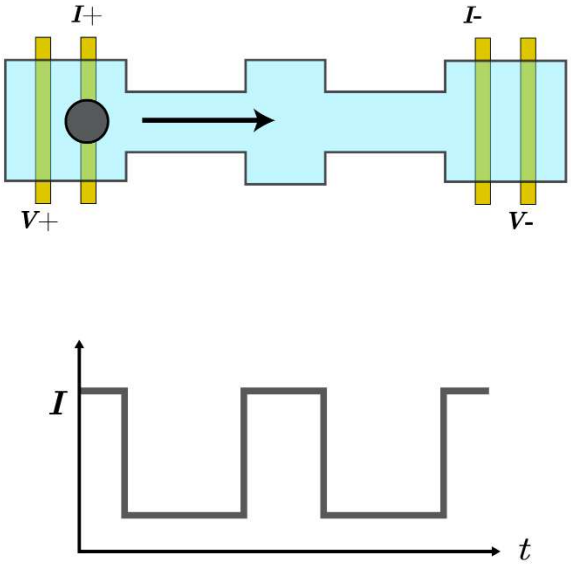

Figure 2-03: Schematic representation of a microchannel (top) and current trace (bottom) in node-pore sensing. A single particle can generate several current subpulses when the microchannel is geometrically modulated to contain narrow sections (pores) and wide sections (nodes). When the particle enters a node, the current returns to baseline.

A key application of node-pore sensing is mechano-NPS, which involves the inclusion of an especially narrow pore segment[7]. This pore is designed to be smaller than the expected diameter of a cell, such that the cell is deformed as the flow field drives it through the contraction. The response of the cell to this mechanical stress reveals information about its mechanical properties, and is the basis for the mechanical biomarker discovery discussed later in this dissertation.

2.3 Mechanics of cells undergoing deformation in microfluidic channels

As much of the work in this dissertation is concerned with the mechanical properties and responses of single cells, this section is devoted to providing the theoretical background needed to understand some of the mechanical phenomena at play. Cells contain a mixture of solid-phase and liquid-phase components, and so the mechanical properties of cells necessarily include characteristics of both solids and liquids. For solids, the simplest way to describe how materials respond to deformations is by approximating them to be linear elastic[8]. For fluids, the intrinsic property that defines deformation under shear is called viscosity[9]. Cells, like all materials expected to have solid-like and fluid-like components to their mechanical properties, are described by a combination of both components in a general model called viscoelasticity[10].

A key difference between linearly elastic solids and purely viscous fluids is that such a solid will only experience deformation so long as mechanical stress is applied. If this applied stress is held at a certain level, the solid will maintain a constant degree of deformation, or strain. This is not the case for fluids, whose *rate* of deformation under a certain stress is described by viscosity. If a non-zero degree of shear stress is constantly applied to a fluid, that fluid will *continuously* deform according to a quantity called the shear rate, which is linked to the applied shear stress by the fluid's viscosity.

In a viscoelastic material, both elastic and viscous behaviors occur when a stress is applied. A key result of this mixed behavior are the phenomena known as stress relaxation and creep, though for our purposes, we will focus on creep. In solid polymers, such as the fibrous and helical proteins that comprise a cell's cytoskeleton, the application of some mechanical stress will see an immediate strain response according to the material's intrinsic elasticity[10]. However, both individual polymer molecules and groups of polymer molecules can rearrange after a stress is applied; this molecular-scale rearrangement occurs over time and means the strain will not be constant even if the applied stress is held constant. This change in strain over time under a constant stress is a property of fluids, but for viscoelastic materials, is appropriately called viscoelastic creep[10].

Numerous other microfluidic techniques have been used to measure the time-dependent deformation of single cells, applying both compressive and tensile stresses and estimating the mechanical properties of cells based on their apparent propensity to deform[11-13]. Apart from the use of optical stretchers, most of these techniques lacked a model for viscoelastic behavior, or the capability to measure cells over long timescales, or both[11-14]. Mechano-NPS addresses this latter shortcoming, although work by Kim *et al*. simplified the measurement of viscoelastic creep to a categorical classification, rather than a quantitative model[7]. To remedy this, used a relatively simple model of viscoelastic creep to describe this behavior in our measurements of single cells. This model, called the Kelvin-Voigt model, assumes that the elastic and viscous components of the material experience the same strain. Because strain occurs instantly in the elastic component but occurs over time in the viscous component, it can be described as a first-order, linear differential equation dependent on the applied stress:

$$\sigma(t) = E\varepsilon(t) + \eta \frac{d}{dt}\varepsilon(t) \qquad \text{(Eq. 5)}$$

Where $\sigma(t)$ is a function describing stress, E is the elastic modulus, $\varepsilon(t)$ is a function describing strain, and η is the viscosity. Thus, the stress depends on both the strain in the elastic component of the material, as well as rate of change in strain in the viscous component of the material.

In our prior example of creep, several different molecules (*e.g.*, collagen, elastin) rearrange after a stress is applied; we can approximate this as a step (sudden) change in stress, such that $\sigma(t)$ is constant at σ_0 for all t after a time t_0. We also make the

assumption that under viscoelastic creep the strain eventually reaches a steady-state value, ε_∞, which would ostensibly be zero if σ_0 were zero, and the material is no longer experiencing a mechanical stress. The solution to the above differential equation given the above is:

$$\varepsilon(t) = \frac{\sigma_0}{E}[1 - \exp(-t/\tau)] + \varepsilon_\infty$$

(Eq. 6)

Note that this solution informs us that the strain will start at an initial value exactly as it would if the material were linearly elastic. The strain will then exponentially decay at a rate defined by the time constant, τ, to the steady-state value we mentioned above (ε_0). This time constant, interestingly, is simply the ratio of coefficients for the two strain terms in Eq. 3: η/E. As such, the rate at which the strain decays to its steady state value is dependent on the relative contributions of elastic vs. viscous forces in the material.

This model is relevant to our research because it can be used to describe the mechanical behavior of cells in our mechano-NPS devices. In mechano-NPS, the microfluidic channel is designed to apply a target strain to a cell as it transits the contraction segment. The behavior of the cell in this contraction has been previously described but is approximated to be a property of the cell's elastic modulus (*i.e.*, viscous forces are not in consideration)[7]. This modulus governs the cell's response to this deformation; a cell with a greater elastic modulus, or stiffness, will transit this contraction more slowly than a cell with a lower elastic modulus. This effect is primarily driven by the friction between the cell's surface and the channel walls (**Fig. 2-04**).

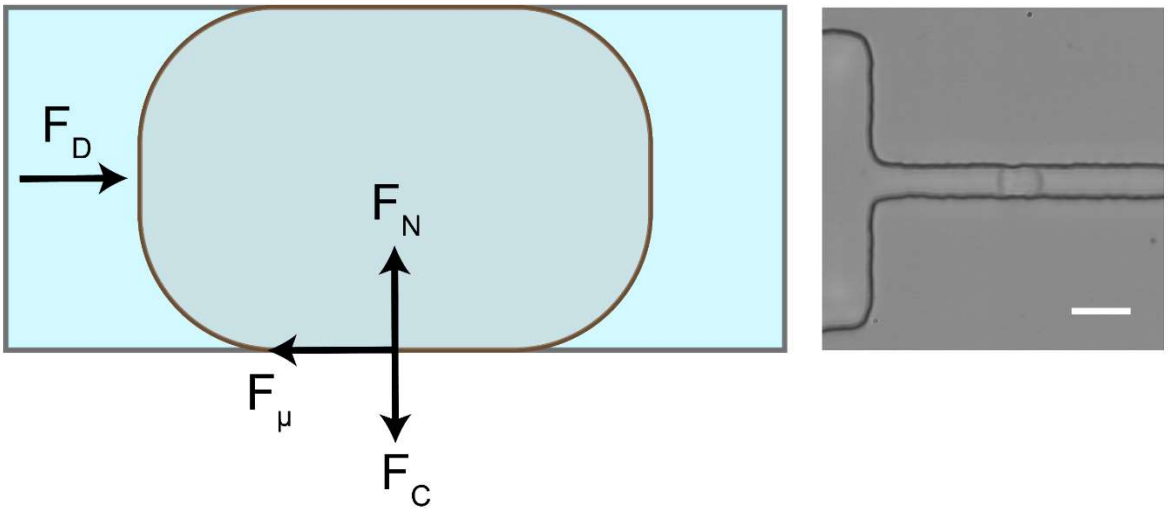

Figure 2-04: Left: free body diagram of a cell transiting a narrow contraction in mechano-NPS. The driving pressure propels the cell in the direction of flow (F_D). This force is opposed by wall friction (F_μ), which results from the normal force (F_N) acting against the cell's compressive force (F_C), which itself arises from the cell's internal stress acting on the wall. Right: high-speed microscopy image of a cell transiting a mechano-NPS contraction segment. Scale bar represents 25 μm.

In this case, the force due to friction F_μ acts opposite to the cell's direction of travel, and is classically dependent on the coefficient of friction, μ, and the normal force, F_N in the following equation:

$$F_\mu = \mu F_N. \quad \text{(Eq. 7)}$$

In this system, the normal force acts in a direction orthogonal to the plane in which the cell surface and channel walls are in contact, and opposite in magnitude and direction to the force applied by the cell surface to the wall while the cell is compressed. The magnitude of the normal force, then, is simply the product of the internal stress due to compression and the area of surface contact. The internal stress is difficult to calculate, but as both the stress and elastic modulus are of the same units, we know the stress *depends* on the elastic modulus of the cell. As such, the magnitude of the normal force is related to the elastic modulus. Since the area of surface contact will vary with cell size, this method of measuring a cell's transit time through a narrow contraction is also highly dependent on cell size. Accordingly, a unitless number called the whole-cell deformability index (*wCDI*) was developed by Kim *et al.* to both describe this behavior, and account for differences in length scale[7]. This is defined as:

$$wCDI = \frac{l_c}{u_{flow} \times h_{chann}} \times \frac{d_{cell}}{t_{cont}}$$

(Eq. 8),

where l_c is the length of contraction segment, u_{flow} is the cell's velocity in the pore before the contraction segment, h_{chann} is the height of the contraction segment, d_{cell} is the cell's initial diameter, and t_{cont} is the transit time through the contraction segment.

While a cell's elastic response is described by the *wCDI*, its viscoelastic response is described by the rate at which creep occurs. In mechano-NPS, after a cell transits the narrow contraction, it enters a series of wider pores and nodes that form the recovery segments of the device. As such, the aforementioned wall-to-wall contact force is abruptly removed, constituting a step change in stress (**Fig. 2-05**). As we described earlier, this step change in stress is associated with an exponential decay in strain. This exponential decay manifests in the cell as a gradual recovery of cell shape and size from an ellipsoid back to a sphere (**Fig. 2-06**).

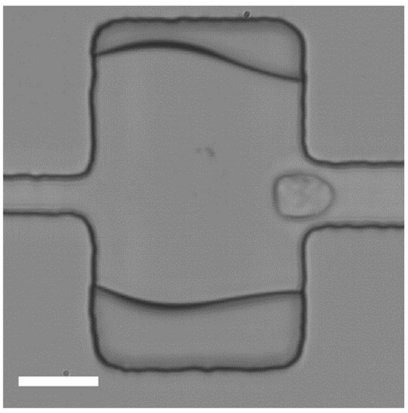

Figure 2-05: High-speed microscopy image of a deformed cell entering a mechano-NPS recovery segment, which is designed to allow the cell to recover to its original shape. Scale bar represents 25 μm.

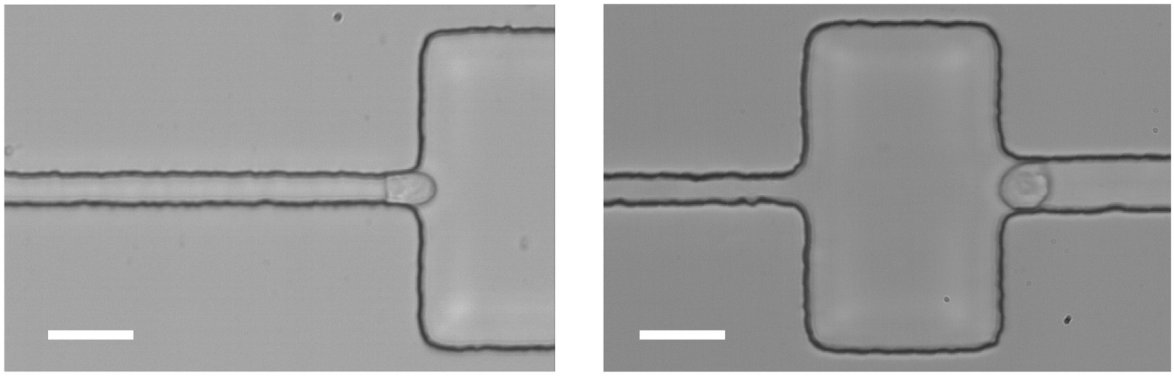

Figure 2-06: High-speed microscopy images of (left) a cell with its leading edge deformed into an ellipsoid while exiting a mechano-NPS contraction segment, and (right) another cell fully recovered to its original spherical shape after deformation. Scale bars represent 25 μm.

As the current drop in an NPS device depends on cell size, so too can the cell shape be measured via the magnitude of current drop. In our measurements, the current drop from a deformed cell is less than that of a spherical cell. As described above in Eq. 6, the cell strain will relax to a steady-state value according to the exponential decay model derived from Kelvin-Voigt. A transform of variables from the stress-strain space to the voltage-current space gives the following equation governing the measurement of this viscoelastic creep in mechano-NPS:

$$\Delta I(t) = \Delta I_0[1 - \exp(-t/\tau)] + \Delta I_\infty \quad \text{(Eq. 9)}$$

where ΔI is equivalent to a difference in current from the baseline: $I_{baseline} - I(t)$, ΔI_0 is the current drop associated with a cell at the time of release from the contraction channel, and ΔI_∞ is the current drop associated with a cell at its steady-state strain after complete

relaxation. Rewriting Eq. 9 as a function of measured current rather than current drop yields:

$$I(t) = I_0 \exp(-t/\tau) + I_\infty \quad \text{(Eq. 10)}$$

where $I(t)$ is the measured current over time after the step change in stress, I_0 is the current associated with the cell at the time of release from the contraction channel, τ is the time constant of the exponential decay in voltage, and I_∞ is the current associated with the cell at its steady-state strain after complete relaxation. Mechano-NPS subpulses produced after the cell exits the contraction channel provide values for $I(t)$ and t to which we fit a linear model to estimate τ via least squares regression (**Fig. 2-07**). Since τ is simply the ratio of viscosity to elasticity, this method allows us to quantify the relationship between viscous and elastic forces in this viscoelastic creep model.

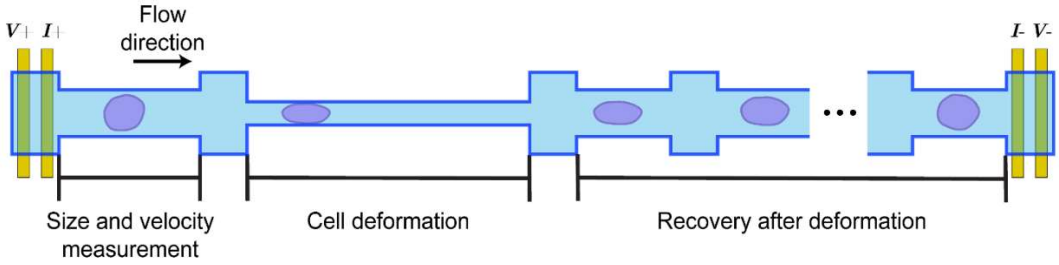

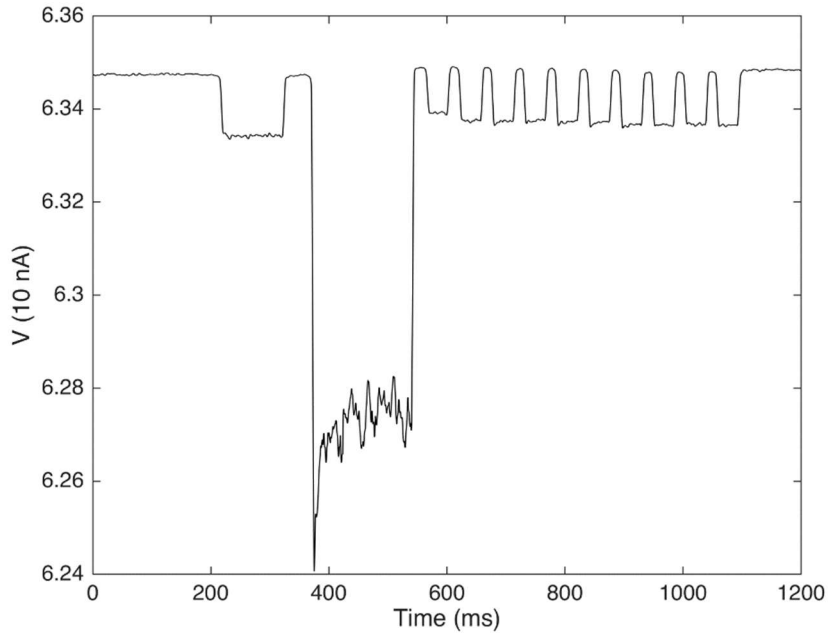

Figure 2-07: (Top) Schematic of mechano-NPS microchannel, including a segment for measuring cell size and velocity, a contraction segment, and a series of recovery segments. After it leaves the contraction channel, the cell recovers from an ellipsoid shape to a sphere. (Bottom) Current pulse (amplified and converted to voltage) resulting from a cell transiting a complete mechano-NPS channel. The subpulse with the largest amplitude is generated when the cell transits the contraction segment. The series of short subpulses immediately following the contraction subpulse are generated as the cell transits each recovery segment. These subpulses gradually increase in amplitude due to viscoelastic creep.

2.4 Concluding thoughts

Overall, the contents of this chapter serve to contextualize the operating principles of the node-pore sensing devices used throughout this dissertation. The equations, models, and laws listed are especially important for Chapter 3, where I will describe critical design parameters of NPS devices, which are governed by the theory in Chapter 2. This same theory is critical for understanding how to test, calibrate, and practically apply node-pore sensing devices to pursue the research questions described in Chapters 4 and 5.

2.5 References

1. Saleh, O. A. & Sohn, L. L. Quantitative sensing of nanoscale colloids using a microchip Coulter counter. *Rev. Sci. Instrum.* **72**, 4449–4451 (2001).
2. DeBlois, R. W. & Bean, C. P. Counting and sizing of submicron particles by the resistive pulse technique. *Rev. Sci. Instrum.* **41**, 909–916 (1970).
3. Kubitschek, H. E. Electronic Counting and Sizing of Bacteria. *Nature* **182**, 234–235 (1958).
4. DeBlois, R. W. *et al.* Electrokinetic measurements with submicron particles and pores by the resistve pulse technique. *J Colloid and Interface Sci* **61**, 323-335 (1977).
5. Balakrishnan, K. R. *et al.* Node-pore sensing: a robust, high-dynamic range method for detecting biological species. *Lab Chip* **13**, 1302 (2013).
6. Balakrishnan, K. R. *et al.* Node-Pore Sensing Enables Label-Free Surface-Marker Profiling of Single Cells. *Anal. Chem.* **87**, 2988–2995 (2015).
7. Kim, J. *et al.* Characterizing cellular mechanical phenotypes with mechano-node-pore sensing. *Microsystems Nanoeng.* **4**, 1–12 (2018).
8. William D. Callister, D. G. R. *Materials Science and Engineering.* (Wiley, 2014).
9. Munson, B. R., Okiishi, T. H., Huebsch, W. W. & Rothmayer, A. P. *Fundamentals of Fluid Mechanics*. (Wiley, 2013).
10. Park, J. & Lakes, R. S. *Biomaterials*. (Springer, 2007).
11. Guck, J. et al. Optical deformability as an inherent cell marker for testing malignant transformation and metastatic competence. Biophys. J. 88, 3689–3698 (2005).
12. Mietke, A. et al. Extracting Cell Stiffness from Real-Time Deformability Cytometry: Theory and Experiment. Biophys. J. 109, 2023–2036 (2015).
13. Byun, S. et al. Characterizing deformability and surface friction of cancer cells. Proc. Natl. Acad. Sci. U. S. A. 110, 7580–7585 (2013).
14. Gossett, D. R. et al. Hydrodynamic stretching of single cells for large population mechanical phenotyping. Proc. Natl. Acad. Sci. U. S. A. 109, 7630–7635 (2012).

Chapter 3: A perspective of the engineering principles involved in applying microfluidic technologies to probe cell mechanics

This chapter is, in part, a postprint of the following journal article:

> Brian Li, Kristen L. Cotner, Nathaniel K. Liu, Stefan Hinz, Mark A. LaBarge, Lydia L. Sohn. Evaluating sources of technical variability in the mechano-node-pore sensing pipeline and their effect on the reproducibility of single-cell mechanical phenotyping. *PLoS ONE* **16**, e0258982 (2021).

While the previous chapter discussed several theoretical considerations surrounding the mechano-node-pore sensing devices used in our research, this chapter will instead explore the practical implementation of this technology from an engineering perspective. First, I will review some of the critical design parameters and considerations for mechano-NPS. Second, I will describe the manufacturing process for these devices, and the importance of these process controls on device performance. Third, I will discuss how these devices are tested and calibrated, and how such work guides the design iteration process. Fourth, I will provide an overview of how raw data traces from mechano-NPS devices are conditioned, processed, and analyzed so that we can interpret a cell's response to an applied deformation. Last, I will show results from specific experiments that we performed to evaluate how technical variability can affect the reliability of our technology and the reproducibility of the results that it generates.

3.1 Critical design parameters for mechano-node-pore sensing

As described in Chapter 2, both the fluid flow and signal amplitude in a node-pore sensing device depend on the geometry of the microchannel. Consequently, the design of a mechano-NPS is most principally concerned with matters of microchannel geometry.

These microchannels are made by way of soft lithography, a process where photolithographic patterning of a negative-tone epoxy photoresist called SU-8 (MicroChem) is used to make relief masters, which are in turned used to embed a microchannel in polydimethyl siloxane (PDMS) (Sylgard 184, Dow Corning), a silicone rubber. For this process, PDMS a liquid pre-polymer base is mixed with a curing agent, which sets the polymer into an elastomeric solid. After curing the PDMS, it is peeled from the relief master, which leaves the microchannel pattern in the now-solid silicone.

In this process, the primary method of controlling channel geometry is in the photolithographic patterning of SU-8. The length and width of microchannel features are set according to a photomask, as is standard in any photolithographic process (**Fig. 3-01**). In designing a photomask for mechano-NPS, it is important to consider the expected size of the cells to be analyzed. The pores of the channel must be small enough for cells to cause an adequately large drop in current, but not so small that any cells are deformed before reaching the contraction segment, or that the cells lack the space to fully recover to their undeformed shape after exiting the contraction segment. Conversely, the contraction segment must be of a width such that cells experience a particular strain rate;

for example, in work by Kim *et al.*, mechano-NPS channels were designed to deform cells by approximately 30% of their starting diameter. The length and width of the nodes must also be adequately large such that the current fully returns to baseline when a cell is not in any pore.

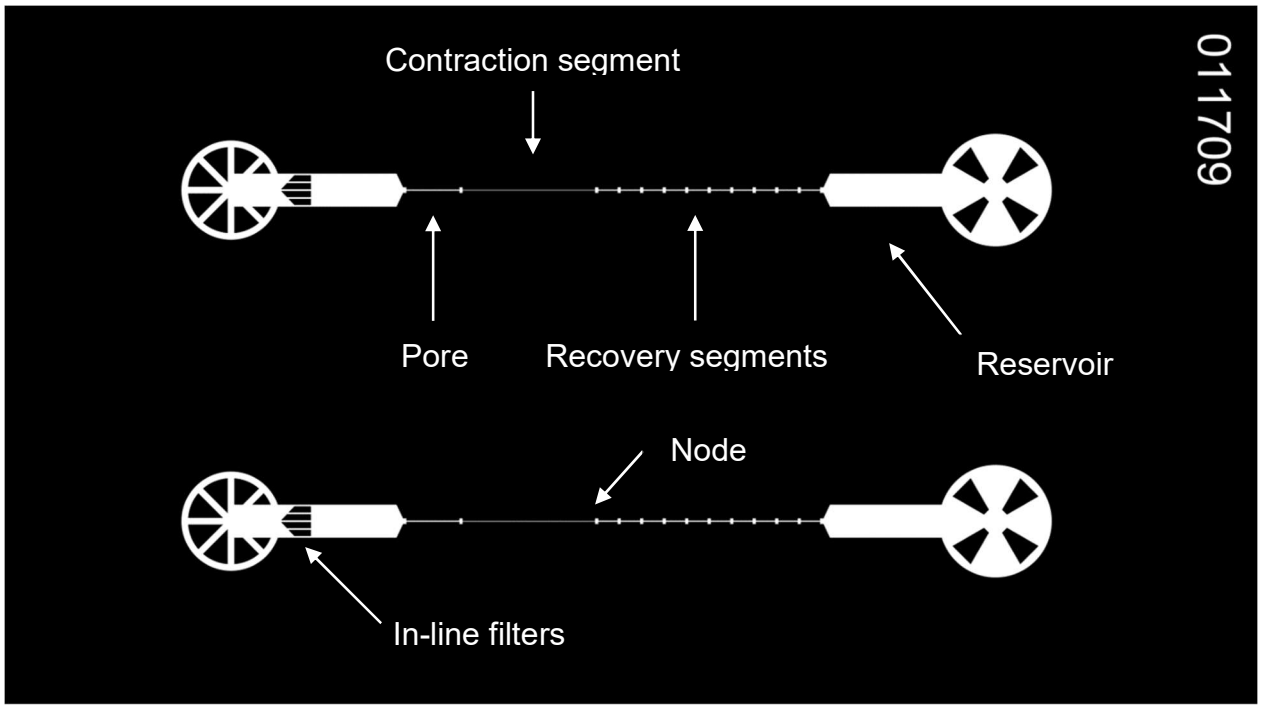

Figure 3-01: Example schematic of a photomask for a single mechano-NPS device with two identical channels containing one reference pore, one contraction segment, and ten recovery segments. White regions allow UV light to pass, whereas black regions block UV light. A stamp with wafer location, pore width, and contraction channel width is included in the device as identifying information when the device is viewed under a microscope. The numerical stamp in the northeast corner is a series of two-digit codes that, in order, describe the device location on the wafer, the pore width in microns, and the contraction segment width in microns. Nodes are 85 μm wide and 50 μm long. For this example, the pore is 800 μm long and 17 μm wide and the contraction segment is 2000 μm long and 9 μm wide. The series of 10 recovery node-pore pairs maintain the same node dimension, but each pore is 290 μm long and 17 μm wide. Reservoirs were 0.5 mm wide, and include in-line filters with a pore size of 20 μm.

While the overall length of the channel is not a critical dimension, a longer channel will have a greater baseline resistance and thus reduce the amplitude of an NPS subpulse. To this end, we chose to use a single pore to measure a cell's starting size and velocity and a single contraction segment to apply deformation to limit the channel's overall length. To measure cell recovery, we included 10 node-pore pairs to track a cell's size over time. Together with minimally short nodes that ensure full recovery of the current to the baseline, our 10 recovery segments provided enough information to reliably calculate the rate of viscoelastic creep in recovering cells.

3.2 Fabrication and manufacturing processes for mechano-node-pore sensing microfluidic devices

As mentioned above, mechano-NPS microchannels are manufactured using a standard soft lithography process (**Fig. 3-02**). More specifically, negative relief structures are fabricated onto polished silicon wafers using SU-8 3000-series epoxy resist. The resist is first poured onto the wafer, then spun to coat a silicon wafer a thin film of resist. The film for one class of mechano-NPS devices used for smaller cells (mean diameter of 10 μm) involved spin-coating of SU-8 3010 at 1850 RPM, yielding a film thickness of 12.9 μm as measured by contact profilometry. For mechano-NPS devices meant for larger cells (mean diameter of 16 μm), SU-8 3025 was spun at 2950 RPM for 60 seconds, yielding a film thickness of 22.3 μm. This film is then baked at 95 °C for several minutes to evaporate the majority of the carrier solvent, depending on the relative concentration of SU-8 solids and thickness of the film. This soft bake was 8 minutes for the SU-8 3010 film, and 11 minutes for the SU-8 3025 film. The resist-coated wafer is then exposed to UV light through a Mylar transparency photomask, with the dose also depending on the resist and film thickness. The UV dose used was 170 mJ/cm^2 for the SU-8 3010 film, and 200 mJ/cm^2 for the SU-8 3025 film. For SU-8 exposed to the UV dose, the resist begins to cross-link, which is accelerated with a post-exposure bake at 95 °C, where the length of this thermal step is again dependent on the film thickness. This post-exposure bake was 4 minutes for both SU-8 3010 and 3025 films. Finally, the entire wafer is immersed in SU-8 developer to remove the resist that was not crosslinked (not exposed to UV). SU-8 3010 films were immersed in developer for 3 minutes, whereas SU-8 3025 films were immersed in developer for 4 minutes. After rinsing and drying by baking at 120 °C for 3 minutes, the silicon wafer is left with SU-8 features that comprise the relief master for mechano-NPS microchannels.

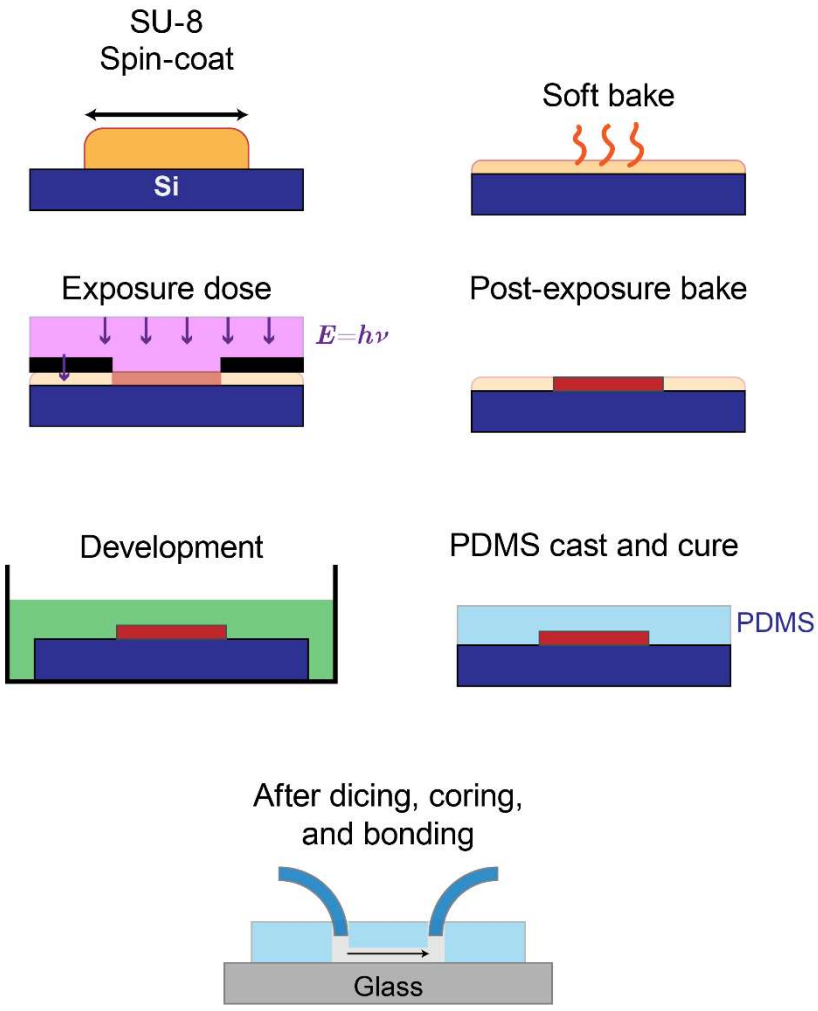

Figure 3-02: An overview of the process of constructing a PDMS-on-glass microfluidic device.

To form these microchannels, PDMS pre-polymer and curing agent are thoroughly mixed at a 9:1 ratio before being poured onto the wafer containing microchannel relief masters. After curing the liquid PDMS for 2 hours at 85 °C, solid PDMS slabs with the embedded microfluidic channels are peeled from the relief masters, cut according to device dimensions, and cored with a 1.5 mm biopsy punch to provide input/output access to the microchannel.

The other primary feature of mechano-NPS devices are the planar metal electrodes, which we pattern on glass substrates for bonding to PDMS devices. Platinum (Pt) and gold (Au) electrodes are fabricated using a lift-off process with electron-gun evaporation for metal deposition. The Pt electrodes and Au contact pads were patterned onto glass slides using a photolithographic process for S1813 positive-tone resist. To accomplish this, S1813 resist was poured onto glass slides and spun at 3000 rpm. After spin-coating, the glass slide is soft-baked at 100 °C for 1 minute to evaporate latent solvent. The glass was then exposed to UV light at a dose of 300 mJ/cm^2 through another Mylar

transparency photomask defining the electrodes. Resist exposed to UV was removed from the glass slide by immersing the substrate in MF-321 developer. A thin metal film consisting of 75 Å Ti, 250 Å Pt, and 250 Å Au was then deposited onto the patterned glass slides using electron-gun evaporation. Lift-off was finally accomplished by dissolution of the remaining photoresist with acetone, which also removed the metal from the glass slide except for where the S1813 had previously been exposed to UV and developed away. As such, the only metal remaining on the glass slides form the Pt/Au electrodes used to perform a four-terminal measurement within a node-pore sensing microchannel.

For final assembly, the glass slides containing electrodes and the molded PDMS devices were simultaneously treated with oxygen plasma (2 minutes, 450 mTorr, 30 W, Harrick Plasma) before being bonded together and baked at 125 °C for 5 minutes, finally yielding complete node-pore sensing devices (**Fig. 3-03**).

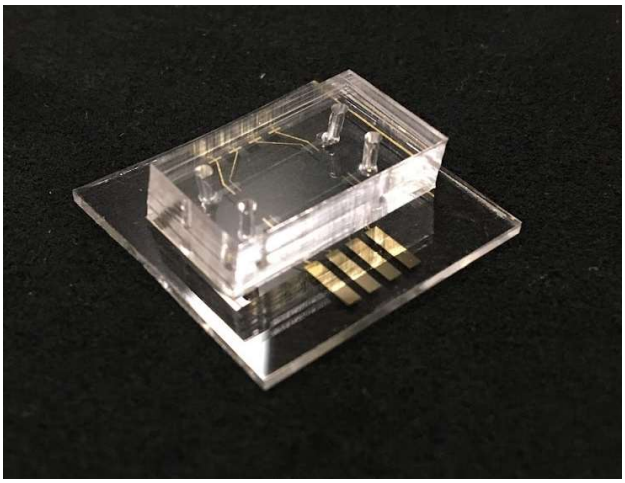

Figure 3-03: Photograph of a mechano-NPS device, with microchannels embedded in PDMS and Pt/Au electrodes patterned on a 2.5 cm x 2.5 cm glass substrate.

3.3 Calibration and testing of mechano-node-pore sensing devices

As was mentioned in Chapter 2, the degree to which the current drops in a resistive-pulse (or node-pore) sensor is dependent on the relative size of the particle compared to the microchannel. Work by DeBlois and Bean established an empirical model to determine the size spherical particles in circular pores based on resistive-pulse amplitudes [1]. This model was later demonstrated by Saleh and Sohn to also be appropriate for performing similar measurements on spherical particles in rectangular pores, highlighting a characteristic effective diameter that can be used in place of the circular diameter of a pipe [2]. While mechano-NPS is concerned with both subpulse duration (in the measurement of *wCDI*) and amplitudes (in measuring cell size and cell recovery), larger signal amplitudes (*i.e.*, signal-to-noise ratio) make it easier to identify cell events in the current measurement.

To determine this characteristic effective diameter (D_{eff}), we calibrated mechano-NPS channels with polystyrene spheres with a manufacturer-specified mean and coefficient of variation (C.V.) for the particle diameter. We then measured the amplitudes of several pulses generated by these polystyrene spheres transiting a mechano-NPS channel with a particular geometry. We used the following equation derived from previous work by Saleh and Sohn[1–3]:

$$\frac{\Delta I}{I} = \frac{d^3}{D_e^2 L}\left(\frac{1}{1 - 0.8\left(\frac{d}{D_e}\right)^3}\right)$$

(Eq. 1)

Which describes the relationship between the current drop ΔI relative to the baseline current I and the particle diameter d, channel length L, and aforementioned effective diameter D_e. By measuring ΔI and I, designing a particular length L, and knowing both the mean value and uncertainty for d, we can compute D_e.

Having determined this critical parameter that permits accurate sizing of spherical particles in a mechano-NPS device, we can now use these devices to find an accurate average diameter for a population of cells, and thus select an optimal device design. To this end, after the basic mechano-NPS design (described above) was decided upon, a "panel" was designed to vary pore width from 13 μm to 21 μm, as well contraction segment widths ranging from 7 μm to 13 μm. The use of supporting tools such as a hemacytometer and microscope, or commercial Coulter counters for cells (*e.g.*, the Millipore Scepter 2.0 Handheld Automated Cell Counter) to estimate the diameter of a cell in suspension can help narrow the selection of devices from this panel.

A cell population is then analyzed with several identical mechano-NPS devices to find a sample mean and standard deviation for cell size, as well as quantify the normalized

current drop, $\Delta I/I$. We will discuss the latter in more detail in the next section, but to accomplish the former, assuming a coefficient of variation of 10%, a 95% confidence interval calculated from 100 analyzed cells will be approximately 0.4 μm wide. Using the sample mean $\bar{x}$ and standard deviation σ from those 100 cells, we can compute a probability distribution function for cell diameter. If this distribution is sufficiently close to normal according to a Lilliefors test, then 97.7% of cells will be smaller than $\bar{x} + 2\sigma$. As such, we set a criterion that the pore width of a mechano-NPS should be at least as wide as $\bar{x} + 2\sigma$ for a particular cell population. While this means 2-3% of cells may contact the channel walls before entering the contraction segment, any such events can be easily recognized by calculating the cell diameter from $\Delta I/I$ and Eq. 1, then discarded, if desired. Following this process, the appropriate channel size can be selected for a wide variety of cell types, ranging from leukocytes (9 μm) to epithelial cells (17 μm).

3.4 Conditioning, processing, and analysis of raw current traces

The extraction of mechanical information from cells analyzed by mechano-NPS is accomplished by quantifying the amplitude and width of current subpulses. The instrumentation used to acquire these data consist of a custom printed-circuit board, a Keysight E36311A digital power supply (or equivalent), a DL Instruments 1211 current preamplifier (or equivalent), and a National Instruments PCIe-6351 DAQ to transmit data to a desktop computer. To improve signal-to-noise ratio, Kim *et al.* developed a pipeline of data conditioning to make it easier to process and analyze current pulses[3] (**Fig. 3-04**).

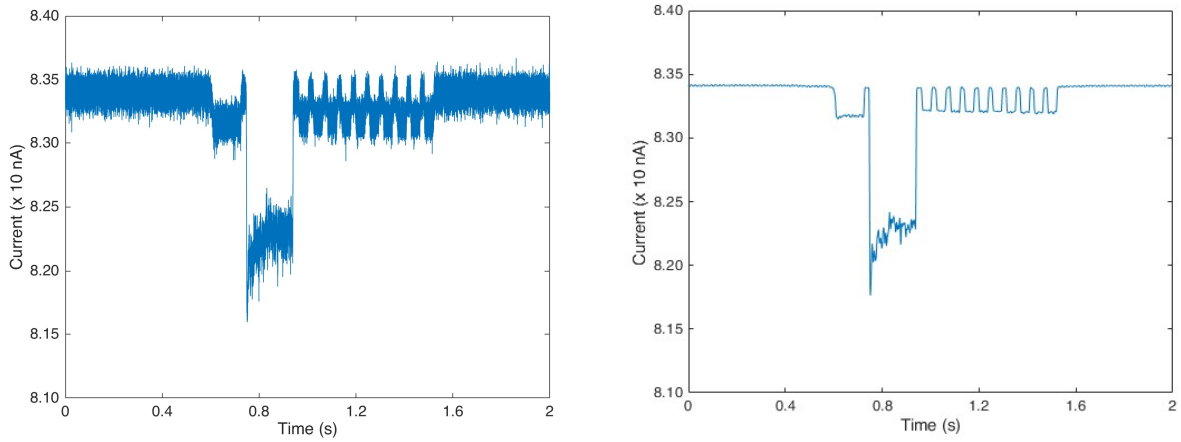

Figure 3-04: Unfiltered mechano-NPS current pulse (left) and the same current pulse after low-pass filtering (right).

Because the subpulses are relatively low-frequency (< 100 Hz for cell velocities on the order of 10 mm/s), the noise can be easily reduced by an order of magnitude (**Fig. 3-04**). To then find the edges of rectangular subpulses, we can approximate the first derivative of the signal by taking the element-wise difference and searching for local maxima, which align with the step changes from the rectangular current subpulses. Even for the low-pass filtered signal, the difference vector is extremely noisy; however, the signal-to-noise ratio can be improved by resampling the signal before the element-wise difference is calculated (**Fig. 3-05**). Performing this resampling step massively improves the contrast

between subpulse-associated peaks and the noise floor and allows for precise quantification of subpulse durations.

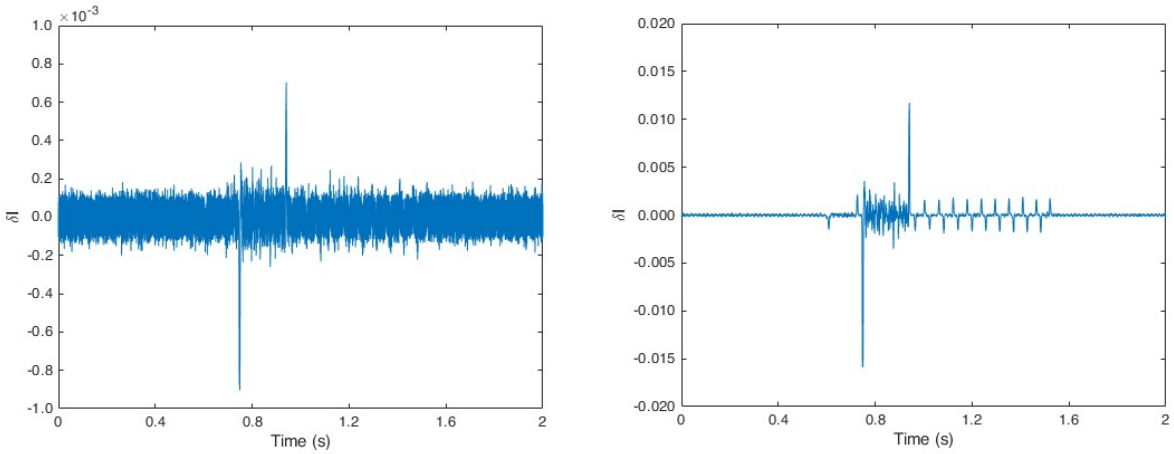

Figure 3-05: Element-wise difference of a low-pass filtered mechano-NPS current pulse (left) and the element-wise difference of the same current pulse that was first resampled from 50 kHz to 2.5 kHz (right).

The amplitudes of these peaks depend on the degree of current drop in the pulse itself. We found that, for the difference vector, a minimum δI peak of 2×10^{-4} is adequate to reliably find subpulse boundaries and quantify transit times, which corresponds to a $\Delta I/I$ in the current pulse of approximately 4×10^{-3}. However, as I may change over time due to baseline fluctuations, the current pulse itself is detrended via asymmetric least-squares smoothing after subpulse boundaries are found (**Fig. 3-06**)[4]. From this detrended signal, the current drop for each subpulse can be easily found.

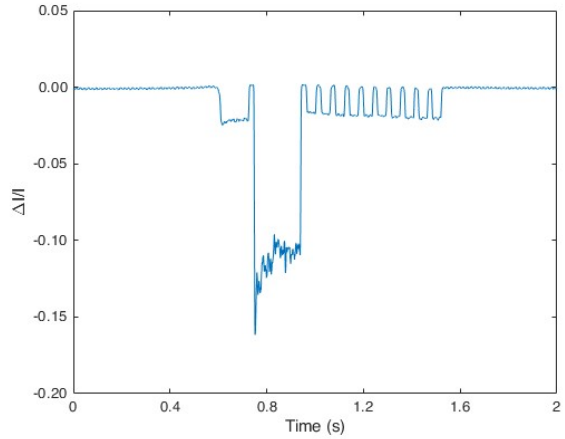

Figure 3-06: Mechano-NPS current pulse detrended with asymmetric least-squares smoothing.

Having quantified the durations and amplitudes of each subpulse in the mechano-NPS signal, we can then derive mechanical information from these data. The amplitude of the first subpulse is used to find the size of the cell prior to deformation using Eq. 1. Since the lengths of each pore are known, we can additionally use the duration of the first and

second subpulse, which are the cell's transit times through the reference pore and contraction segment, respectively, to find the respective velocities through these pores. From this information, we can calculate *wCDI*[3]:

$$wCDI = \frac{l_c}{u_{flow} \times h_{channel}} \times \frac{d_{cell}}{t_{cont}}$$

(Eq. 2)

where v_c is the cell's velocity in the contraction segment, v_0 is the cell's velocity in the reference pore, d_0 is the cell's initial diameter, and h is the height of the channel. The remaining subpulses pertain to the calculation of recovery time, which is accomplished using the model described in Chapter 2:

$$I(t) = I_0 \exp(-t/\tau) + I_\infty$$

(Eq. 3)

3.5 Evaluating the repeatability and reproducibility of results drawn from mechano-node-pore sensing analysis

This section is, in part, a postprint of the following journal article:

> Brian Li, Kristen L. Cotner, Nathaniel K. Liu, Stefan Hinz, Mark A. LaBarge, Lydia L. Sohn. Evaluating sources of technical variability in the mechano-node-pore sensing pipeline and their effect on the reproducibility of single-cell mechanical phenotyping. *PLoS ONE* **16**, e0258982 (2021).

3.5.1 Introduction

As cells frequently generate and experience a variety of forces in normal physiology, their mechanical properties are an important aspect of their function. Cell mechanical properties are implicated in many diseases, including metastatic cancer and a variety of laminopathies [5,6]. More recently, there has been increasing research on the use of "mechanical phenotyping" to identify and screen single cells for mechanical properties associated with malignancies [3,7,8]. In this work, we focus specifically on the use of mechano-NPS to analyze cells from breast epithelial tissue and from a drug-resistant leukemia cell line [3,9]. Mechano-NPS, like other microfluidic methods for single-cell mechanical testing, has demonstrated enhanced deformability in cancer cells, reflecting invasive potential [3,5,7,10,11]. Uniquely, by measuring cell recovery from deformation, mechano-NPS has also been used to uncover age-dependent changes in viscoelastic properties and offers roughly 10 fold faster throughput for viscoelastic testing over more established methods such as optical tweezers [3,12].

Previously, the technical variability of microfluidic techniques like mechano-NPS has only been addressed through simple validation and calibration. For mechano-NPS, Kim *et al*.

made comparisons to published measurements of cortical tension and elastic modulus for several cell lines, showing that their measure of deformability followed trends established with atomic force microscopy and micropipette aspiration, the gold standards for measuring cell mechanical properties [3]. Similarly, a comparison among three recently developed mechanophenotyping microfluidic techniques—hydrodynamic stretching, suspended microchannel resonators, and real-time deformability cytometry—show that all three can, with limited agreement, sense similar trends in deformability [13]. To calibrate hydrodynamic stretching, Gossett *et al*. carried out measurements on droplets of various viscosities, demonstrating the relationship between measured deformability and known values of viscosity [14]. Kang *et al*. calibrated their suspended microchannel resonators using polystyrene beads and hydrogel spheres of varying elastic modulus [15]. For real-time deformability cytometry (RT-DC), Mietke *et al*. and Girardo *et al*. employed theoretical modeling of soft matter deformation in combination with experimental measurements of agar and polyacrylamide beads of varying stiffnesses to validate observed changes in apparent cell deformability as measured by RT-DC [16,17]. Notably, only Gossett *et al*. and Kim *et al*. performed any reliability testing of their respective platforms, and even here, such testing was limited to assessing only a handful of sources of variability [3,14]. It is thus clear that the field is lacking in reproducibility analyses for microfluidic platforms that measure single-cell mechanical properties. Such analysis would provide a critical performance benchmark for the growing number of researchers who may seek to adopt these technologies for their own applications.

Observing this need for reproducibility analyses in our field, we set out to examine the reproducibility of the mechano-NPS system and its measurements of single-cell mechanical phenotypes. To device-to-device variability, we quantified the differences in mechano-NPS results when a single biological sample is tested across multiple replicate devices with relatively low sample sizes. Then, to assess the reproducibility of the mechano-NPS technology platform, we evaluated the similarity in results from two identical experiments conducted on two different sets of mechano-NPS hardware by different researchers in different physical locations.

Overall, we show that average measures of single-cell mechanical parameters using mechano-NPS are highly repeatable. We show that the current mechano-NPS analysis pipeline is capable of high degrees of consistency, high throughput (allowing for large sample sizes), and significantly faster analysis of large data sets compared to prior, manual methods. This work provides an important insight into the performance and reproducibility of mechano-NPS, demonstrating its maturity as a technology and potential for further adoption by other research groups.

3.5.2 Device-to-device variability and its effects on mechanical phenotyping

We first characterized how device-to-device variability could affect mechano-NPS reproducibility, which can be masked when pooling data from several replicate devices and samples. Device-to-device variability can arise from manufacturing, resulting in differences in channel geometry (e.g., channel height and width) that in turn may affect flow rates through a given device. We mechanically phenotyped small samples of AP-1060 cells ($127 \leq n \leq 184$), determining the *wCDI* and recovery time constant using

seven different mechano-NPS devices as described above (**Fig. 3-06**). These AP-1060 cells will also be used later in this dissertation as a model of acute promyelocytic leukemia with a drug-resistant phenotype for which we aimed to uncover mechanical biomarkers.

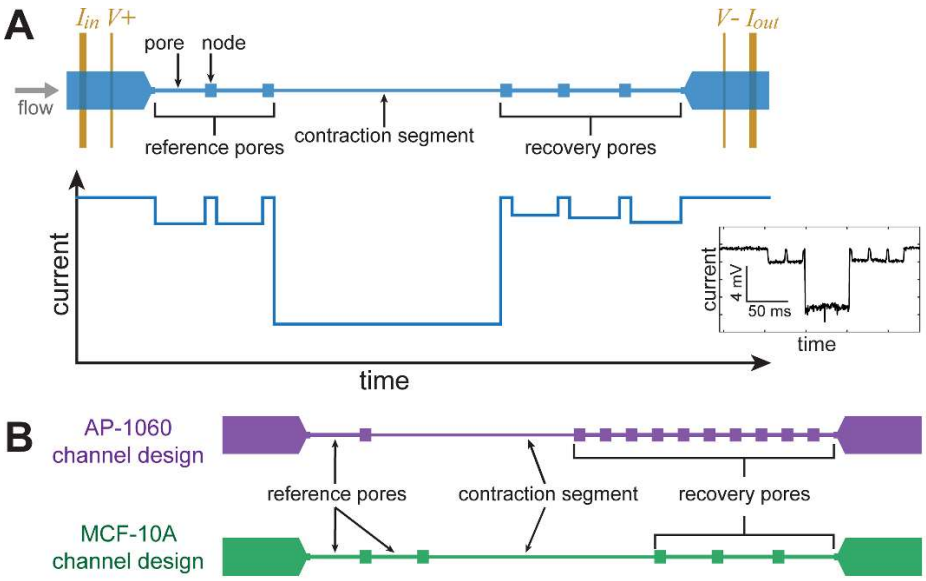

Figure 3-07: A) Top-down schematic view of a mechano-NPS device (top), with corresponding expected electric current pulse (bottom) caused by a single cell transiting the microfluidic channel. A potential is applied across the channel, causing a drop in measured current when a cell enters a narrow segment of the microchannel (pore). Inset: An actual current pulse caused by an MCF-10A cell traversing the channel. (B) Top-down schematic views of mechano-NPS channel designs used in this work for screening AP-1060 and MCF-10A cells.

We found the *wCDI* distributions (**Fig. 3-08A**) from each device to be non-normal (**Appendix 01**). We tested whether the data from these seven devices were sampled from the same distribution with a Kruskal-Wallis test and found that these data reject the null hypothesis of an equal originating distribution ($p < 0.0001$). Pairwise comparisons for all devices showed that only Device 5 was significantly different from Device 3 ($p = 0.0021$), Device 4 ($p = 0.0007$), and Device 7 ($p = 0.0010$) (**Fig. 3-08A**). Pairwise tests of *wCDI* cumulative distribution functions (CDFs) similarly showed that the *wCDI* data from Device 5 was not sampled from the same distribution as Device 3 ($p = 0.0012$), Device 4 ($p = 0.0004$), or Device 7 ($p < 0.0001$) (Bonferroni-corrected for 21 pairwise comparisons, $\alpha = 0.0024$), whereas all other *wCDI* data from each device were sampled from the same distribution (**Appendix 02**).

We performed a similar analysis on recovery time constant data from the same cells (**Fig. 3-08B**). We found that the distributions from several devices were non-normal (**Appendix 01**). Analyzing the recovery data obtained from these seven devices, we found that the recovery time constant data for all seven groups were sampled from the same distribution ($p = 0.21$), precluding the need for further pairwise comparisons. This analysis suggests that compared to *wCDI*, the measurement of continuous recovery time constant is less sensitive to device-to-device variability and is thus more robust against variability in manufacturing.

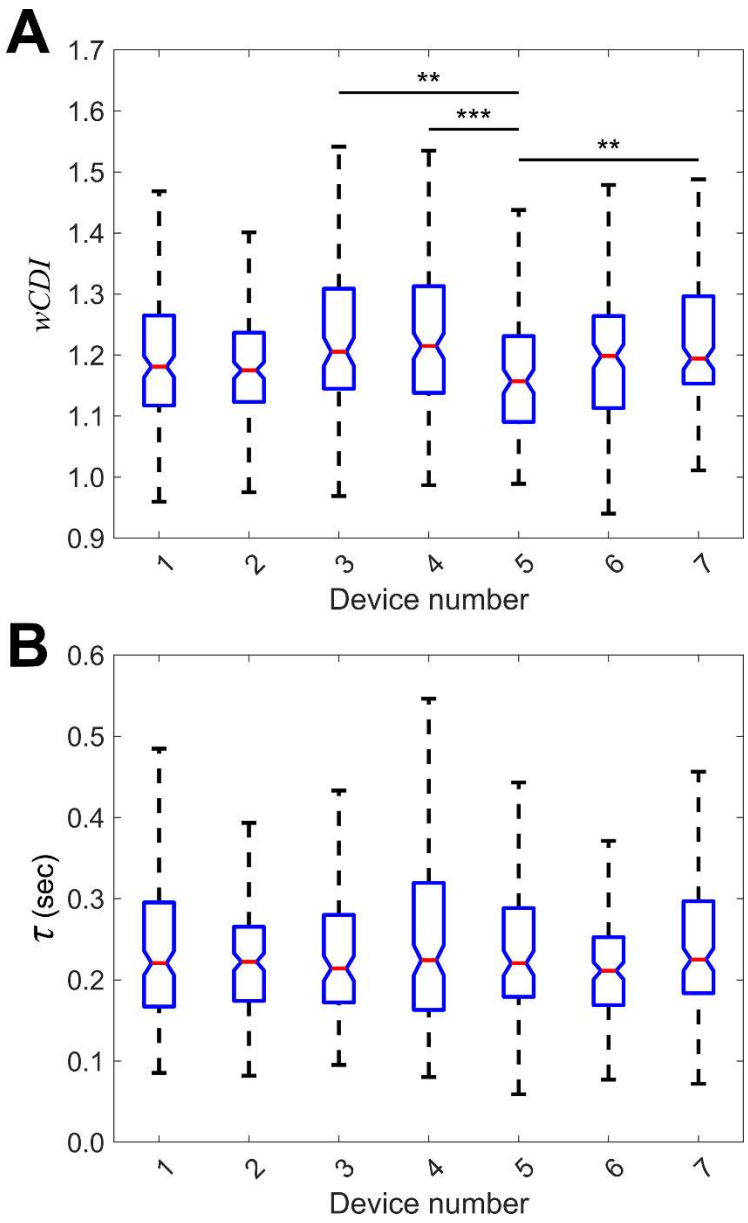

Figure 3-08: (A) Box plots of whole-cell deformability index (*wCDI*) for a single sample of AP-1060 cells analyzed using seven separate devices. Notches represent 95% confidence intervals for the true sample median for each distribution. ** indicates $p < 0.01$; *** indicates $p < 0.001$. Statistical significance between devices was determined using pairwise Wilcoxon rank sum tests for unequal medians, where the critical value for multiple comparisons was calculated using a Tukey-Kramer method. ($p_{3,5} = 0.0021$, $p_{4,5} = 0.0007$, $p_{5,7} = 0.0010$; $n_1 = 182$, $n_2 = 184$, $n_3 = 127$, $n_4 = 176$, $n_5 = 134$, $n_6 = 155$, $n_7 = 167$). (B) Box plots of recovery time constant (τ) for the AP-1060 cells analyzed in (A) on each of seven devices. Notches represent 95% confidence intervals for the true sample median for each distribution. A Kruskal-Wallis test failed to reject the null hypothesis that the recovery time constants measured by each device came from the same distribution. ($n_1 = 182$, $n_2 = 184$, $n_3 = 127$, $n_4 = 176$, $n_5 = 134$, $n_6 = 155$, $n_7 = 167$).

For typical mechano-NPS experiments, the data from replicate devices are pooled before comparisons are made among experimental conditions [3,9]. The discrepancy among *wCDI* data from the different devices highlights the importance of this data pooling, which

reduces the influence of device-to-device variability. This variability may cause the *wCDI* for cells in a certain condition or sample to appear more extreme than they truly are, whereas combining the measurements from several devices increases the statistical power of tests against other conditions by reducing the influence of such extreme values to the test statistic at hand. Even though similar variations were not observed in recovery time constant measurements, data pooling would serve the same purpose. In comparing the difference in median *wCDI* among the seven devices, there was only a 5.04% difference in the two most extreme median values (between Device 5 and Device 6). Devices 3 and 4, which were the next most extreme pair, only varied in median *wCDI* by 2.46%. We consider even 5% variance to be within acceptable tolerances for mechano-NPS devices, as they account for a difference in *wCDI* of approximately 0.06, whereas biologically meaningful differences in *wCDI* using this device design often exceeded 0.1 [9].While biological variability may also influence this result, each of the seven samples of AP-1060 cells were biological replicates and were handled identically prior to mechano-NPS measurements (see Methods). While this served to minimize differences between replicates, biological variability is impossible to completely eliminate. As such, the measured 5.04% difference in median *wCDI* may be an overestimate of the actual device-to-device variability in mechano-NPS. Overall, we demonstrate the degree to which device-to-device variability in mechano-NPS can affect measurements of *wCDI* and recovery time constant.

3.5.3 Comparing mechano-NPS results from experiments performed on different instrumentation platforms

We also investigated whether results from a mechano-NPS experiment are reproducible if another research group utilizes a physically different mechano-NPS platform and conducts the same experiment. Two mechano-NPS platforms were used in this comparison: one located in Berkeley, California and operated by mechano-NPS researchers (Site A), and another located in Duarte, California and operated by a collaborating research group specializing in breast cancer research (Site B) (see Methods for a complete list of hardware). Although there were slight differences in the instrumentation used (e.g., digital vs. analog current preamplifier), the platforms are functionally identical. At both sites, an identical mechano-NPS device design was used to measure MCF-10A cells, and all devices were fabricated at Site A using an identical process (see Methods) [3]. We chose to measure MCF-10A cells in this experiment instead of AP-1060 cells (as above) due to the expertise in breast cancer at Site B (and by extension, the availability of devices designed to measure breast epithelial cells). To compare mechanical phenotyping results, replicate vials of cryo-preserved MCF-10A cells were distributed from Site B, thawed, and cultured in identical growth medium (see Methods). A researcher at each site measured the cells using that site's mechano-NPS platform and extracted two mechanical phenotyping parameters—cell deformability and recovery category—as described in previously published work [3].

Between Site A and Site B results, the MCF-10A mean and median *wCDI* varied by less than 0.4% and 2%, respectively (**Fig. 3-09A**). Lilliefors tests for *wCDI* distributions determined that both Site A ($p < 0.001$) and Site B ($p < 0.001$) distributions were non-normal, and a Mann-Whitney U-test found that the median *wCDI*s were not statistically

significantly different (p = 0.055). We then performed a post hoc power analysis of this test to determine the minimum effect size detectable with 80% power and a significance criterion of α = 0.05. We computed this effect size to be 0.0275; since the actual effect size for this experiment was only 0.0201, we conclude that the difference in median *wCDI* between Site A and Site B is not a meaningful difference. However, we compared the empirical CDFs for *wCDI* data obtained at Site A and Site B (**Fig. 3-09B**) and found that they were statistically significantly different (p = 0.042), with the maximum absolute deviation occurring between the sample medians.

We then investigated the reproducibility of MCF-10A recovery categories. Kim et al. classified cell recovery into three categories: immediate, finite, and prolonged. A cell is classified as "immediate" if it is observed to recover its original shape immediately, "finite" if it recovers within a finite time range, or "prolonged" if it does not recover within the finite range (implying slow, prolonged recovery) [3]. We classified the MCF-10A recovery categories measured by Site A and Site B and, using a Pearson's Chi-squared test, found that the frequencies of recovery categories were significantly different (p < 0.0001) with a Cramér's V of 0.094, which is considered a small-to-medium effect size (**Fig. 3-09C**) [18–20].

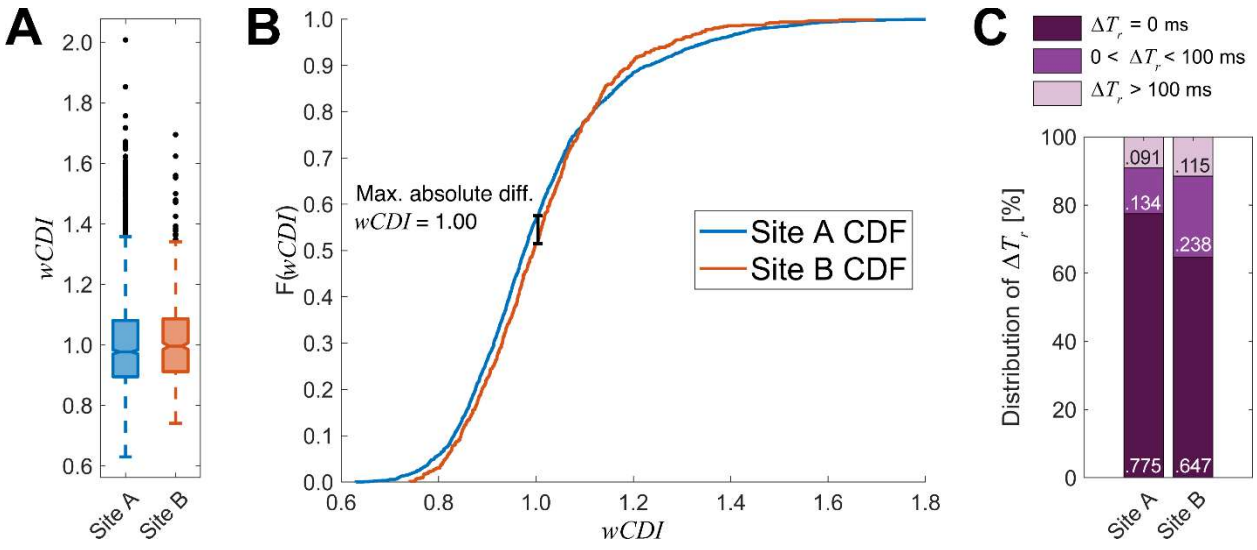

Figure 3-09: (A) Box plots of *wCDI* for MCF-10A cells analyzed at Site A and Site B. Black points represent cells with outlier values of *wCDI*, defined as 1.5 times the inter-quartile range. Notches represent 95% confidence intervals for the true sample median for each distribution. (Site A n = 1960, Site B n = 625). (B) Empirical CDFs for Site A and Site B *wCDI* data. A two-sample Kolmogorov-Smirnov test determined that these data are sampled from different distributions (p = 0.042; Site A n = 1960, Site B n = 625), with the maximum absolute difference occurring at *wCDI* = 1.00. (C) Stacked bar graph representing the relative categorical frequency of MCF-10A cells recovering instantaneously (ΔT_r = 0 ms), within the finite time window (0 < ΔT_r < 100 ms), or failing to recover within the finite time window (ΔT_r > 100 ms). Chi-squared analysis determined that these frequencies were statistically significantly different (p < 0.0001; Site A n = 1960, Site B n = 625; see **Appendix 03**).

By comparing *wCDI* and recovery category data between the two sites, we observed statistically significant differences according to a standard significance criterion of 0.05. As mechano-NPS is easily capable of measuring hundreds to thousands of cells, it is reasonable that even small differences may be statistically significant. In this case, we would expect differences in cell culturing and handling (e.g., expert vs. novice tissue culture technique, lot-to-lot differences in trypsin-based disassociation solutions, etc.) to account for some differences in measured mechanical properties such as those observed here. Furthermore, based on our characterization of device-to-device variability, we cannot exclude the possibility that manufacturing variations also contribute to the differences observed between Site A and Site B.

The effect sizes we observed between sites are small in comparison to biologically meaningful effect sizes observed in past mechano-NPS work. For example, Kim *et al*. tested the effects of immortalizing primary human mammary epithelial cells to mimic malignant progression, which we consider biologically relevant and meaningful [3]. Specifically, we measured a between-sites difference in median *wCDI* of 2%, whereas Kim et al. reported differences ranging from 5.8% to 12.8% for their primary strain 122L when treated with shRNA targeting p16 or cyclin D1 to mimic malignant progression. For recovery category, we reported a Cramér's V of 0.094, and while Kim et al. did not report this figure, we computed a value of 0.242 based on their raw data, which is considered medium-to-large [19,20]. Consequently, while our measurements of MCF-10A cells at Site A and Site B produced statistically significantly different results for *wCDI* and recovery category frequencies, the magnitudes of the effect sizes indicate that these differences may not be meaningful.

Based on this experiment, we conclude that the mechano-NPS results from one research group are highly replicable and reproducible when an identical experiment is performed by another group, even with differences in instrumentation hardware, environmental factors due to climate control, and different individuals performing the experiment. As such, we expect that our results here can be generalized to most other laboratories.

3.5.4 Discussion

Our work assessing experimental reproducibility represents a novel kind of analysis regarding the use of microfluidic technologies for measuring cell mechanical properties. Increasingly complex and powerful devices can introduce greater opportunity for variability, and the repeatability of the measurements made with these technologies should be addressed accordingly. We investigated how technical variation between mechano-NPS devices might affect a measurement, as well as how mechano-NPS measurements might vary when performed by different research groups at different locations. A study such as this one provides a performance benchmark for other researchers who adopt a technology like mechano-NPS and sets expectations of technical variability to assess the reproducibility of experiments. Understanding and minimizing sources of technical variability is especially important because single-cell measurements are inherently sensitive to biological heterogeneity.

3.5.5 Methods

Device design: Design parameters for MCF-10A and AP-1060 devices followed designs from previously published work [3,9]. Geometric features were chosen to optimize the signal-to-noise ratio of the microfluidic four-terminal measurement and apply a specific degree of strain to cells (**Appendix 04**).

Device fabrication: The mechano-NPS channels were fabricated using standard soft lithography. Briefly, a negative-relief master was lithographically fabricated onto a polished silicon substrate using SU-8 epoxy photoresist (MicroChem) (SU-8 3025 for MCF-10A devices, SU-8 3010 for AP-1060 devices). Polydimethyl siloxane (PDMS) (Sylgard 184, Dow Corning) was mixed at a ratio of 9:1 pre-polymer base to curing agent, degassed with a vacuum desiccator, and then poured onto the negative relief masters. The PDMS was cured at 85 °C on a hotplate for 2 h, and a PDMS slab containing the embedded microfluidic channel was subsequently excised. The inlet and outlet ports were cored with a biopsy punch (Harris Uni-Core, Fisher Scientific).

Thin-film metal electrodes and contact pads were fabricated on a glass substrate. Briefly, standard photolithography was used to pattern Shipley 1813 photoresist (MicroChem) on the substrate. Electron-gun evaporation was then used to deposit a 75/250/250 Å titanium/platinum/gold thin film onto the patterned substrate, and photoresist liftoff was accomplished with immersion in acetone (JT Baker 9005-05 CMOS grade). For the MCF-10A devices, a gold wet etch solution (GOLD ETCHANT TFA, Transene Company) was drop-cast onto the area of electrodes crossing the microfluidic channel, exposing the platinum electrodes.

Mechano-NPS device fabrication was completed by treating the PDMS slab and glass substrate with pre-fabricated electrodes with oxygen plasma (Harrick Plasma, 450 mTorr, 30 W, 2 min). 20 µL of 2:1 methanol (ACS Grade, VWR BDH1135-4LG) to water (18.2 MΩ) was drop-cast onto the glass substrate to aid in alignment. The slab and substrate were then aligned, mated, and baked on a hotplate to evaporate the methanol-water mixture. The MCF-10A devices were baked at 85 °C for 2 h, and the AP-1060 devices were baked at 125 °C for 5 min.

Cell culture: AP-1060 cells (DSMZ ACC 593), a gift from Dr. S. Kogan, University of California, San Francisco, CA, U.S.A., were cultured at 37 °C with 5% CO_2. They were initially seeded at a density of 1×10^6 cells/mL in growth medium comprised of 70% Iscove's modified Dulbecco's medium (IMDM, Gibco 12440053), 20% fetal bovine serum (FBS, VWR 89510-186), 10% conditioned medium from cell line 5637 (ATCC HTB-9), and 1X Penicillin-Streptomycin (Gibco 15070063). Cells were passaged when suspension cultures reached a density of 2.5×10^6 cells/mL. Conditioned medium from cell line 5637 was prepared by seeding 2.5×10^5 cells in 10 mL of growth medium consisting of 90% RPMI-1640 (Corning 10-040-CV), 10% FBS, and 1X Penicillin-Streptomycin. Medium was changed after 24 h and collected after another 24 h. Before adding to AP-1060 growth medium, the conditioned medium was filtered using a 0.22 µm polyethersulfone filter (Millipore Sigma SLGPM33RS). For intra- and inter-user repeatability experiments, two samples of AP-1060 cells were treated with LatA (Abcam

ab144290). LatA was reconstituted in ACS reagent grade ethyl alcohol (Sigma-Aldrich 459844) to a stock concentration of 2 mM, then aliquoted and kept frozen at –20 °C until use. LatA was thawed and added to growth medium at a concentration of 2 µM. Cells were subsequently incubated in the LatA-supplemented growth medium for 30 min at 37 °C with 5% CO_2. After 30 min, LatA-treated cells were collected by centrifuging at 200 RCF for 5 min. Cells were washed once with 1X phosphate buffered saline (PBS) and centrifuged again for 5 min at 200 RCF before immediately being resuspended for mechano-NPS measurements (see below).

MCF-10A cells (ATCC CRL-10317) were cultured at 37 °C and 5% CO_2 in M87A medium containing cholera toxin and oxytocin at 0.5 ng/mL and 0.1 nM, respectively. Cells were passaged when adherent culture reached 75% confluence. After the fifth passage, cells were frozen at a concentration of 1 x 10^6 cells/mL for use in reproducibility testing at Sites A and B. Upon thawing at Sites A and B, the cells were seeded at a density of 1 x 10^5 cells/mL and medium was changed every 48 h until they were passaged at 75% confluence, with the last medium change 24 h prior to cell dissociation. Cell dissociation was accomplished by incubating cells in 0.25% trypsin-EDTA (Gibco, 25200056) at 37 °C and 5% CO_2 for 5 min, followed by trypsin neutralization with complete M87A medium (twice the volume of trypsin solution used). MCF-10A cells were collected by centrifuging at 200 RCF for 5 min, washed once with 1X PBS, then centrifuged again for 5 min at 200 RCF before immediately being resuspended for mechano-NPS measurements (see below).

Mechano-NPS measurements: Suspension-culture AP-1060 cells were prepared for mechano-NPS by first transferring the cell suspension into microcentrifuge tubes and centrifuging for 5 min at 200 RCF. After aspirating the growth-medium supernatant, cells were washed with 1X PBS solution and centrifuged again for 5 min at 200 RCF. The PBS was aspirated, and the AP-1060 pellet was resuspended in 1X PBS supplemented with 2% FBS to reduce adhesion between cells and cell adhesion to PDMS. The cell density was diluted to 3 x 10^5 cells/mL in 1X PBS supplemented with 2% FBS.
MCF-10A cells were prepared for mechano-NPS in a similar fashion. Cells were dissociated from the culture dish by incubating with 0.05% trypsin-EDTA (Gibco #25300062) for 10 min at 37 °C, centrifuged for 5 min at 200 RCF, and resuspended in 1X PBS to a cell density of 1 x 10^5 cells/mL.

To perform mechano-NPS measurements, diluted cell suspensions were aspirated into polytetrafluoroethylene tubing (1/32” ID, 1/16” OD, Cole-Parmer EW-06407-41) using a 1 mL slip-tip syringe (BD 309659) fitted with a 20-ga blunt-tip needle (Jensen Global JG20-0.5TX). For MCF-10A experiments, the tubing was inserted into a 1” (length) x 20-ga 304 stainless steel connector (New England Small Tube Corp) which was then inserted into the inlet ports. For AP-1060 experiments, the tubing was directly inserted into PDMS inlet ports. The needle was then disconnected from the syringe and connected to an Elveflow OB1 microfluidic pressure controller. A nominal inlet pressure of 200 mbar (20 kPa) for MCF-10A experiments and 80 mbar (8 kPa) for AP-1060 experiments was applied to induce flow through the mechano-NPS device. A four-terminal current measurement was performed as previously described, using a DC potential of 2.5 V for

MCF-10A experiments and 3 V for AP-1060 experiments, and measuring the current at a sample rate of 50 kHz [2,3,21,22].

The instrumentation used to acquire the mechano-NPS data consisted of a custom-printed circuit board (PCB) to perform the four-terminal measurement, a benchtop power supply, a current preamplifier, and a PCIe DAQ to interface with a computer. The data was recorded using custom MATLAB software as previously published [3]. The same custom PCB was used at Site A and Site B, and the circuit diagram can be found in Kim et al. [3]. Site A used a Keysight E36311A power supply, a DL Instruments 1211 current preamplifier, and a National Instruments PCIe-6351 DAQ. Site B used a Hewlett-Packard/Agilent E3630A power supply, a Stanford Research Systems SR570 current preamplifier, and a National Instruments PCIe-6351 DAQ. The raw data was processed using custom MATLAB code as previously published to calculate the size and mechanical properties of measured cells [3,9,21,22].

Data processing and analysis for mechano-NPS: Current data sampled at 50 kHz was first low-pass filtered using a 200-sample-wide rectangular moving average filter. The filtered signal was downsampled to 2.5 kHz, then detrended using asymmetric least squares smoothing [4]. The element-wise difference of the entire data vector was computed and thresholded according to user-supplied values; for example, for AP-1060 cell measurements, we used a normalized drop-change in current (relative to baseline) cutoff of 2×10^{-4} for pores and 1×10^{-3} for contraction segments. As a cell enters or exits a pore, it causes a step change in the current, which manifests as an extreme value in the first-order discrete time-difference in current. Thus, the threshold separates noise-related fluctuations from these step changes in current. As cells of different sizes generate step changes of varying amplitude, the threshold is set to a value specific to the signal-to-noise ratio of the data. By identifying these step changes, pulse and subpulse boundaries are established, allowing for calculation of subpulse amplitude (i.e., cell size) and duration (i.e., cell velocity). Mechanical parameters are computed as previously described [3,9].

The user-dependent data processing pipeline is described in Fig 1C (code available at https://github.com/sohnlab/mechanoNPS_Li-et-al-2020/releases/tag/mNPS_2020). By finding peak locations in the first-order difference in current, a list of potential data "windows" where a pulse that might belong to a cell are generated. Many windows are automatically classified by the software as signal interference and discarded (e.g., if a subpulse is missing from the window). For the remaining windows, manual confirmation regarding whether the pulse belongs to a cell is necessary through a MATLAB CLI. Threshold values are adjusted as needed by the user before confirming to the program to extract information from the pulse in the window. The user can choose to let the program automatically compute threshold values based on the peak heights in the window or to manually adjust these values.

Statistical methods and analysis: Data for *wCDI* and recovery time constant were tested for normality using a Lilliefors test implemented in MATLAB R2020a. To evaluate differences in non-normal distributions, a Kruskal-Wallis test for non-parametric analysis of variance (ANOVA) across groups was implemented in MATLAB R2020a. For pairwise

comparisons, a Wilcoxon rank sum test with a Tukey-Kramer method to correct the critical value (when applicable) was implemented in MATLAB R2020a. To determine if the probability distributions of *wCDI* and recovery time constant were equal, a two-sample Kolmogorov-Smirnov test with a Bonferroni correction (when applicable) was implemented in MATLAB R2020a. For recovery category data, the proportions of cells in each recovery category were analyzed with a Pearson's Chi-squared test implemented in MATLAB R2020a.

3.6 References

1. DeBlois, R. W. & Bean, C. P. Counting and sizing of submicron particles by the resistive pulse technique. *Rev. Sci. Instrum.* **41**, 909–916 (1970).
2. Saleh, O. A. & Sohn, L. L. Quantitative sensing of nanoscale colloids using a microchip Coulter counter. *Rev. Sci. Instrum.* **72**, 4449–4451 (2001).
3. Kim, J. *et al.* Characterizing cellular mechanical phenotypes with mechano-node-pore sensing. *Microsystems Nanoeng.* **4**, 1–12 (2018).
4. Eilers, P. H. C. & Boelens, H. F. M. Baseline correction with asymmetric least squares smoothing. *Leiden Univ. Med. Cent. Rep.* (2005).
5. Guck, J. *et al.* Optical deformability as an inherent cell marker for testing malignant transformation and metastatic competence. *Biophys. J.* **88**, 3689–3698 (2005).
6. Lammerding, J. *et al.* Lamin A/C deficiency causes defective nuclear mechanics and mechanotransduction. *J. Clin. Invest.* **113**, 370–378 (2004).
7. Tse, H. T. K. *et al.* Quantitative diagnosis of malignant pleural effusions by single-cell mechanophenotyping. *Sci. Transl. Med.* **5**, (2013).
8. Toepfner, N. *et al.* Detection of human disease conditions by single-cell morpho-rheological phenotyping of blood. *Elife* **7**, 1–22 (2018).
9. Li, B., Maslan, A., Streets, A. M. & Sohn, L. L. Mechanical phenotyping of acute promyelocytic leukemia reveals unique biomechanical responses in retinoic acid-resistant populations. *bioRxiv* (2021) doi:https://doi.org/10.1101/2021.04.25.441378.
10. Kim, J., Li, B., Scheideler, O. J., Kim, Y. & Sohn, L. L. Visco-Node-Pore Sensing: A Microfluidic Rheology Platform to Characterize Viscoelastic Properties of Epithelial Cells. *iScience* **13**, 214–228 (2019).
11. Byun, S. *et al.* Characterizing deformability and surface friction of cancer cells. *Proc. Natl. Acad. Sci. U. S. A.* **110**, 7580–7585 (2013).
12. Ekpenyong, A. E. *et al.* Viscoelastic Properties of Differentiating Blood Cells Are Fate- and Function-Dependent. *PLoS One* **7**, (2012).
13. Urbanska, M. *et al.* A comparison of microfluidic methods for high-throughput cell deformability measurements. *Nat. Methods* (2020) doi:10.1038/s41592-020-0818-8.
14. Gossett, D. R. *et al.* Hydrodynamic stretching of single cells for large population mechanical phenotyping. *Proc. Natl. Acad. Sci. U. S. A.* **109**, 7630–7635 (2012).
15. Kang, J. H. *et al.* Noninvasive monitoring of single-cell mechanics by acoustic scattering. *Nat. Methods* **16**, 263–269 (2019).
16. Mietke, A. *et al.* Extracting Cell Stiffness from Real-Time Deformability Cytometry:

Theory and Experiment. *Biophys. J.* **109**, 2023–2036 (2015).
17. Girardo, S. *et al.* Standardized microgel beads as elastic cell mechanical probes. *J. Mater. Chem. B* **6**, 6245–6261 (2018).
18. Cramér, H. *Mathematical Methods of Statistics (PMS-9)*. (Princeton University Press, 1946). doi:10.1515/9781400883868.
19. Cohen, J. *Statistical Power Analysis for the Behavioral Sciences*. (Lawrence Erlbaum Associates, 2013).
20. Kim, H.-Y. Statistical notes for clinical researchers: Chi-squared test and Fisher's exact test. *Restor. Dent. Endod.* **42**, 152 (2017).
21. Balakrishnan, K. R. *et al.* Node-pore sensing: a robust, high-dynamic range method for detecting biological species. *Lab Chip* **13**, 1302 (2013).
22. Balakrishnan, K. R. *et al.* Node-Pore Sensing Enables Label-Free Surface-Marker Profiling of Single Cells. *Anal. Chem.* **87**, 2988–2995 (2015).

Chapter 4: Mechanical phenotyping of acute promyelocytic leukemia reveals unique biomechanical responses in retinoic acid-resistant populations

This chapter is, in part, derived from the following journal article under consideration at *iScience*:

> Brian Li, Annie Maslan, Sean E. Kitayama, Corinne Pierce, Aaron M. Streets, Lydia L. Sohn. Mechanical phenotyping of acute promyelocytic leukemia reveals unique biomechanical responses in retinoic acid-resistant populations. (2021)

4.1 Introduction

Increasingly, physical and mechanical properties such as mass growth rate and deformability, are being explored as possible biomarkers of cancer cells [1–6]. While cells from solid tumors have been the primary focus of these studies, those from liquid tumors have also been investigated, albeit to a lesser extent. Atomic-force microscopy and optical stretcher studies have shown that deformability and mechanical compliance are important in the pathological dissemination of leukemic cells throughout the circulatory system [7–11]. More recently, studies involving suspended microchannel resonators have correlated physical properties (*e.g.*, cell mass and growth rate) of leukemias and lymphomas to important pathological processes such as drug sensitivity or proliferation [12,13], and have determined the biophysical factors that influence cell mechanical properties, such actin remodeling and cell cycle phase [14]. Despite these investigations, the relevance of the physical and mechanical attributes of liquid tumor cells to sensitivity to therapy has yet to be examined [7,13].

Here, we assess the cell mechanics of Acute Promyelocytic Leukemia (APL), an acute myeloid leukemia (AML) subtype characterized by a fusion gene between PML (promyelocytic leukemia protein) and RARA (retinoic acid receptor alpha) [15]. In APL, the PML-RARA fusion gene occurs in granulocytic-precursor cells known as promyelocytes, halting their differentiation and causing rapid proliferation of the immature blasts. Because of the PML-RARA fusion gene, the standard of care for APL patients is to administer all-trans retinoic acid (ATRA), which induces differentiation of the promyelocytes and, in turn, resolves the acute phase of the disease [16–19]. This acute phase can rapidly progress to mortality within a week if left untreated. Early deaths due to disseminated intravascular coagulopathy are of especially great risk in *ATRA-resistant* cases, which comprise nearly 20% of all APL cases [20–23]. Although APL has been well-characterized biochemically using cDNA microarrays and RT-PCR [24–27], there has only been limited characterization of APL cell mechanics. Specifically, Lautenschläger *et al*. showed that the APL cell line, NB4, becomes more deformable with ATRA treatment as it differentiates [9]. However, beyond this work, there have been no investigations of the mechanical responses of ATRA-resistant APL to our knowledge.

We used mechano-node-pore sensing (mechano-NPS) [5], a microfluidic platform that utilizes a narrow channel to deform cells and measure their mechanical properties, to investigate ATRA-sensitive and ATRA-resistant APL cells. Through our mechano-NPS measurements, we determined that ATRA-resistant APL cells are significantly stiffer than ATRA-sensitive APL cells and are influenced by the organization of various structural subcellular components. Using chemical cell-cycle arrest and perturbation of chromatin accessibility, we evaluated how both major and minor changes in nuclear structure, respectively, affect APL mechanical phenotypes. We discovered that only ATRA-resistant APL cells are measurably softened after pharmacological chromatin decondensation. By performing RNA-Seq analysis of ATRA-resistant and ATRA-sensitive cells, we have obtained a whole-transcriptome perspective of how gene expression changes in response to ATRA. This work, in particular, establishes a resource for further studies of ATRA resistance in APL. Overall, our studies show that ATRA-resistance in APL corresponds to a state of cell rigidity that can be measured with mechano-NPS.

4.2 Results

4.2.1 Single-cell mechanical phenotyping of APL cells

Mechano-NPS [5] is an electronic method for mechanophenotyping cells that involves measuring the current across a microfluidic channel segmented by widened "nodes" (**Fig. 4-01A,B**). The width of one segment is narrower than a cell diameter (hereafter referred to as the "contraction" segment), and cells must squeeze through this segment in order to traverse the entire channel (**Fig. 4-01C**). Wider "recovery" segments immediately following the contraction segment allow the cell to recover from deformation. When a cell transits the channel, a unique current pulse is measured. This current pulse is comprised of subpulses that correspond to the cell traversing specific mechano-NPS segments (**Fig. 4-01D**). It is these subpulses from which physical and mechanical properties of the cell can be extracted. Specifically, the magnitude and duration of the subpulse prior to the cell entering the contraction segment reflect the cell size and velocity, respectively. The dramatically large subpulse corresponds to the cell entering the contraction segment, and its duration provides information on the cell's deformability (*i.e.*, a more deformable cell will transit the contraction segment faster than a stiffer cell). Finally, the series of subpulses produced by the cell transiting the series of node-pores following the contraction segment tracks the cell's recovery from deformation. As the cell relaxes back to its original size and shape, the magnitude of the subpulses return to that of the initial subpulse, i.e., the one caused by the cell initially entering the first node-pore segment of the device.

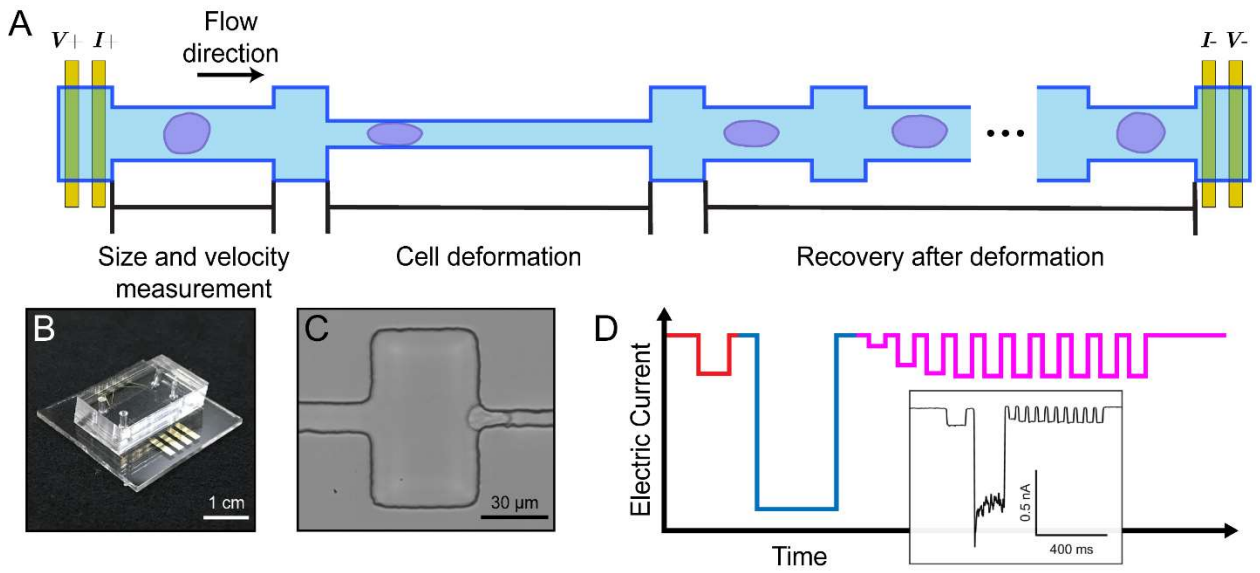

Figure 4-01: Overview of mechano-node-pore sensing (mechano-NPS) platform. A. Top view schematic of mechano-NPS microchannel. A four-terminal measurement is used to measure the current across the microchannel. Cell size (d_0) and velocity (u_{flow}) are measured prior to cell deformation. During deformation, the transit time of a cell is dependent on the cell's elastic modulus. After it leaves the contraction channel, the cell recovers from an ellipsoid shape to a sphere. **B.** Photograph of a mechano-NPS platform, with a polydimethylsiloxane (PDMS) mold embedded with two mechano-NPS channels and bonded to a glass substrate with prefabricated metal electrodes. **C.** High-speed image of an NB4 cell deforming in transit through the contraction channel. **D.** Expected current pulse caused by a cell transiting the entire mechano-NPS channel. The current pulse consists of subpulses that reflect the three main regions of the microchannel. (1) In the initial cell sizing segment (red), the free diameter and transit time of the cell are measured by the subpulse amplitude and duration, respectively. (2) In the contraction segment (blue), the transit time of the cell is measured by the subpulse duration, where more deformable cells transit this segment faster. (3) In the 10 cell recovery segments (magenta), cells recover from a deformed ellipsoid shape to a sphere, which is reflected in the gradual increase in subpulse amplitude over time. The inset shows an actual current pulse produced by an NB4 cell transiting a 6 mm long mechano-NPS channel at an inlet pressure of 80 mbar.

A cell's mechanical response is dependent on the degree of applied strain, ε:

$$\varepsilon = (d_0 - d_c)/d_0 \qquad (1),$$

where d_0 is the cell's initial diameter and d_c is the cell's deformed diameter. For our studies, $e \approx 0.35$ in the contraction segment. To describe a cell's deformability, we use the whole-cell deformability index (*wCDI*), a dimensionless parameter that relates a cell's size and transit time through the contraction segment [5]:

$$wCDI = \frac{l_c}{u_{flow} \times h_{chann}} \times \frac{d_{cell}}{t_{cont}} \qquad (2),$$

where l_c is the length of contraction segment, u_{flow} is the cell's velocity in the pore before the contraction segment, h_{chann} is the height of the contraction segment, d_{cell} is the cell's initial diameter, and t_{cont} is the transit time through the contraction segment. As Kim et al. established with micropipette aspiration studies, the *wCDI* is inversely related to the cell's cortical tension [5], and cells that are softer will have a higher *wCDI* than those that are stiffer. Moreover, the *wCDI* negates cell-size effects: larger cells will naturally take longer to transit the contraction channel compared to smaller cells with similar stiffnesses. To ensure that the friction between channel walls and cell surfaces remained constant in our measurements, we flowed all cells in PBS supplemented with 2% fetal bovine serum.

As cells are intrinsically viscoelastic materials, the time-dependent response to changes in applied stress is a critical aspect of cell mechanical phenotype. To measure cell viscoelastic behavior, we use the recovery segments in our mechano-NPS channel to quantify how cells recover from deformation. For the experiments we report here, we designed a device with 10 recovery channel segments, which provided sufficient information to calculate the time constant of a cell's recovery using linear least squares regression for a Kelvin-Voigt model. This recovery time ranged from 20 ms to 800 ms, with longer recovery times indicative of more viscous behavior.

4.2.2 ATRA-resistant APL cells are phenotypically and mechanically distinct

Of the only three cell lines established from APL patients, we investigated two—NB4 and AP-160—which have varying degrees of sensitivity to ATRA and from which the majority of published APL studies have been performed [9,28–30]. NB4 was derived from a patient who retained the characteristic sensitivity to ATRA differentiation, and AP-1060 was derived from an individual who displayed ATRA resistance [31–33]. We cultured NB4 and AP-1060 cells in media supplemented with ATRA in concentrations ranging from 10 nM to 10 μM and subsequently evaluated their propensity to differentiate (see Materials and Methods). Using flow cytometry to measure expression of CD11b and CD18, two integrins expressed by mature innate immune cells [34], we confirmed that while NB4 cells respond to ATRA, AP-1060 cells were largely resistant (**Fig. 4-02**).

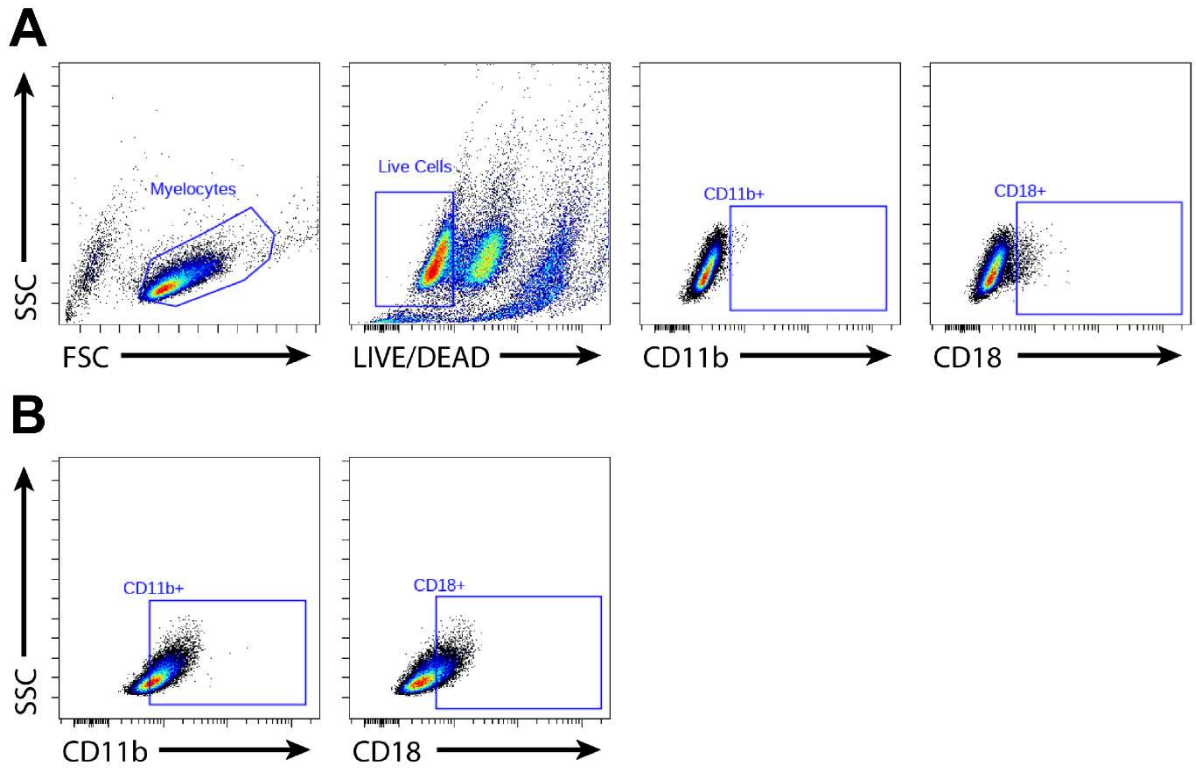
A
Myelocytes
Live Cells
CD11b+
CD18+
SSC
FSC
LIVE/DEAD
CD11b
CD18
B
CD11b+
CD18+
SSC
CD11b
CD18

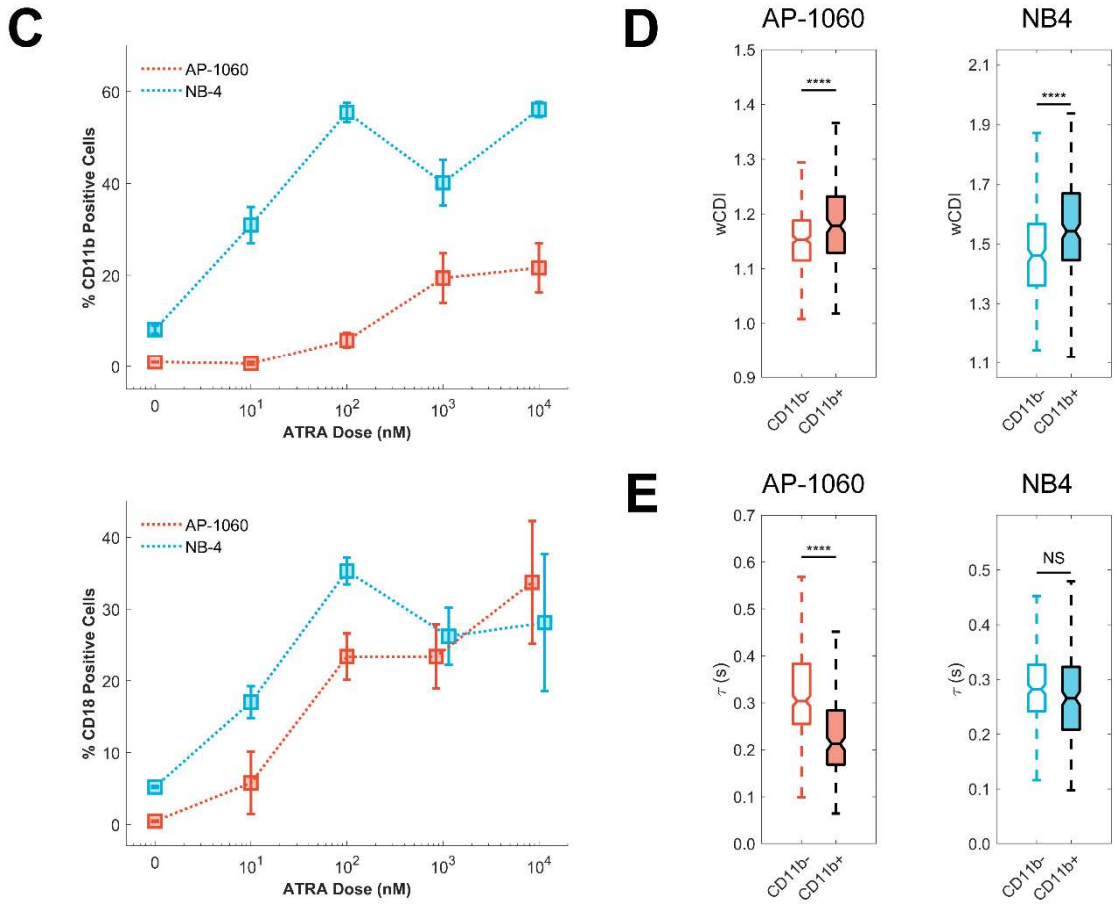
C
AP-1060
NB-4
% CD11b Positive Cells
ATRA Dose (nM)
AP-1060
NB-4
% CD18 Positive Cells
ATRA Dose (nM)
D
AP-1060
NB4
wCDI
****
CD11b-
CD11b+
E
AP-1060
NB4
τ (s)
****
NS
CD11b-
CD11b+

Figure 4-02: Flow cytometric analysis of APL cell line response to ATRA. A, B. Gating strategy for flow cytometry measurements of the CD11b and CD18 expression of AP-1060 and NB4 cells induced to differentiate with ATRA (representative plots from cells treated with 1 μM ATRA for 4 days). **A.** Myelocytes are first identified as a cluster in side scatter (SSC) v. forward scatter (FSC). Live cells are then gated by the LIVE/DEAD-low cluster based on fluorescence from the LIVE/DEAD Violet dye. Fluorescence-minus-one (FMO) controls for each marker were used to determine the true negative fluorescence intensity distribution for the markers' respective fluorophores. **B.** Using gates established by FMO controls, the proportion of ATRA-differentiated cells expressing a certain marker can be measured. **C.** Proportions of cells positive for CD11b and CD18, markers associated with mature/differentiated myelocytes, after treatment with varying doses of ATRA. A stronger differentiation response is seen in NB4 cells, indicating a higher susceptibility to induced differentiation via ATRA. **D, E.** Box plots of *wCDI* (**D**) and recovery times (**E**) for AP-1060 (left) and NB4 (right) cells treated with 1 μM ATRA for 4 days and sorted for CD11b expression. Notches represent 95% confidence intervals for the true median of each distribution. AP-1060 CD11b- $n = 343$; AP-1060 CD11b+ $n = 191$; NB4 CD11b- $n = 234$; NB4 CD11b+ $n = 212$ measured on 3 different devices. ****$p < 0.0001$, determined by two-sample Student's *t*-tests.

The differences between AP-1060 and NB4 cells extend well beyond their biochemical response to ATRA. Upon mechanophenotyping these cells, we found that untreated AP-1060 cells have a significantly lower *wCDI* ($p < 0.0001$) than that of untreated NB4 cells, indicating that they are stiffer (Fig. 2A). After treating both cell lines with two doses of 1 μM ATRA over the course of 4 days (see Materials and Methods), we observed that only NB4 cells showed a significant change in their *wCDI* ($p < 0.0001$) and became more deformable (**Fig. 4-03**). Although the ATRA dose we chose did lead to a limited degree of maturation in AP-1060 cells (**Fig. 4-02C**), there was still no significant change in their overall deformability.

As with their *wCDI*s, we observed differences between the apparent viscosities of the two cell lines via their recovery times. AP-1060 cells were more viscous, taking far longer to recover from deformation than NB4 cells ($p < 0.0001$) (**Fig. 4-03B**). While ATRA-treated AP-1060 recovered significantly faster from deformation than untreated AP-1060 cells ($p < 0.0001$), we surprisingly observed no significant difference in the recovery times of ATRA-treated and untreated NB4 cells ($p = 0.99$). Although AP-1060 cells are overall resistant to ATRA according to their expression of CD11b and CD18, these cells are not completely unresponsive to ATRA when introduced to a high concentration, as has been previously shown (**Fig. 4-02C**)[34]. This partial response, as we have discovered, also corresponds to a partial response in mechanical phenotype where changes in recovery time, but not *wCDI,* occur. Mechano-NPS analysis of ATRA-treated APL cells sorted for CD11b expression showed that both CD11b+ AP-1060 and NB4 cells were far more deformable than CD11b- AP1060 cells ($p < 0.0001$) (**Fig. 4-02D**) and that only for AP-1060 did CD11b+ cells recover significantly faster than their CD11b- counterparts ($p < 0.0001$) (**Fig. 4-02E**). Together, these results show that the differences between AP-1060's and NB4's responses to ATRA affect not only protein expression but also mechanical phenotype, in which ATRA treatment promotes cell softening in cells that are induced to differentiate.

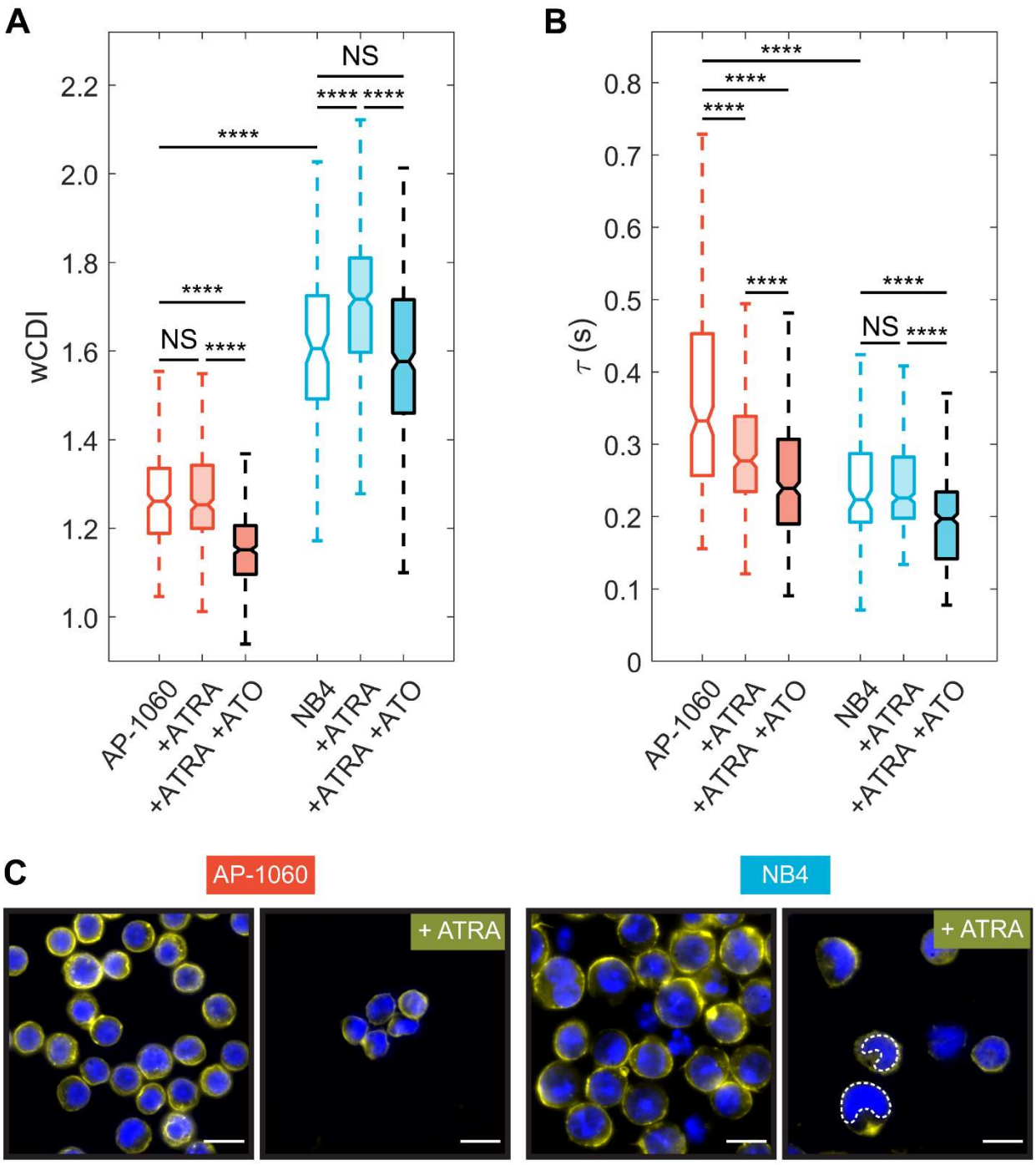

Figure 4-03: APL cell responses to all-trans retinoic acid (ATRA). A, B. Box plots of whole cell deformability index (*wCDI*) (**A**) and recovery times (**B**) for AP-1060 and NB4 cells before and after treatment with all-trans retinoic acid (ATRA). Notches represent 95% confidence intervals for the true median of each distribution. AP-1060 n = 246; AP-1060 + ATRA n = 333; AP-1060 + ATRA + ATO n = 424; NB4 n = 124; NB4 + ATRA n = 402; NB4 + ATRA + ATO n = 419 from 3 biological replicates each measured on a different device. ****p < 0.0001, NS corresponds to no significance; statistical significance was determined by a Tukey test for multiple comparisons. **C.** Fluorescence images of AP-1060 and NB4 cells before and after treatment with ATRA. Cell nuclei stained with Hoescht 33342 (blue); F-actin stained with rhodamine phalloidin (yellow). Lobulated (U-shaped) nuclei in ATRA-treated NB4 cells are highlighted with a white dashed outline. Scale bar = 15 μm.

We additionally evaluated whether arsenic trioxide (ATO), which is commonly administered in conjunction with ATRA to prevent relapse [35], affects APL cell mechanics. Mechano-NPS analysis of AP-1060 and NB4 cells treated with ATRA as before plus 0.25 μM ATO showed that these cells were significantly less deformable and faster to recover compared to those only treated with ATRA ($p < 0.0001$) (**Fig. 4-03B**). ATO is known to alleviate APL primarily by promoting degradation of the PML-RARα fusion protein, whereas ATRA-induced differentiation involves transcriptional regulation mediated by retinoid signaling pathways [36–38]. We hypothesize that it is this difference in pharmacological mechanisms that is reflected in our observations with mechano-NPS; *i.e.* the cell stiffening after ATO treatment relates to the fact that ATO does not induce differentiation like ATRA.

Because the spatial organization and reorganization of the nucleus constitute a critical part of cell mechanics [39–41], we employed fluorescence microscopy to image the nuclei of APL cells before and after ATRA treatment (see Methods). We observed lobulation only in NB4 nuclei (recognizable by the U-shaped nuclei) after ATRA treatment, indicating that differentiation in promyelocytes was progressing (**Fig. 4-03C**)[42]. In contrast, we did not observe such lobulation in ATRA-treated AP-1060 nuclei, which is consistent with the resistance of these cells to differentiate. In general, lobulation is associated with downregulation of lamin A, a protein associated with the nuclear lamina that strongly influences nuclear and whole-cell deformability[43,44]. While immunoblotting for lamin A revealed no detectable expression of this protein in either APL cell line both before or after ATRA treatment (**Fig. 4-04**), this result was expected given prior Western blotting of HL-60 [44], a cell line that was derived from a patient mistakenly diagnosed with APL, but later to be found to lack the PML-RARA fusion gene [46]. Despite the lack of a detectable amount of lamin A in our samples, the striking morphological changes in NB4 nuclei nevertheless suggest that ATRA-associated softening is influenced by structural changes in the nucleus.

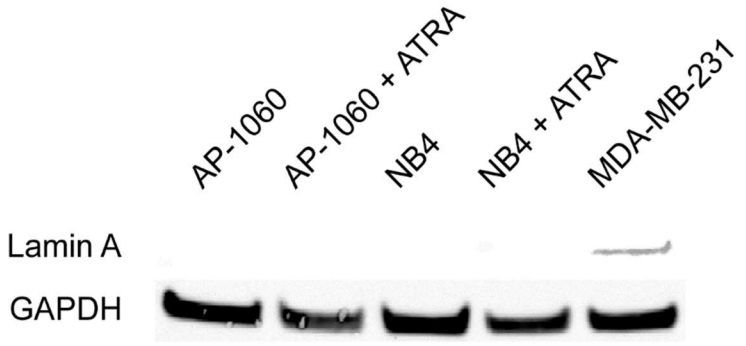

Figure 4-04: Western blot for Lamin A in APL cells. Western blotting of protein isolated from whole-cell lysates of APL cells before and after ATRA treatment. MDA-MB-231 whole-cell lysate was used as a positive control.

In addition to the nucleus, we examined the F-actin network, which provides mechanical support for the cell and its organelles and drives cell motility [45–49]. Although there were no major visual differences in the F-actin network between cell types or before and after ATRA treatment (Fig. 2C), we sought to determine how F-actin might affect cell mechanical properties. We destabilized F-actin with Latrunculin A (LatA) and confirmed the disruption of cortex-localized F-actin in both AP-1060 and NB4 cells (**Fig. 4-05**). Upon mechano-NPS screening of LatA-treated APL cells, we observed no significant differences in the deformability of AP-1060 ($p = 0.61$) or NB4 ($p = 0.19$) cells (**Fig. 4-05B**). However, the recovery times for both cells with disrupted actin cortices were significantly faster than those of untreated cells (AP-1060, $p < 0.0001$; NB4, $p = 0.0027$) (**Fig. 4-05C**), with differences more pronounced with AP-1060 cells than with NB4 cells (125 ms vs. 27 ms faster median recovery, respectively). These results agree with previous work in the literature utilizing latrunculins to measure the mechanical properties of cells in microfluidic contractions [3,5]. Specifically, it was shown that actin destabilization had a greater effect on the viscoelastic processes of cells undergoing deformation (e.g., the time needed for a cell to deform and enter a contraction, or to recover from deformation) than on the transit velocity through narrow contractions [3,5]. Overall, since ATRA affected both the elastic and viscoelastic regimes of APL cells and LatA only affected cell viscoelasticity, we conclude that the mechanical changes in ATRA-treated APL cells are not solely due to any remodeling of the F-actin network that may arise after ATRA treatment.

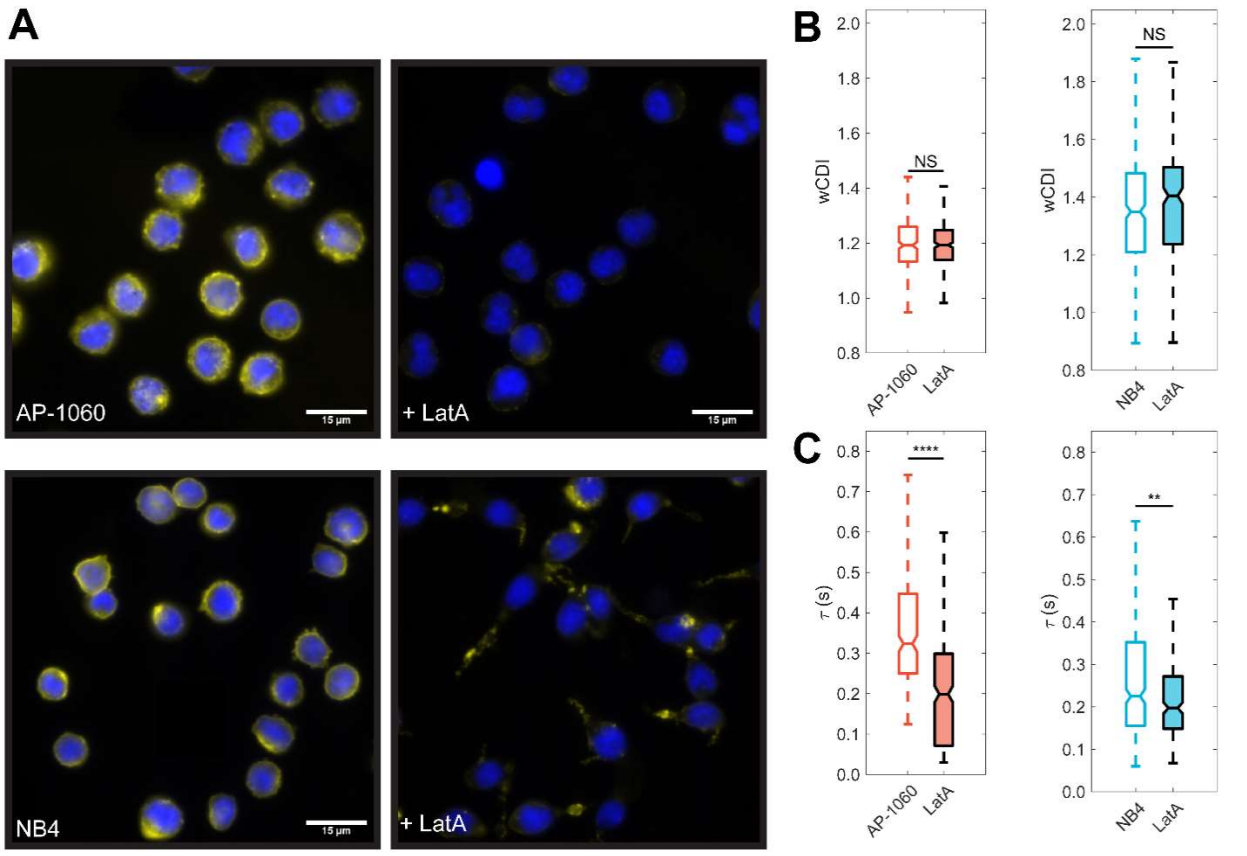

Figure 4-05: Filamentous actin in APL cell cortices primarily influence cell recovery times. A. Fluorescence microscopy of AP-1060 and NB4 cells before and after treatment with Latrunculin A. Blue represents DNA stained with Hoechst 33342 dye, and yellow represents actin stained with rhodamine phalloidin. **B, C.** Box plots of *wCDI* (**B**) and recovery times (**C**) for AP-1060 and NB4 cells before and after treatment with latrunculin A. Notches represent 95% confidence intervals for the true median of each distribution. AP-1060 $n = 268$; AP-1060 + LatA $n = 327$; NB4 $n = 341$; NB4 + LatA $n = 239$ from 3 biological replicates each measured on a different device. $^{**}p < 0.01$ $^{****}p < 0.0001$, NS no significance; determined by two-sample Student's *t*-tests.

4.2.3 APL single-cell mechanical phenotypes vary with DNA content

Because DNA content and nuclear volume change throughout a cell's life cycle, cell-cycle phase is also an important contributor to whole-cell mechanical properties [50–52]. We demonstrated this by performing a series of experiments in which we mechanically phenotyped cells that were synchronized either in M- or S-phase (high DNA content or low DNA content, respectively) Specifically, we used colcemid (a mitotic inhibitor) to arrest cells in M-phase prior to mechanophenotyping (**Fig. 4-06A**). Both NB4 and AP-1060 cells showed a significant increase in stiffness ($p < 0.0001$), with stiffening more pronounced in NB4 cells (**Fig. 4-06B**). Only colcemid-treated NB4 cells had significantly slower recovery times, and thus were more viscous, as compared to their respective untreated cells ($p < 0.0001$) (**Fig. 4-06C**).

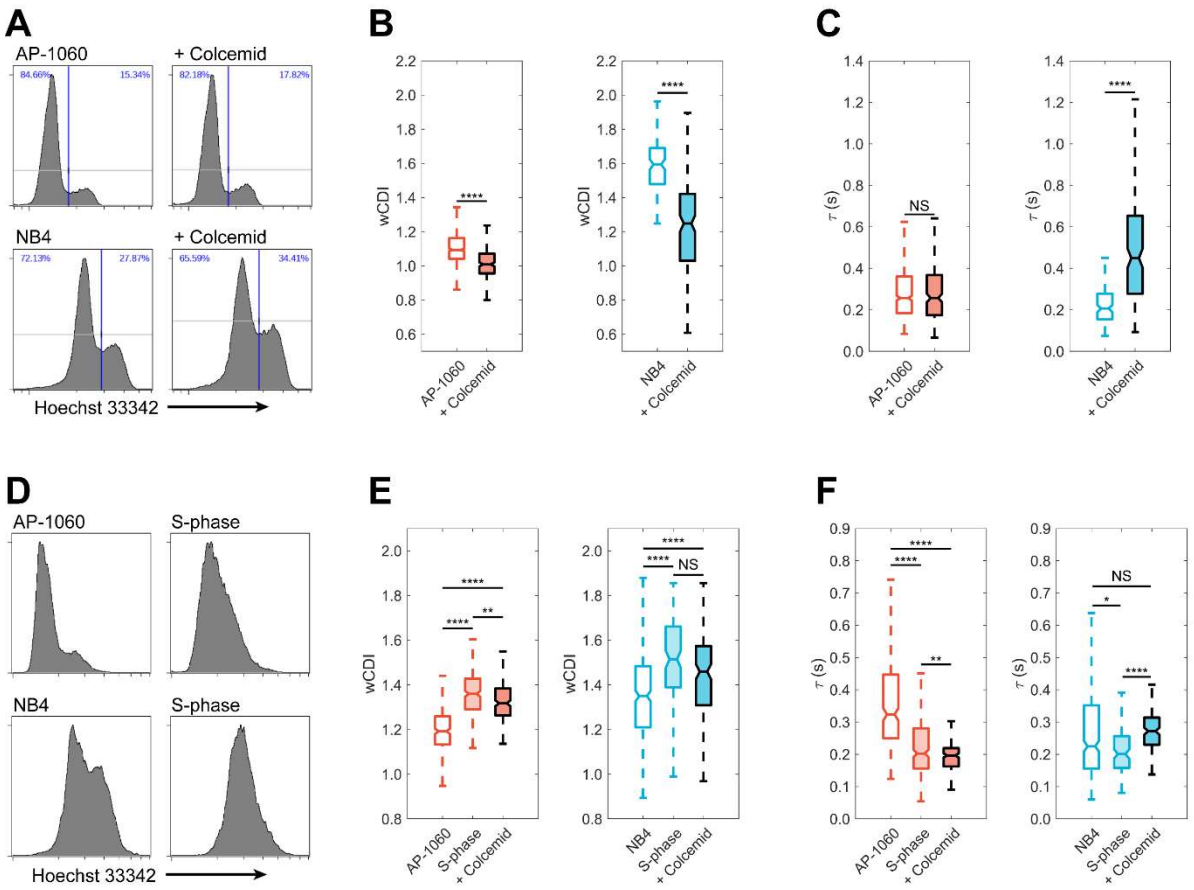

Figure 4-06: Mechanical phenotypes of APL cells are strongly influenced by cell-cycle phase. A. Histograms of DNA content in AP-1060 and NB4 cells before and after colcemid treatment. Colcemid treatment causes small increases in cell counts staining high for DNA, indicating an increased mitotic index. **B, C.** Box plots of whole-cell deformability index (*wCDI*) (**B**) and recovery times (**C**) for AP-1060 and NB4 cells before and after treatment with colcemid. Notches represent 95% confidence intervals for the true median of each distribution. AP-1060 n = 616; AP-1060 + Colcemid n = 236; NB4 n = 123; NB4 + Colcemid n = 167 from 3 biological replicates each measured on a different device. ****$p < 0.0001$, NS no significance; statistical significance was determined by two-sample Student's *t*-tests. **D.** Histograms of DNA content in AP-1060 and NB4 cells before and after synchronization at S-phase with a double thymidine block. Cell cycle synchronization reduces the bimodal distribution to a unimodal distribution, representing a decreased mitotic index. **E, F.** Box plots of *wCDI* distributions (**E**) and recovery times (**F**) for AP-1060 and NB4 cells before and after double thymidine block. Notches represent 95% confidence intervals for the true median of each distribution. AP-1060 n = 268; AP-1060 S-phase n = 282; AP-1060 + Colcemid n = 209; NB4 n = 341; NB4 S-phase n = 122; NB4 + Colcemid n = 151 from 3 biological replicates each measured on a different device. *$p < 0.05$, ****$p < 0.0001$, NS no significance; statistical significance was determined by two-sample Student's *t*-tests.

To determine whether low DNA content would lead to increased deformability and lower viscosity, we mechanophenotyped AP-1060 and NB4 cells that we arrested in S-phase using a double thymidine block (**Fig. 4-06D**) (Bostock, 1971). In contrast to cells arrested in M-phase, cells in S-phase were significantly more deformable than untreated cells ($p < 0.0001$) (**Fig. 4-06E**). Moreover, compared to non-arrested cells, both NB4 and AP-1060 cells recovered from deformation significantly faster after the double thymidine block (NB4, $p = 0.0105$, AP-1060, $p < 0.0001$) (**Fig. 4-06F**).

Thus, increasing or decreasing DNA content can also increase or decrease cell stiffness. To further confirm that DNA content is a strong driver of whole-cell mechanical phenotype, we mechanophenotyped NB4 cells that we sorted based on DNA content (see Materials and Methods) and subsequently and similarly observed that low-DNA content cells had a greater *wCDI* and faster recovery time compared to high-DNA content cells (**Fig. 4-07**).

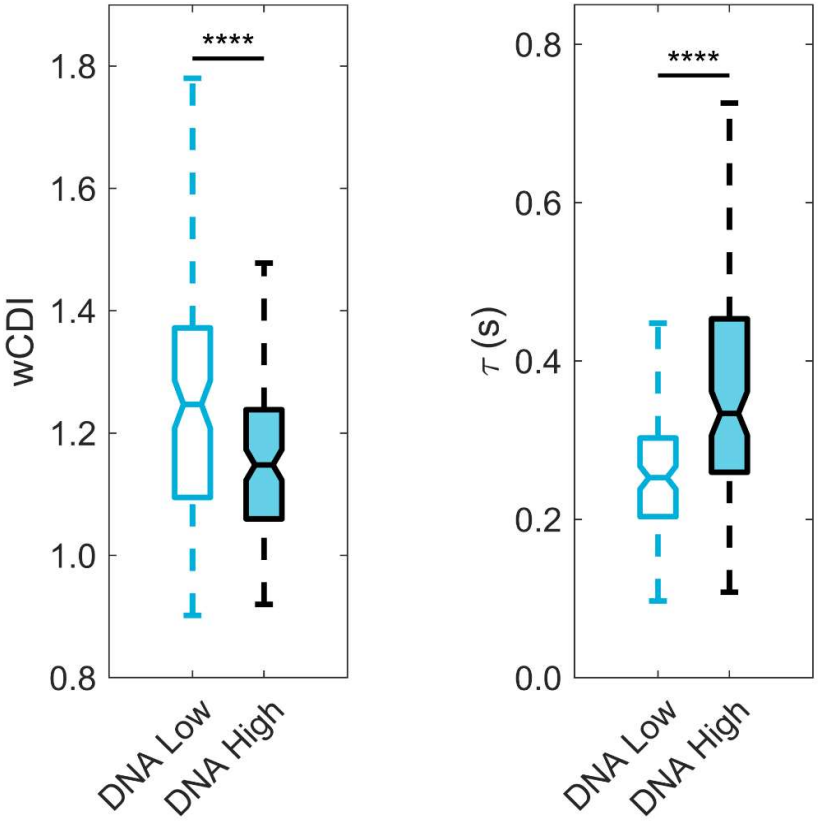

Figure 4-07: NB4 cells sorted for DNA content demonstrate inverse relationship between DNA content and cell pliability. Box plots of *wCDI* (left) and recovery times (right) for NB4 cells stained for DNA (Hoechst 33342) and sorted by DNA content. NB4 populations were sorted into a "DNA Low" tube, indicating non-dividing cells, or a "DNA High" tube, indicating cells undergoing division at the time (M-phase). Cells from each tube were the analyzed with mechano-NPS. Notches represent 95% confidence intervals for the true median of each distribution. DNA low n = 125; DNA high n = 123 measured on 3 different devices. ****$p < 0.0001$, determined by two-sample Student's t-tests.

Because it inhibits cell division by interfering with microtubule dynamics, we focused on determining colcemid's contribution to cell mechanophenotypes independent of modulating DNA content. We first used a double thymidine block to arrest AP-1060 and NB4 cells in S-phase and then treated these cells with colcemid. For AP-1060 cells only, *wCDI* was significantly smaller after this treatment ($p < 0.01$) (**Fig. 4-06E**). However, the recovery time of both AP-1060 and NB4 cells significantly increased ($p < 0.01$ and $p < 0.0001$, respectively) (**Fig. 4-06F**). Thus, colcemid does affect the mechanical phenotype of AP-1060 and NB4 cells, though these effects are far less dramatic than the cell stiffening we observed when cells are arrested in M-phase.

4.2.4 Influences of histone acetylation on APL cell mechanical phenotype

We next probed how the mechanical phenotypes of APL cells depend on the modulation of chromatin accessibility downstream of retinoid signaling (e.g., due to ATRA) [17,54,55]. We perturbed chromatin accessibility independently of ATRA treatment by inhibited histone deacetylase (HDAC) activity with trichostatin A (TSA) (see Materials and Methods), which has been previously shown to soften isolated nuclei [56,57]. To measure primarily the mechanical properties of the nucleus and the effect of TSA, we destabilized actin cortices with LatA and arrested cells in S-phase using a double thymidine block (see Materials and Methods). We then treated the cells with TSA or ATRA and subsequently mechanophenotyped them. As a control, we mechanophenotyped synchronized and LatA-treated cells without further perturbations.

TSA treatment significantly increased *wCDI* in both AP-1060 ($p < 0.0001$) and NB4 ($p = 0.0014$) cells, suggesting that chromatin decondensation indeed causes nuclear softening (**Fig. 4-08A**). In contrast to our earlier experiments when cells were solely treated with ATRA (**Fig. 4-03A**), we unexpectedly observed a dramatic decrease in *wCDI* ($p < 0.0001$) of ATRA-treated actin-destabilized and S-phase arrested AP-1060 cells ATRA (**Fig. 4-08A**). Moreover, actin-destabilized and S-phase arrested NB4 cells were more deformable after ATRA treatment ($p < 0.0001$) (**Fig. 4-08A**), agreeing with the results of our earlier experiments when these cells were only treated with ATRA (**Fig. 4-03A**). Recovery time responses were also different depending on treatment: TSA significantly decreased recovery times in AP-1060 ($p = 0.0095$) but not NB4 ($p = 0.13$) cells (**Fig. 4-08B**); ATRA-treated AP-1060 cells showed no significant difference in recovery time ($p = 0.15$); but NB4 cells took significantly longer to recover ($p = 0.0030$).

Overall, these measurements highlight the complexity of measuring whole-cell deformability, where the effects of certain perturbations (i.e., ATRA) on cell stiffness can change depending on the state of other subcellular components (i.e., F-actin, DNA content). For actin-destabilized and S-phase arrested cells, TSA had a more consistent softening effect than ATRA across both cell types and mechanical parameters, most likely because TSA causes chromatin decondensation. While nuclear softening is expected, TSA treatment may also modulate the expression of genes that could affect single-cell mechanical phenotype [58,59].

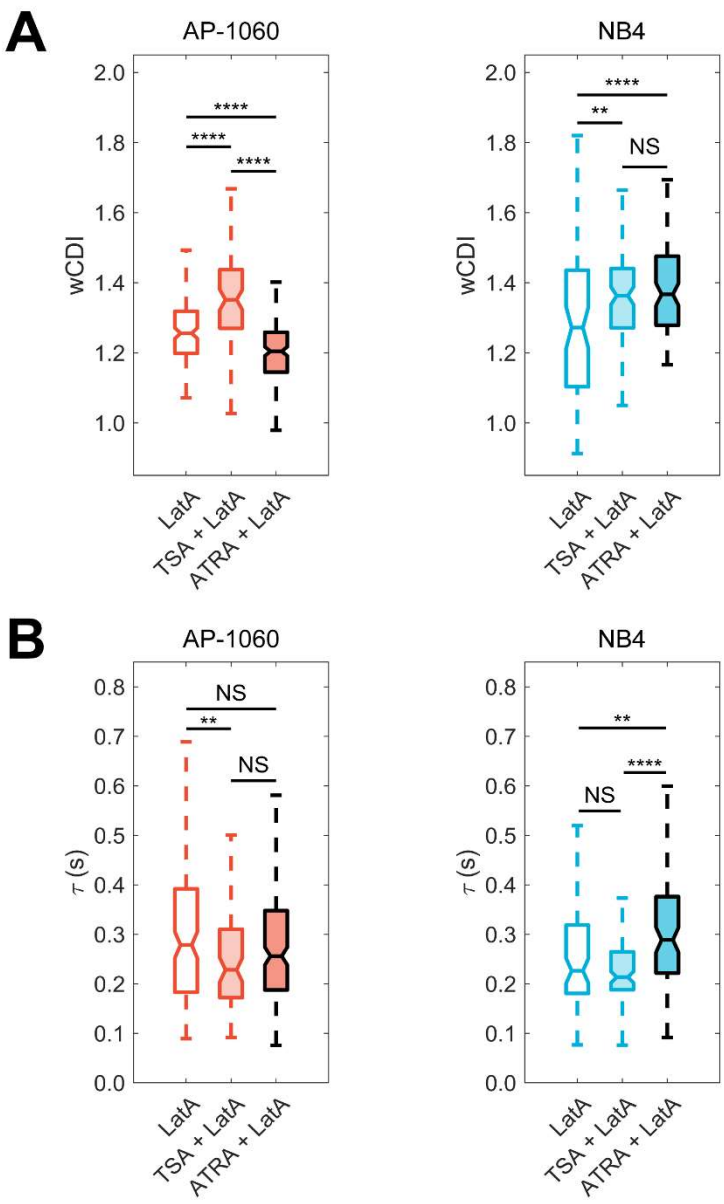

Figure 4-08: Mechanical phenotype of ATRA-resistant APL nuclei is sensitive to histone acetylation. **A, B.** Box plots of *wCDI* (**A**) and recovery times (**B**) for S-phase synchronized AP-1060 (left) and NB4 (right) with actin cortices destabilized with Latrunculin A. Cells were treated with TSA to promote accumulation of decondensed chromatin or ATRA to induce differentiation. AP-1060 + LatA $n = 155$; AP-1060 + TSA + LatA $n = 84$; AP-1060 + ATRA + LatA $n = 199$; NB4 + LatA $n = 75$; NB4 + TSA + LatA $n = 114$; NB4 + ATRA + LatA $n = 95$ from 3 biological replicates each measured on a different device. $^{**}p < 0.01$, $^{****}p < 0.0001$, NS no significance; statistical significance was determined by a Tukey test for multiple comparisons.

4.2.5 Characterizing transcriptomic changes in APL cells with RNA-Seq

Studies involving cDNA microarrays have identified patterns of differential gene expression in APL cells undergoing differentiation after ATRA treatment [26,27]. In contrast, total RNA sequencing captures entire transcriptomes and can thus provide a more thorough exploration of how ATRA differentially affects the gene expression of ATRA-

responsive and ATRA-resistance cells. Here, we performed RNA-Seq on APL cells treated with both ATRA and TSA to identify transcriptional changes potentially associated with mechanical response to treatment. To compare, we performed the same treatments and RNA-Seq analysis on HL-60 cells, a cell line derived from a patient mistakenly diagnosed with APL but whose cells were found to lack the PML-RARA fusion gene [60]. We found that HL-60 cells also lacked the same softening response as APL cells (**Fig. 4-03, Fig. 4-09**). We thus performed RNA-Seq on three cell lines under four different conditions, and identified differentially expressed genes between samples and conditions [61].

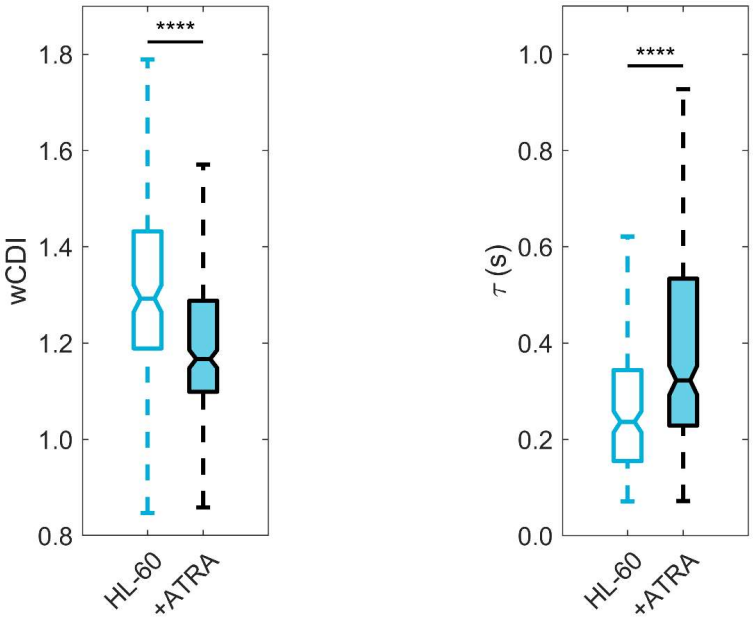

Figure 4-09: HL-60, a non-APL cell line, treated with ATRA. Box plots of *wCDI* (left) and recovery times (right) for HL60 cells before and after ATRA treatment. Notches represent 95% confidence intervals for the true median of each distribution. HL-60 n = 184; HL-60 + ATRA n = 252 from 3 biological replicates each measured on a different device. ****$p < 0.0001$, determined by two-sample Student's t-tests.

In comparing cell lines, NB4 had the most differentially expressed genes (2,523) between untreated and ATRA-treated samples (**Fig. 4-10A**). AP-1060 had fewer differentially expressed genes (1,907), reflecting its ATRA resistance, and HL-60 had the least (1,176), corresponding to its lack of sensitivity to ATRA due to the absence of the PML-RARA fusion gene. Although NB4 cells demonstrated a stronger response to ATRA than AP-1060, there was only one differentially expressed gene (C1QA, part of the classical complement pathway) between TSA-treated and untreated NB4 compared to 86 with AP-1060 in a similar comparison (**Fig. 4-10B**). We also evaluated the interaction of TSA with ATRA by comparing gene expression of ATRA-treated cells to cells treated with both TSA and ATRA. This analysis revealed 13 differentially expressed genes in NB4, compared to 385 in AP-1060 (**Fig. 4-10C**). The greater number of differentially expressed genes in AP-1060 compared to NB4, underscores the former's sensitivity to TSA HDAC inhibition that we previously measured with mechano-NPS.

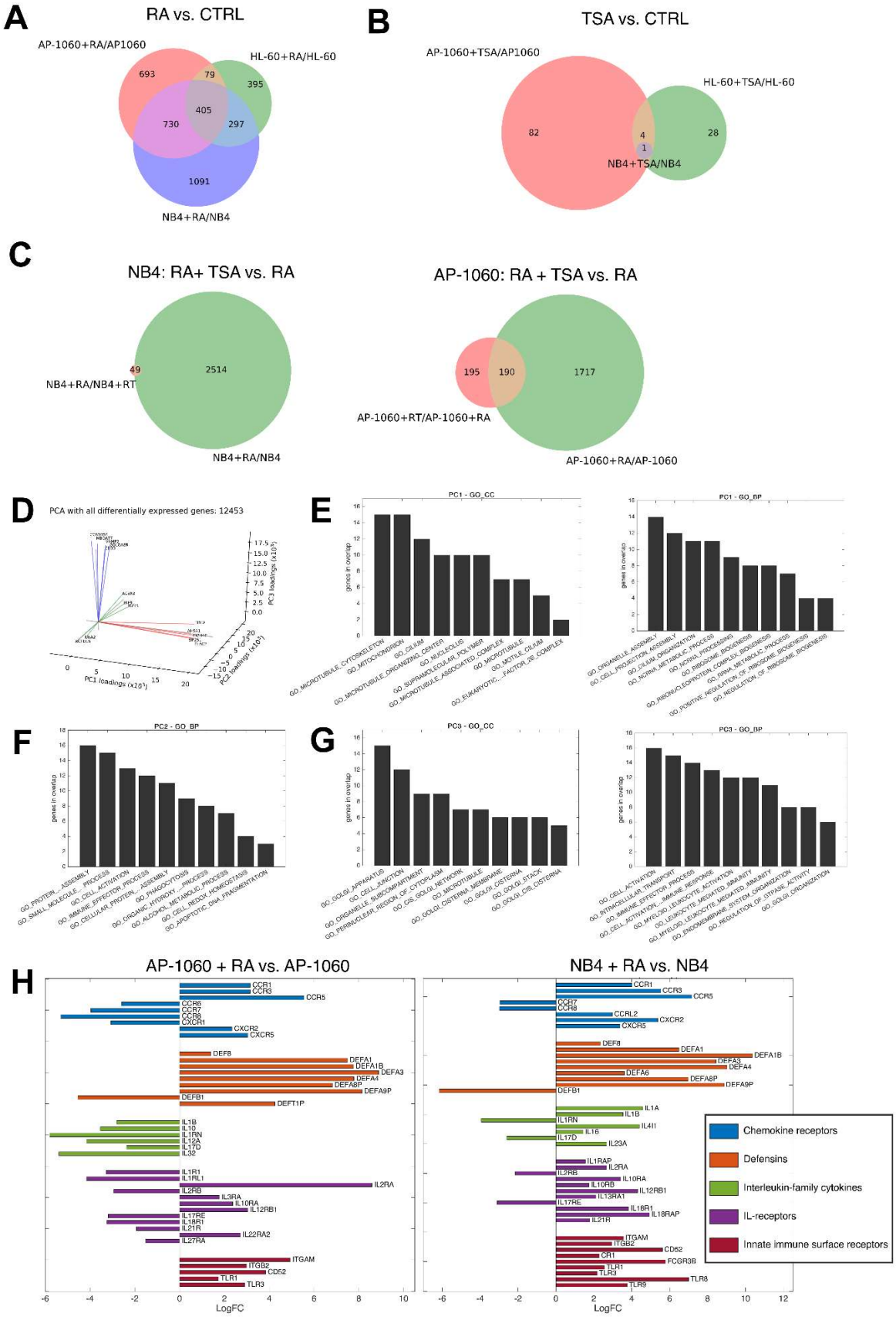
A
RA vs. CTRL
AP-1060+RA/AP1060
HL-60+RA/HL-60
NB4+RA/NB4
693
79
395
405
730
297
1091
B
TSA vs. CTRL
AP-1060+TSA/AP1060
HL-60+TSA/HL-60
NB4+TSA/NB4
82
4
28
1
C
NB4: RA+ TSA vs. RA
NB4+RA/NB4+RT
NB4+RA/NB4
49
2514
AP-1060: RA + TSA vs. RA
AP-1060+RT/AP-1060+RA
AP-1060+RA/AP-1060
195
190
1717
D
PCA with all differentially expressed genes: 12453
E
PC1 - GO_CC
PC1 - GO_BP
F
PC2 - GO_BP
G
PC3 - GO_CC
PC3 - GO_BP
H
AP-1060 + RA vs. AP-1060
NB4 + RA vs. NB4
LogFC
Chemokine receptors
Defensins
Interleukin-family cytokines
IL-receptors
Innate immune surface receptors

Figure 4-10: Differential expression analysis across cell lines and treatment groups. A-C. Venn diagrams for differentially expressed genes identified via RNAseq **A, B.** Untreated AP-1060, NB4, and HL-60 cells were compared to respective ATRA-treated samples (**A**) or TSA-treated samples (**B**). The sets of differentially expressed genes from each cell line-specific pairwise comparison were then compared. **C.** Comparisons to determine what effect TSA has on gene expression, in addition to or in interaction with ATRA. The set of differentially expressed genes for ATRA-treated vs. untreated samples was compared to that of ATRA- and TSA-treated vs. ATRA-treated samples for NB4 (left) and AP-1060 (right). **D.** Biplot for top 5 genes of each principal component according to PC loadings. **E, F, G.** Gene set overlap between the top 100 highest-loading genes of PC1 (**E**), PC2 (**F**), and PC3 (**G**) and MSigDB C5 (gene ontology) gene sets for GO cellular component (GO_CC) and GO biological process (GO_BP). For PC2, only one GO cellular component gene set (GO_NUCLEAR_OUTER_MEMBRANE_ENDOPLASMIC_RETICULUM_MEMBRANE_NETWORK, 13 overlapping genes) overlapped with input genes. **H.** Differentially expressed genes related to immune function and immunophenotyping identified in comparing ATRA-treated vs. untreated AP-1060 (left) and NB4 (right).

We performed principal component analysis on all differentially expressed genes and evaluated the loadings of individual genes to each principal component (**Fig. 4-11A**, **Fig. 4-10D-G**). The first two principal components (PC1 and PC2) clearly separate the different cell types. The third principal component (PC3) separates only AP-1060 samples treated with TSA. Analyzing the top 100 highest-loading genes for each principal component, PC3 was especially enriched for gene ontology terms associated with immune cell function and activation compared to PC1 and PC2. PC1 was primarily enriched for cellular reorganization and RNA processing. PC2 was enriched for several biological processes including metabolism and cell activation.

We analyzed the expression of the 86 differentially expressed genes between untreated AP-1060 and TSA-treated AP-1060. The retinoid signaling-related genes RARRES2 and RBP4 were among the most highly downregulated genes (1st and 11th, respectively) (**Fig. 4-11B**). RARRES2 was found to be upregulated in an HL-60 population made multi-drug resistant via selection with ATRA, and RBP4 has been shown to promote the extracellular transport of retinoic acid [62,63]. As such, downregulation of these two genes could increase sensitivity to ATRA. We filtered these 86 genes by association to the cytoskeleton to identify genes that might also affect cell structure and, by extension, mechanical properties. Several microtubule-associated genes were downregulated, as were cytoskeleton-associated OBSL1, MYBPH, EPSNL, ANKRD22, KRT18, and LMNA (in decreasing order of log-fold change in expression). Only microtubule-associated MAP1A was upregulated. Although the softening in TSA-treated AP-1060 cells is most likely due to direct decondensation of chromatin, the downregulation of these cytoskeletal genes may also contribute to cell softening. Future work is needed to quantify whether any of these genes, by themselves or in concert, have a substantial impact on mechanical phenotype.

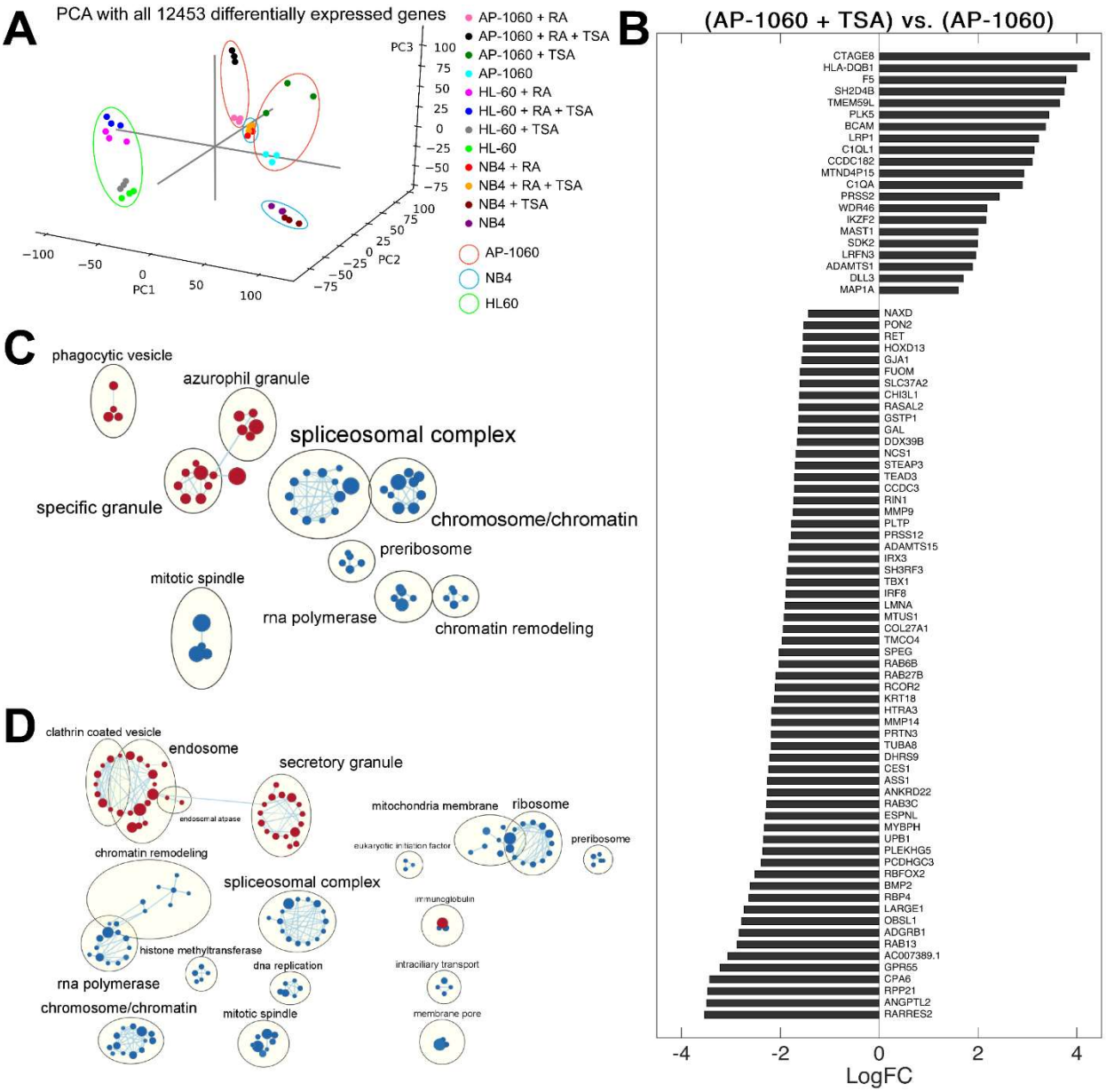

Figure 4-11: RNA-Seq and differential expression analysis of APL cells highlights transcriptional differences in ATRA-resistant AP-1060 cells. A. Principal component analysis of counts per differentially expressed gene identified in any of 66 between-sample pairwise comparisons. **B.** Differentially expressed genes identified in comparing TSA-treated vs. untreated AP-1060. **C.** Enrichment map of positively (red) and negatively (blue) enriched gene sets for ATRA-treated AP-1060 cells. GSEA was performed from the *GO_CC* (Gene ontology cellular component) collection. **D.** Enrichment map of positively (red) and negatively (blue) enriched gene sets for ATRA-treated NB4 cells. GSEA was performed from the *GO_CC* (Gene ontology cellular component) collection.

We next investigated the differentially expressed genes in AP-1060 and NB4 after 96 hours of ATRA treatment. First, we compared our differential expression results to cDNA microarray results from Yang *et al.* in which NB4 cells were also treated with ATRA for 96 hours. While we found agreement in 24 of 62 upregulated genes and 15 of 43 downregulated genes[27], we did not find the remaining genes to be differentially expressed

as Yang *et al.* had. To understand the whole-transcriptome effects of ATRA on our APL cells, especially in the context of controlling cell mechanical phenotype, we carried out gene set enrichment analysis (GSEA) comparing ATRA-treated AP-1060 and NB4 samples to their untreated counterparts. Enrichment maps from this analysis demonstrate a wide range of transcriptional effects from ATRA, and additionally reflect the more dramatic response in NB4 (**Fig. 4-11C, D**). ATRA treatment for both cell lines resulted in positive enrichment of gene sets for granulocytic functions (phagocytosis, granules) associated with differentiation induced by ATRA treatment, with this effect being more pronounced in NB4, as expected. Negatively enriched gene sets in both cell lines were linked to transcription, RNA processing, and chromosome/chromatin organization (Fig. 5C), reflecting the transcriptional and epigenetic regulation that occurs downstream of retinoid signaling [17,54,55]. Furthermore, ATRA-treated NB4 were also negatively enriched for components of DNA replication and epigenetic regulation, including histone methyltransferases (**Fig. 4-11D**). As we showed that DNA content (**Fig. 4-06**) and chromatin decondensation (**Fig. 4-08**) both modulate mechanical phenotype, genes affecting the synthesis and organization of DNA may be important drivers of cell softening in ATRA-treated NB4.

Last, we constructed a gene set to investigate specifically the immunophenotypic landscape of differentiating AP-1060 and NB4 cells. As expected, NB4 cells exhibited greater upregulation of innate immunity-related genes (indicative of differentiation) after ATRA treatment compared to AP-1060 (**Fig. 4-10H**). These data provide a more thorough transcriptomic analysis of ATRA-induced differentiation compared to prior work using cDNA microarrays [26,27], as well as how this response differs in an ATRA-resistant cell line.

4.3 Discussion

APL is a highly aggressive AML subtype that can quickly lead to patient death if therapeutic ATRA regimens are unsuccessful. ATRA induces differentiation of malignant immature promyelocytes, which would otherwise proliferate to the point of patient morbidity. Using mechano-NPS, we have, for the first time, uncovered specific cell mechanical properties that correlate with ATRA-resistant APL. Specifically, we determined that ATRA-resistant AP-1060 cells are stiffer and more viscous than ATRA-sensitive NB4 cells. Through an in-depth study, we determined that the mechanics of APL cells are more dependent on the mechanical properties of their nuclei rather than cytoskeletal components such as microtubule and actin networks. Specifically, major changes in DNA content strongly influenced cell mechanical phenotypes, with high DNA content associated with stiffer and more viscous cells. While it had a more subtle effect on APL cells, chromatin decondensation led to the softening of ATRA-resistant AP-1060 cells, a response seen only in differentiating APL cells. Through RNA-Seq, we discovered enriched gene sets that may also affect mechanical phenotype by way of chromatin remodeling. We also discovered several cytoskeleton-associated genes that were differentially expressed, and so their potential influence on mechanical phenotype should be more fully investigated in future studies. Because ATRA or TSA could directly affect cell structure without affecting transcriptional regulation (*e.g.*, like the destabilization of actin with LatA), it would be valuable to know if changes in transcription, protein structure,

or both are what drive changes in mechanical phenotype.

The importance of nuclear mechanics in APL is further strengthened when considering our results with cells that were synchronized into S-phase and had their F-actin networks disrupted. Synchronized and actin-destabilized AP-1060 cells treated with TSA were more deformable and less viscous than similarly treated NB4 cells. ATRA treatment stiffened these AP-1060 cells, in contrast to cells that were solely treated with ATRA. This may be a consequence of AP-1060's ATRA resistance and the unique epigenomic state of S-phase synchronized cells, where decondensed chromatin is more accessible and susceptible to retinoid signaling [64]. However, further work is warranted to identify the exact mechanism behind this unexpected synergistic effect between cell cycle synchronization and ATRA. Unlike AP-1060 cells, synchronized NB4 cells with disrupted F-actin networks consistently softened after ATRA treatment. Overall, we conclude that while NB4 is robustly sensitive to ATRA, AP-1060 is sensitive to HDAC inhibition with TSA.

Identifying the biophysical factors that link a particular pathological phenotype to a specific mechanical phenotype is a new approach toward the implementation of physical and mechanical biomarkers to characterizing cancer cells. Understanding these factors can explain the biological underpinnings of the mechanical properties of cancer cells, whose potential clinical applications are frequently discussed [65,66]. Within this light, we systematically perturbed subcellular components of APL cells and assessed their relevance to the mechanical phenotype associated with ATRA resistance. In our RNA-Seq analysis, we highlighted genes and gene sets associated with our observations of APL cells and their mechanical properties and provided a resource characterizing the transcriptome of differentiating and ATRA-resistant APL cells. We bridge together two critically under-examined aspects of APL, ultimately uncovering a previously unknown relationship between drug resistance and mechanical phenotype.

4.4 Materials and Methods

Device design and fabrication: All mechano-NPS devices utilized in these studies consisted of a 12.9 ± 0.1 μm high microfluidic channel molded into a polydimethylsiloxane (PDMS) slab that was bonded to a glass substrate with pre-defined platinum (Pt) electrodes and gold (Au) contact pads. PDMS slabs included in-line filters with a pore size of 20 μm to prevent cell clusters that would clog the channel. The central contraction segment, 7 μm x 2000 μm (W x L), was flanked by a single node-segment at its entrance and 10 recovery segments at its exit. While all nodes were 85 μm x 50 μm (W x L), the single segment located in front of the contraction segment was 13 μm x 800 μm (W x L) and the recovery segments were each 13 μm x 290 μm (W x L). Contraction segment length was chosen such that cells experienced deformation for ~150-200 ms. The series of 10 recovery segments provided up to ~500 ms of sampling for recovering cells, which was sufficient to observe the exponential decay of cell strain to a steady-state value.
A standard soft lithography process was used to create the PDMS microfluidic channels. Briefly, negative relief structures were fabricated onto polished silicon wafer using SU8-3010 epoxy resist (MicroChem). SU-8 3010 was spun at 1850 rpm for 30 seconds and baked at 95 °C for 8 minutes. The resist-coated wafer was then exposed to a mask with UV light at a dose of 160 mJ/cm^2, baked again at 65 °C for 1 minute, and then at 95 °C

for 3 minutes. Finally, the wafer was immersed in SU-8 developer (MicroChem) for 2 minutes, then rinsed with water and dried. This process yielded a film thickness and microchannel height of 12.9 ± 0.1 μm (mean ± std. dev.). Sylgard 184 PDMS (Dow Corning) pre-polymer and curing agent were mixed in a ratio of 9:1, degassed, and then poured onto the negative-relief masters. After curing for 2 hours at 85 °C, PDMS slabs with the embedded microfluidic channels were cut and peeled from the relief masters, cored with a 1.5 mm biopsy punch (Harris Uni-Core, Fisher Scientific) to provide input/output access to the microchannel, and then cleaned with isopropanol and deionized water (DI, 18 MW).

Pt/Au electrodes were fabricated using a lift-off process with electron-gun evaporation for metal deposition. The Pt electrodes and Au contact pads were patterned onto glass slides using standard photolithography. First, glass slides were patterned with positive-tone S1813 resist (MicroChem) by spin-coating at 3000 rpm and soft-baking at 100 °C for 1 minute. The wafer was then exposed to a mask with UV light at a dose of 300 mJ/cm^2, and subsequently developed in MF-321 developer (MicroChem) for 45 seconds. A thin metal film consisting of 75 Å Ti, 250 Å Pt, and 250 Å Au was then deposited onto the patterned glass slides using electron-gun evaporation. Excess metal and photoresist were lifted off using acetone. The fabricated metal electrodes were then cleaned with acetone, isopropanol, and DI water. The glass slides with pre-fabricated electrodes and the molded PDMS devices were simultaneously treated with oxygen plasma (2 minutes, 450 mTorr, 30 W, Harrick Plasma) before being bonded together and baked at 125 °C for 5 minutes.

Mechano-node pore sensing: Mechano-node pore sensing was performed as previously described [5]. A DC potential (< 3 V) is applied across the mechano-NPS channel and a four-terminal measurement is performed. Cells transiting the channel partially block the flow of electric current, leading to a modulated current pulse. In the experiments performed, cell suspensions were prepared at a concentration of 300,000 cells/mL in 1X phosphate buffered saline (PBS) solution supplemented with 2% fetal bovine serum (FBS, VWR 89510-186) to reduce cell-cell and cell-PDMS adhesion. Cell suspensions were injected into mechanoNPS devices using a microfluidic pressure controller (Elveflow OB1) with a nominal inlet pressure of 80 mbar. Signals were sampled at 50 kHz, post-processed with a moving-average low pass filter, and then downsampled to 2.5 kHz. A custom command-line interface program, written in MATLAB (available on GitHub) rapidly identifies mechanoNPS pulses, determines subpulse features (i.e. magnitude and duration), and extracts physical and mechanical parameters.

Cell culture: AP-1060 cells, obtained from Dr. S. Kogan, University of California-San Francisco, San Francisco, CA, U.S.A., were cultured in 70% IMDM (Gibco 12440053) supplemented with 20% FBS, 1% Penicillin-Streptomycin (Gibco 15070063), and 10% conditioned medium from cell line 5637 (ATCC HTB-9). For conditioned medium from cell line 5637, cells were seeded in 10 mL of RPMI-1640 (Corning 10-040-CV) supplemented with 10% FBS and 1% Penicillin-Streptomycin (Gibco 15070063). Medium was exchanged after 24 hours, then collected at 48 hours after initial seeding. Conditioned medium was then sterilized using a 0.22 μm polyethylsufone filter (Millipore Sigma

SLGPM33RS). NB4 (DSMZ ACC 207) and HL-60 (ATCC CCL-240) cells were cultured in 90% RPMI-1640 supplemented with 10% FBS and 1% Penicillin-Streptomycin. AP-1060 cells were passaged at a density of 2 x 10^6 cells/mL, seeded in wells of a 24-well plate at a density of 1 x 10^6, and maintained at 37 °C in 5% CO_2. NB4 and HL-60 cells were passaged at a density of 5 x 10^5 cells/mL, seeded in wells of a 24-well plate at a density of 1 x 10^6, and maintained at 37 °C in 5% CO_2.

Pharmacological treatments: Dry powder all-trans retinoic acid (ATRA, Sigma-Aldrich R2625) was reconstituted in anhydrous dimethylsulfoxide to 25 mg/mL for an 83.3 mM concentrated stock solution (Sigma-Aldrich 276855). Concentrated stock solution was aliquoted and snap-frozen in liquid nitrogen, then transferred to a -80 °C freezer for long-term storage. Concentrated stock ATRA was thawed and diluted to 10 mM in dimethyl sulfoxide (DMSO) prior to use, then further diluted to working concentration (10 nM to 10 µM for testing ATRA response; 1 µM otherwise) in cell-culture media. Dry powder arsenic trioxide (ATO, Sigma-Aldrich 202673) was prepared in a 2 mM solution by first dissolving dry ATO in 10% w/w sodium hydroxide (NaOH) in DI water. The NaOH was then neutralized with an equimolar amount of 1 M hydrochloric acid, then diluted with additional DI water. Concentrated stock ATO was diluted to 25 µM in water prior to use, then further diluted to 0.25 µM in cell-culture media. Cells receiving both ATRA and ATO received doses of 1 µM ATRA and 0.25 µM ATO upon seeding and at 48 hours after seeding. LatrunculinA (LatA, Abcam ab144290) was reconstituted in ethyl alcohol (Sigma-Aldrich 459844) and added to cell-culture media at a concentration of 0.5 µg/mL for 30 minutes to disrupt actin filaments. 100 nM of Trichostatin A (TSA, Fisher Scientific 14-061, Mfg. Tocris Bioscience), reconstituted in DMSO, was added to cells for 24 hours to inhibit histone deacetylase activity. For synchronized and LatA-treated cells, cell cultures were first synchronized in S-phase (see below). Cells not receiving further treatment were treated with LatA (see above) immediately prior to mechano-NPS analysis. Cells treated with TSA were incubated in cell culture media supplemented with 100 nM TSA for 24 hours, then treated with LatA (see above) immediately prior to mechano-NPS analysis. Cells treated with ATRA were incubated in cell-culture media supplemented with 1 µM ATRA at 0 and 48 hours after the completion of cell-cycle synchronization, then treated with LatA (see above) 96 hours after synchronization, followed by immediate analysis with mechano-NPS. For all pharmacological treatments, cells were pelleted via centrifugation at 200 rcf for 5 minutes, rinsed once with 1X PBS, then pelleted again, and resuspended for mechano-NPS analysis (see above).

Cell-cycle arrest: A double thymidine block was used to arrest cells at S-phase. Cells were resuspended at 1 x 10^6 cells/mL in cell-culture media supplemented with 2 mM thymidine (Abcam ab143719) and incubated at 37 °C in 5% CO_2 for 18 hours. They were then isolated via centrifugation at 200 rcf for 5 minutes, resuspended at the same density in cell-culture media supplemented with 10 µM deoxycytidine (Abcam ab146218), and subsequently incubated at 37 °C in 5% CO_2 for 8 hours. Finally, cells were again collected via centrifugation at 200 rcf for 5 minutes, resuspended at the same density in cell-culture media supplemented with 2 mM thymidine, and incubated at 37 °C in 5% CO_2 for 18 hours. Synchronized cells were then isolated via centrifugation at 200 rcf for 5 minutes and rinsed once with 1X PBS for further experiments. Colcemid solution in 1X PBS (Gibco

15212012) was used to arrest cell division and synchronize cells in M-phase. Colcemid was added directly to cells in culture media at a concentration of 1 µg/mL. Cell cultures were then incubated at 37 °C in 5% CO_2 for 2 hours. Synchronized cells were then isolated via centrifugation at 200 rcf for 5 minutes and rinsed once with 1X PBS for further experiments. Cell cycle arrest in either S- or M-phase was confirmed via flow cytometric analysis of DNA content (see below).

Fluorescence staining and immunostaining: Silicone isolators (Grace BioLabs CWS-13R-0.5) were pressed onto poly-L-lysine glass slides (VWR 16002-116) to form small wells. Cells in suspension culture were resuspended at 5 x 10^5 cells/mL in 1X PBS, then pipetted into the wells, and allowed to settle and adhere for 1 hour while incubating at 37 °C in 5% CO_2. Wells were then washed with 1X PBS to remove unbound cells. Cells were then fixed with 4% paraformaldehyde (Sigma-Aldrich P6148) and permeabilized with 0.1% Triton X-100 (Sigma-Aldrich T8787). For immunocytochemistry, cells were blocked with donkey serum (Sigma-Aldrich D9663) for 1 hour at room temperature, washed with 1X PBS, then stained overnight with anti-LaminA primary antibody (Invitrogen MA1-06101) at a ratio of 1:200 at 4 °C. Fluorescence staining solutions for immunocytochemistry contained 40 µM Hoechst 33342 (Thermo Scientific 62249), 165 nM rhodamine phalloidin (Biotium 00027), and 1:1000 donkey anti-mouse Alexa-Fluor 488-conjugated secondary antibody (Invitrogen A-21202). Fluorescence staining solutions for ATRA and LatA experiments contained the same concentrations of Hoechst 33342 and rhodamine phalloidin.

Flow cytometric analysis: Cells were isolated by centrifugation at 200 rcf for 5 minutes and resuspended in 1X PBS. For assessing DNA content, cells were stained with 40 µM Hoechst 33342 for 30 minutes, washed with 1X PBS, and analyzed on a BD LSR Fortessa X20 with BD FACSDiva 9.0 software. For immunostained flow cytometry, cells were blocked with an anti-Fc Receptor polyclonal antibody (Invitrogen 14-9161-73) for 30 minutes. An antibody mix for a three-color flow cytometry panel was prepared, consisting of FITC-anti-CD11b (Biolegend 101206), Super Bright 600-anti-CD18 (Invitrogen 63-0189-41), and PerCP-eFluor 710-anti-CD52 (Invitrogen 46-0529-41). Samples were incubated with fluorophore-conjugated antibodies for 35 minutes, then washed several times with 1X PBS. Samples were then stained with LIVE/DEAD Fixable Violet (Invitrogen L34955) and washed several times with 1X PBS prior to analysis. For each experimental condition, one unstained control and three fluorescence-minus-one controls for each antibody-conjugated fluorophore were prepared (Supplementary Fig. S2). Single-stain positive control samples for each fluorophore were prepared prior to all analysis to compute a compensation matrix. Compensation was set such that the median fluorescence intensity in negative channels was the same across single-stain control samples. All analysis of flow cytometry data was performed using Cytobank Community [67]. Sorting of APL cells for both DNA content and CD11b expression was performed with a BD FACSAria Fusion.

Immunobloting: Protein was isolated from whole cell lysates using RIPA buffer (50 mM Tris-HCl, 150 mM NaCl, 1% Triton-X 100, 0.5% sodium dodecyl sulfate) supplemented with 1X Halt Protease Inhibitor Cocktail (Thermo Scientific 78430). The concentration of

protein in lysates was quantified using a bicinchoninic acid assay (Thermo Scientific 23225). Lysates were diluted in LDS Sample Buffer (Invitrogen NP0007), reduced with 5 mM TCEP-HCl (Sigma-Aldrich 646547), and diluted to 0.4 mg/mL with deionized water to ensure equal loading. The samples were then boiled for 10 minutes before being electrophoretically separated on NuPAGE Bis-Tris gels (Thermo Scientific NP0335PK2). Proteins from the gel were then transferred to a nitrocellulose membrane (Thermo Scientific 88013). After transfer, the membrane was blocked for 1 hr with 5% non-fat milk in 1x Tris-buffered saline + 0.1% TWEEN 20 (Sigma-Aldrich P9416) (1x TBS-T), then stained with primary antibodies against Lamin A (Invitrogen MA1-06101) and GAPDH (CellSignaling 2118S) diluted 1:1000 in 5% non-fat milk in 1x TBS-T overnight at 4 ºC. The membrane was then washed three times for 10 minutes with 1x TBS-T, then stained with anti-mouse (LI-COR 926-68070) and anti-rabbit (LI-COR 926-32211) secondary antibodies diluted 1:10,000 in 5% non-fat milk in 1x TBS-T for 1 hr. The membrane was then washed three times with 1x TBS-T before being imaged on a LI-COR Odyssey.

RNA-Seq and differential expression analysis: RNA was extracted from ~1 M cells using the QIAGEN RNeasy Mini Kit (QIAGEN 74104). A total of 36 samples were prepared: for each of three cell lines (AP-1060, HL-60, and NB4), the four conditions of untreated, ATRA, TSA, and ATRA & TSA were run in triplicate. Libraries were prepared using NEBNext Ultra II RNA Library Prep Kit for Illumina (New England Biolabs E7770S) and the NEBNext Poly(A) mRNA Magnetic Isolation Module (New England Biolabs E7490S) with 1 μg total RNA input. Paired-end 2 x 100 bp sequencing was performed on three Illumina HiSeq 4000 lanes with twelve samples per lane for an average sequencing depth of 31M reads per sample. Transcripts were quantified using Salmon (version 0.10.0) [68] in mapping-based mode with the human reference transcriptome (Ensembl GRCh38 version 86) [69]. Read counts were then converted to counts per gene using Bioconductor (version 3.7) [70] with the *tximport* package [71]. Differential expression was determined using *edgeR* (version 3.22.0) and *limma* (version 3.32.0) [72–76]. Significance in differential expression was then filtered by a log-fold change greater than 1 using the TREAT method (*treat* function from *limma*) [61]. Principal component analysis was performed with the *scikit-learn* library in Python [77], and gene set overlaps were computed using the Molecular Signatures Database (MSigDB) and its *Investigate Gene Sets* tools [78,79]. Gene set enrichment analysis was carried out using GSEA 4.0.3, using 497 gene sets from GO Cellular Component (c5.go.cc.v7.2.symbols.gmt) [78,80] after applying a maximum and minimum size threshold of 500 and 15 genes, respectively. For enrichment mapping, enriched gene set nodes were filtered using a false discovery rate cutoff of 25%, and edges were filtered using a similarity cutoff of 50% [81,82].

High-speed imaging: 100 mbar of nominal inlet pressure from an Elveflow OB1 pressure controller drove cells through a mechanoNPS device. Images were acquired using a Fastec IL-5 high-speed camera at 1500 frames per second with a 167 µs shutter speed. Movie playback was set to 50 frames per second.

Mechano-NPS statistical analysis: Statistical tests for mechano-NPS data were applied to measurements of both *wCDI* and recovery time. Significant differences were principally calculated using two-sample Student's t-tests with a significance criterion of α = 0.05. For

experiments involving multiple comparisons, test statistics were instead computed using a Tukey's range test. Where applicable, a Bonferroni correction to the significance criterion (by default, α = 0.05) was made for experiments involving multiple comparisons. To quantify the power of all mechano-NPS statistical tests, we performed a *post hoc* power analysis on all statistical tests made for both *wCDI* and recovery time (**Appendix 05**). The statistical power for each test given the measured effect size and sample size was calculated and reported. For tests not exceeding a power value of 0.80, we reported the minimum effect size needed for a statistical power of 0.80, as well as the measured effect size.

4.5 References

1. Gossett, D. R. *et al.* Hydrodynamic stretching of single cells for large population mechanical phenotyping. *Proc. Natl. Acad. Sci. U. S. A.* **109**, 7630–7635 (2012).
2. Tse, H. T. K. *et al.* Quantitative diagnosis of malignant pleural effusions by single-cell mechanophenotyping. *Sci. Transl. Med.* **5**, (2013).
3. Byun, S. *et al.* Characterizing deformability and surface friction of cancer cells. *Proc. Natl. Acad. Sci. U. S. A.* **110**, 7580–7585 (2013).
4. Toepfner, N. *et al.* Detection of human disease conditions by single-cell morpho-rheological phenotyping of blood. *Elife* **7**, 1–22 (2018).
5. Kim, J. *et al.* Characterizing cellular mechanical phenotypes with mechano-node-pore sensing. *Microsystems Nanoeng.* **4**, 1–12 (2018).
6. Kimmerling, R. J. *et al.* Linking single-cell measurements of mass, growth rate, and gene expression. *Genome Biol.* **19**, 207 (2018).
7. Lam, W. A., Rosenbluth, M. J. & Fletcher, D. A. Chemotherapy exposure increases leukemia cell stiffness. *Blood* **109**, 3505–3508 (2007).
8. Rosenbluth, M. J., Lam, W. A. & Fletcher, D. A. Force microscopy of nonadherent cells: A comparison of leukemia cell deformability. *Biophys. J.* **90**, 2994–3003 (2006).
9. Lautenschläger, F. *et al.* The regulatory role of cell mechanics for migration of differentiating myeloid cells. *Proc. Natl. Acad. Sci. U. S. A.* **106**, 15696–15701 (2009).
10. Stein, E. *et al.* The coagulopathy of acute promyelocytic leukaemia revisited. *Best Pract. Res. Clin. Haematol.* **22**, 153–163 (2009).
11. Pals, S. T., de Gorter, D. J. J. & Spaargaren, M. Lymphoma dissemination: the other face of lymphocyte homing. *Blood* **110**, 3102–3111 (2007).
12. Mu, L. *et al.* Mass measurements during lymphocytic leukemia cell polyploidization decouple cell cycle- and cell size-dependent growth. *Proc. Natl. Acad. Sci.* **117**, 15659–15665 (2020).
13. Stevens, M. M. *et al.* Drug sensitivity of single cancer cells is predicted by changes in mass accumulation rate. *Nat. Biotechnol.* **34**, 1161–1167 (2016).
14. Kang, J. H. *et al.* Noninvasive monitoring of single-cell mechanics by acoustic scattering. *Nat. Methods* **16**, 263–269 (2019).
15. Rowley, J., Golomb, H. & Dougherty, C. 15/17 TRANSLOCATION, A CONSISTENT CHROMOSOMAL CHANGE IN ACUTE PROMYELOCYTIC LEUKAEMIA. *Lancet* **309**, 549–550 (1977).
16. Puccetti, E. & Ruthardt, M. Acute promyelocytic leukemia: PML/RARα and the leukemic stem cell. *Leukemia* **18**, 1169–1175 (2004).
17. Mendez, L., Chen, M. & Pandolfi, P. P. Molecular Genetics of APL. in *Acute Promyelocytic Leukemia* 41–53 (Springer International Publishing, 2018). doi:10.1007/978-3-319-64257-4_4.
18. Tallman, M. S. *et al.* All- trans -Retinoic Acid in Acute Promyelocytic Leukemia. *N. Engl. J. Med.* **337**, 1021–1028 (1997).
19. Douer, D. *et al.* All-trans retinoic acid and late relapses in acute promyelocytic leukemia: Very long-term follow-up of the North American Intergroup Study I0129. *Leuk. Res.* **37**, 795–801 (2013).

20. Park, J. H. *et al.* Early death rate in acute promyelocytic leukemia remains high despite all-trans retinoic acid. *Blood* **118**, 1248–1254 (2011).
21. Ribeiro, R. C. & Rego, E. Management of APL in developing countries: epidemiology, challenges and opportunities for international collaboration. *Hematology Am. Soc. Hematol. Educ. Program* 162–168 (2006) doi:10.1182/asheducation-2006.1.162.
22. Douer, D. *et al.* High frequency of acute promyelocytic leukemia among Latinos with acute myeloid leukemia. *Blood* **87**, 308–313 (1996).
23. Stein, E. *et al.* The coagulopathy of acute promyelocytic leukaemia revisited. *Best Pract. Res. Clin. Haematol.* **22**, 153–163 (2009).
24. Gallagher, R. Retinoic acid resistance in acute promyelocytic leukemia. *Leukemia* **16**, 1940–1958 (2002).
25. Noguera, N. I. *et al.* Acute Promyelocytic Leukemia: Update on the Mechanisms of Leukemogenesis, Resistance and on Innovative Treatment Strategies. *Cancers (Basel).* **11**, (2019).
26. Lee, K. H. *et al.* Differential gene expression in retinoic acid-induced differentiation of acute promyelocytic leukemia cells, NB4 and HL-60 cells. *Biochem. Biophys. Res. Commun.* **296**, 1125–1133 (2002).
27. Yang, L. *et al.* Gene Expression Profiling during All-trans Retinoic Acid-Induced Cell Differentiation of Acute Promyelocytic Leukemia Cells. *J. Mol. Diagnostics* **5**, 212–221 (2003).
28. Zhu, H. *et al.* Role of cofilin-1 in arsenic trioxide-induced apoptosis of NB4-R1 cells. *Mol. Med. Rep.* **22**, 4645–4654 (2020).
29. Abecassis, I. *et al.* Re-expression of DNA methylation-silenced CD44 gene in a resistant NB4 cell line: rescue of CD44-dependent cell death by cAMP. *Leukemia* **22**, 511–520 (2008).
30. Long, J. *et al.* Multiple distinct molecular mechanisms influence sensitivity and resistance to MDM2 inhibitors in adult acute myelogenous leukemia. *Blood* **116**, 71–80 (2010).
31. Roussel, M. J. S. & Lanotte, M. Maturation sensitive and resistant t(15;17) NB4 cell lines as tools for APL physiopathology: Nomenclature of cells and repertory of their known genetic alterations and phenotypes. *Oncogene* **20**, 7287–7291 (2001).
32. Lanotte, M. *et al.* NB4, a maturation inducible cell line with t(15;17) marker isolated from a human acute promyelocytic leukemia (M3). *Blood* **77**, 1080–1086 (1991).
33. Sun, Y. *et al.* Acute promyelocytic leukemia cell line AP-1060 established as a cytokine-dependent culture from a patient clinically resistant to all-trans retinoic acid and arsenic trioxide. *Leukemia* **18**, 1258–1269 (2004).
34. May, R. C. & Machesky, L. M. Phagocytosis and the actin cytoskeleton. *J. Cell Sci.* **114**, 1061–1077 (2001).
35. Adès, L. *et al.* Arsenic trioxide is required in the treatment of newly diagnosed acute promyelocytic leukemia. Analysis of a randomized trial (APL 2006) by the French Belgian Swiss APL group. *Haematologica* **103**, 2033–2039 (2018).
36. Tomita, A., Kiyoi, H. & Naoe, T. Mechanisms of action and resistance to all-trans retinoic acid (ATRA) and arsenic trioxide (As2O3) in acute promyelocytic leukemia. *Int. J. Hematol.* **97**, 717–725 (2013).
37. Geoffroy, M.-C., Jaffray, E. G., Walker, K. J. & Hay, R. T. Arsenic-Induced SUMO-

Dependent Recruitment of RNF4 into PML Nuclear Bodies. *Mol. Biol. Cell* **21**, 4227–4239 (2010).
38. Tatham, M. H. *et al.* Polymeric Chains of SUMO-2 and SUMO-3 Are Conjugated to Protein Substrates by SAE1/SAE2 and Ubc9. *J. Biol. Chem.* **276**, 35368–35374 (2001).
39. Dahl, K. N., Ribeiro, A. J. S. & Lammerding, J. Nuclear Shape, Mechanics, and Mechanotransduction. *Circ. Res.* **102**, 1307–1318 (2008).
40. Friedl, P., Wolf, K. & Lammerding, J. Nuclear mechanics during cell migration. *Curr. Opin. Cell Biol.* **23**, 55–64 (2011).
41. Wolf, K. *et al.* Physical limits of cell migration: Control by ECM space and nuclear deformation and tuning by proteolysis and traction force. *J. Cell Biol.* **201**, 1069–1084 (2013).
42. Lawrence, S. M., Corriden, R. & Nizet, V. The Ontogeny of a Neutrophil: Mechanisms of Granulopoiesis and Homeostasis. *Microbiol. Mol. Biol. Rev.* **82**, (2018).
43. Rowat, A. C. *et al.* Nuclear Envelope Composition Determines the Ability of Neutrophil-type Cells to Passage through Micron-scale Constrictions. *J. Biol. Chem.* **288**, 8610–8618 (2013).
44. Lammerding, J. *et al.* Lamin A/C deficiency causes defective nuclear mechanics and mechanotransduction. *J. Clin. Invest.* **113**, 370–378 (2004).
45. Yamaguchi, H. & Condeelis, J. Regulation of the actin cytoskeleton in cancer cell migration and invasion. *Biochim. Biophys. Acta - Mol. Cell Res.* **1773**, 642–652 (2007).
46. Pollard, T. D. & Cooper, J. A. Actin, a Central Player in Cell Shape and Movement. *Science (80-.).* **326**, 1208–1212 (2009).
47. Chalut, K. J. & Paluch, E. K. The Actin Cortex: A Bridge between Cell Shape and Function. *Dev. Cell* **38**, 571–573 (2016).
48. Gardel, M. L., Schneider, I. C., Aratyn-Schaus, Y. & Waterman, C. M. Mechanical Integration of Actin and Adhesion Dynamics in Cell Migration. *Annu. Rev. Cell Dev. Biol.* **26**, 315–333 (2010).
49. Pegoraro, A. F., Janmey, P. & Weitz, D. A. Mechanical Properties of the Cytoskeleton and Cells. *Cold Spring Harb. Perspect. Biol.* **9**, a022038 (2017).
50. Webster, M., Witkin, K. L. & Cohen-Fix, O. Sizing up the nucleus: nuclear shape, size and nuclear-envelope assembly. *J. Cell Sci.* **122**, 1477–1486 (2009).
51. Aureille, J. *et al.* Nuclear envelope deformation controls cell cycle progression in response to mechanical force. *EMBO Rep.* **20**, (2019).
52. Chu, F.-Y., Haley, S. C. & Zidovska, A. On the origin of shape fluctuations of the cell nucleus. *Proc. Natl. Acad. Sci.* **114**, 10338–10343 (2017).
53. BOSTOCK, C. An evaluation of the double thymidine block for synchronizing mammalian cells at the G1-S border*1. *Exp. Cell Res.* **68**, 163–168 (1971).
54. Bernardi, R. & Pandolfi, P. P. Structure, dynamics and functions of promyelocytic leukaemia nuclear bodies. *Nat. Rev. Mol. Cell Biol.* **8**, 1006–1016 (2007).
55. Nervi, C. *et al.* Caspases mediate retinoic acid-induced degradation of the acute promyelocytic leukemia PML/RARα fusion protein. *Blood* **92**, 2244–2251 (1998).
56. Stephens, A. D., Banigan, E. J., Adam, S. A., Goldman, R. D. & Marko, J. F. Chromatin and lamin a determine two different mechanical response regimes of the

cell nucleus. *Mol. Biol. Cell* **28**, 1984–1996 (2017).
57. Stephens, A. D. *et al.* Chromatin histone modifications and rigidity affect nuclear morphology independent of lamins. *Mol. Biol. Cell* **29**, 220–233 (2018).
58. Minucci, S., Nervi, C., Coco, F. Lo & Pelicci, P. G. Histone deacetylases: a common molecular target for differentiation treatment of acute myeloid leukemias? *Oncogene* **20**, 3110–3115 (2001).
59. Ceccacci, E. & Minucci, S. Inhibition of histone deacetylases in cancer therapy: Lessons from leukaemia. *Br. J. Cancer* **114**, 605–611 (2016).
60. Dalton, W. J. *et al.* HL-60 cell line was derived from a patient with FAB-M2 and not FAB-M3. *Blood* **71**, 242–247 (1988).
61. Mccarthy, D. J. & Smyth, G. K. Testing significance relative to a fold-change threshold is a TREAT. *Bioinformatics* **25**, 765–771 (2009).
62. Liu, S.-M., Chen, W. & Wang, J. Distinguishing between cancer cell differentiation and resistance induced by all-trans retinoic acid using transcriptional profiles and functional pathway analysis. *Sci. Rep.* **4**, 5577 (2015).
63. Blaner, W. S. Vitamin A signaling and homeostasis in obesity, diabetes, and metabolic disorders. *Pharmacol. Ther.* **197**, 153–178 (2019).
64. Alabert, C. & Groth, A. Chromatin replication and epigenome maintenance. *Nat. Rev. Mol. Cell Biol.* **13**, 153–167 (2012).
65. Kozminsky, M. & Sohn, L. L. The promise of single-cell mechanophenotyping for clinical applications. *Biomicrofluidics* **14**, 031301 (2020).
66. Carey, T. R., Cotner, K. L., Li, B. & Sohn, L. L. Developments in label-free microfluidic methods for single-cell analysis and sorting. *Wiley Interdiscip. Rev. Nanomedicine Nanobiotechnology* **11**, e1529 (2019).
67. Kotecha, N., Krutzik, P. O. & Irish, J. M. Web-Based Analysis and Publication of Flow Cytometry Experiments. *Curr. Protoc. Cytom.* **53**, 10.17.1-10.17.24 (2010).
68. Patro, R., Duggal, G., Love, M. I., Irizarry, R. A. & Kingsford, C. Salmon provides fast and bias-aware quantification of transcript expression. *Nat. Methods* **14**, 417–419 (2017).
69. Cunningham, F. *et al.* Ensembl 2019. *Nucleic Acids Res.* **47**, D745–D751 (2019).
70. Huber, W. *et al.* Orchestrating high-throughput genomic analysis with Bioconductor. *Nat. Methods* **12**, 115–121 (2015).
71. Soneson, C., Love, M. I. & Robinson, M. D. Differential analyses for RNA-seq: transcript-level estimates improve gene-level inferences. *F1000Research* **4**, 1521 (2015).
72. Robinson, M. D., McCarthy, D. J. & Smyth, G. K. edgeR: a Bioconductor package for differential expression analysis of digital gene expression data. *Bioinformatics* **26**, 139–40 (2010).
73. McCarthy, D. J., Chen, Y. & Smyth, G. K. Differential expression analysis of multifactor RNA-Seq experiments with respect to biological variation. *Nucleic Acids Res.* **40**, 4288–97 (2012).
74. Phipson, B., Lee, S., Majewski, I. J., Alexander, W. S. & Smyth, G. Robust Hyperparameter Estimation Protects. *Ann. Appl. Stat.* **10**, 946–963 (2016).
75. Ritchie, M. E. *et al.* Limma powers differential expression analyses for RNA-sequencing and microarray studies. *Nucleic Acids Res.* **43**, e47 (2015).
76. Law, C. W., Chen, Y., Shi, W. & Smyth, G. K. voom: precision weights unlock linear

model analysis tools for RNA-seq read counts. *Genome Biol.* **15**, R29 (2014).
77. Pedregosa, F. *et al.* Scikit-learn: Machine Learning in Python. *J. Mach. Learn. Res.* **12**, 2825–2830 (2011).
78. Subramanian, A. *et al.* Gene set enrichment analysis: A knowledge-based approach for interpreting genome-wide expression profiles. *Proc. Natl. Acad. Sci.* **102**, 15545–15550 (2005).
79. Liberzon, A. *et al.* Molecular signatures database (MSigDB) 3.0. *Bioinformatics* **27**, 1739–1740 (2011).
80. Mootha, V. K. *et al.* PGC-1α-responsive genes involved in oxidative phosphorylation are coordinately downregulated in human diabetes. *Nat. Genet.* **34**, 267–273 (2003).
81. Merico, D., Isserlin, R., Stueker, O., Emili, A. & Bader, G. D. Enrichment Map: A Network-Based Method for Gene-Set Enrichment Visualization and Interpretation. *PLoS One* **5**, e13984 (2010).
82. Shannon, P. Cytoscape: A Software Environment for Integrated Models of Biomolecular Interaction Networks. *Genome Res.* **13**, 2498–2504 (2003).

Chapter 5: Multiplexed DNA-directed patterning of antibodies for single-cell surface marker analysis

This chapter is, in part, a postprint of the following journal article:

> Molly Kozminsky, Olivia J. Scheideler, Brian Li, Nathaniel K. Liu, Lydia L. Sohn. Multiplexed DNA-Directed Patterning of Antibodies for Applications in Cell Subpopulation Analysis. *ACS Applied Materials and Interfaces* **13** (2021).

5.1 Introduction

The expression of surface proteins is a critical component of a cell's phenotype and is commonly measured using antibody labels. For example, liquid biopsy devices have used immobilized antibodies to analyze and capture circulating tumor cells (CTCs) [1]. However, CTCs may have a number of different phenotypes, especially due to epithelial-to-mesenchymal transitions (EMT) [2]. As a result, there is increasing demand to analyze cells for several surface markers to identify phenotypic subpopulations in a sample of cells. For this application, it is necessary to immobilize multiple antibodies in a way that makes it possible to analyze a single cell for several antigens. We address this need by employing DNA-directed patterning to immobilize antibodies along the base of PDMS-on-glass microfluidic devices utilizing node-pore sensing, which was previously used to assay cells for surface proteins [3,4]. Here, we demonstrate that DNA-directed patterning of antibodies is a highly flexible method for functionalizing surfaces for label-free surface marker screening. The previous method for functionalizing NPS channel segments with different antibodies involved an aminosilane-based conjugation chemistry scheme that required two overnight steps in cold and humidity-controlled storage[4]. In addition, an orthogonal temporary channel to flow antibodies across prepared areas was needed. Finally, permanent bonding of the NPS channel to the prepared glass substrate was not possible, as antibody damage occurred due to exposure to oxygen plasma and high heat[4]. Manual clamping between the PDMS-based NPS channel and the substrate was therefore necessary, leading to uneven pressure applied to the channel that then altered cell velocities and also resulted in leakage.

Our results show that a next-generation node-pore sensing device, in which anti-EpCAM is patterned, can differentiate between MCF-7 and Jurkat cells based on EpCAM expression. We also highlight the advantage of our multiplexing capabilities by immunophenotyping MCF10A, MCF-7, and Hs 578T cells for E-cadherin, N-cadherin, and β-integrin, markers corresponding to epithelial-mesenchymal transitions, using a next-generation NPS device that integrates the three antibodies against these surface markers. Together, the results from these proof-of-concept applications highlight that our antibody immobilization strategy utilizing DNA-directed patterning allows for high-throughput screening of surface markers with a flexible and multiplexable conjugation chemistry.

5.2 Results

Reaction scheme for linkage of antibodies to glass via DNA-directed patterning
DNA-directed patterning has been described in detail in other work by our lab [3] (**Fig. 5-01**). To summarize, aldehyde-functionalized glass serves as the solid-phase substrate to which single-stranded oligonucleotides are conjugated. To define features and patterns of DNA, positive-tone S1813 photoresist is patterned using photolithography to mask regions of the aldehyde-functionalized glass where DNA should not be conjugated. With these photolithographic masks in place, 5'-aminated ssDNA is drop casted onto the glass and covalently bonded in the exposed regions. The resist is then stripped with acetone, leaving the immobilized ssDNA and allowing for further rounds of photolithographic patterning and DNA drop casting. Finally, to attach a biomolecule such as a protein, the protein is first conjugated to another ssDNA molecule complementary to the immobilized strand. By simply adding the protein-ssDNA conjugate to an aqueous solution atop the DNA-patterned glass, the protein will also be specifically patterned according to base-pairing chemistry.

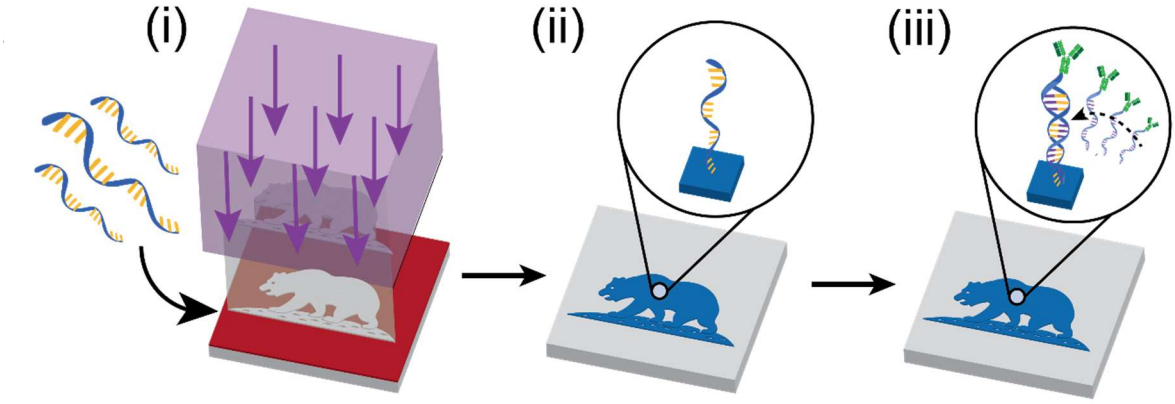

Figure 5-01: Schematic of patterning protocol: **(i)** A photoresist template on a glass slide is created using photolithography, and amine-terminated DNA oligonucleotides are drop cast where they conjugate onto exposed glass; **(ii)** oligonucleotide conjugated to the surface with all photoresist stripped; **(iii)** hybridization of the complementary sequence, conjugated to an antibody, to the oligonucleotide patterned on the slide surface enables directed patterning of antibody on the surface.

The conjugation of the protein of interest – in this case, an antibody molecule – has some special considerations. To summarize, our strategy involves the use of amine-reactive NHS ester linkage of a heterobifunctional crosslinker to the protein. This crosslinker contains, on one end, the amine-reactive NHS ester moiety, and on the other end, a dibenzocyclooctyne (DBCO) moiety for performing copper-free click chemistry, with a 5-unit polyethylene glycol (PEG5) as a spacer [5]. This DBCO moiety will freely react with any azide group, and as such, the DNA intended to be conjugated to the protein is terminated with an azide at its 5' end.

To start, NHS ester chemistry is reactive with primary amines, which, on polypeptides, are present on the N-terminus and on any lysine residues. The efficiency of this reaction depends on the protonation of these amines, and so alkaline conditions are preferred to ensure these amines are indeed protonated. It is worth nothing that free hydroxyl ions will also hydrolyze the NHS ester, but despite this, a pH between 8.0 – 9.0 is a good range to perform this reaction in, despite accelerating hydrolysis[6]. This is important because the

antibodies we purchased from vendors, if they were shipped in solution, were packaged in phosphate-buffered saline at pH 7.4. As such, it is necessary to elevate the pH before adding the heterobifunctional crosslinker.

While one could simply elevate the pH with the addition of strong base, the salt concentration in phosphate-buffered saline is another concern. The DBCO on the heterobifunctional crosslinker is more hydrophobic than the primary amine it replaces; at high salt concentrations (i.e., in phosphate-buffered saline), we found that after addition of DBCO to the protein, it could precipitate out of solution (**Fig. 5-02**).

Figure 5-02: Photograph of immunoglobulin protein precipitating in high salt after DBCO addition.

To remedy both this and the pH, we performed a buffer exchange via ultrafiltration prior to addition of the heterobifunctional crosslinker. While a variety of buffer solutions are adequate for this, we chose to use an aqueous solution 0.2 M sodium bicarbonate, as this is easy to prepare and the weak base by itself increases the solution pH to approximately 8.4. While this buffer exchange does not purify the protein solution of all salt, it removes 90% of the salt such that even high degrees of DBCO labeling do not cause the protein to crash out of solution.

Another consideration from packaging/storage of antibodies is the presence of sodium azide. In many cases, antibody solutions are shipped with sodium azide in solution as a preservative. However, as mentioned before, *any* azide will freely react with the DBCO conjugated to the protein. As such, it is necessary to purify the reaction solution of sodium azide before the addition of the heterobifunctional crosslinker to preserve the reactivity of conjugated DBCO. For low concentrations (unconjugated monoclonal antibodies from Invitrogen, 0.09% sodium azide), the aforementioned buffer exchange was adequate to purify the reaction volume of azide. However, at higher concentrations (fluorescently labeled monoclonal antibodies from Invitrogen, 5 mM sodium azide), our buffer exchange process would have left the azide concentration at unacceptable levels. To remedy this, we first quenched the amine-reactive end of heterobifunctional crosslinker with Tris-HCl to prevent conjugation to the protein. We then added a 4-fold molar excess of this quenched crosslinker to the protein solution containing 5 mM sodium azide and allowed this reaction to progress for 24 hours. This step effectively prevented the free sodium azide from reacting with new, heterobifunctional crosslinker with an intact NHS ester. As

such, this scheme ensured that the protein is primarily conjugated with reactive DBCO, instead of DBCO that already reacted with free sodium azide.

After a few hours, any heterobifunctional crosslinker still in solution will have its NHS ester moiety hydrolyzed. However, as the DBCO may still be intact, these functional groups may still react with the 5'-azide DNA to be added in the next step, preventing the conjugation of the DNA to the protein. Therefore, it is critically important to purify the reaction volume of DBCO starting material; fortunately, this is easily accomplished with size-exclusion chromatography, as the crosslinker molecular weight is less than 1 kDa, whereas an immunoglobulin molecular weight easily exceeds 100 kDa. After retaining this starting material in the chromatography matrix and retrieving the DBCO-labeled protein, the ssDNA is added in a 2-fold molar excess to ensure efficient labeling of the protein. Similar to the DBCO starting material, any ssDNA that is not purified from the reaction volume prior to hybridization will contaminate the surface with starting material. In this case, this means that ssDNA on the glass surface can hybridize with complementary strands not conjugated to protein. As these oligonucleotides are relatively short (20 bases), this DNA starting material can also be easily purified by size exclusion chromatography.

After this multi-step conjugation and purification scheme, we finally produce an antibody conjugated to a ssDNA molecule intended to hybridize to a complementary strand immobilized on a glass substrate. We demonstrated the robustness of this strategy by patterning 4 different ssDNA molecules on a glass substrate, conjugating the complementary strands to 4 different fluorescent antibodies, and simply incubating the glass substrate with an aqueous solution containing a diluted amount of each of these antibody-olignucleotide complexes (**Fig. 5-03**). This strategy can generate patterns of several antibodies with high resolution, demonstrating its power and utility.

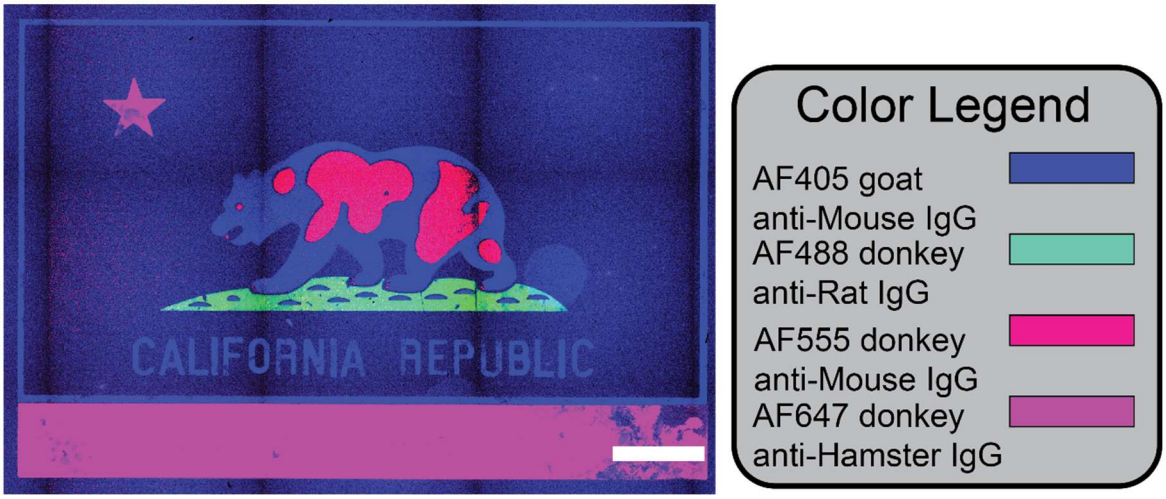

Figure 5-03: Proof-of-concept, high-resolution patterning of four fluorescent antibodies (Alexa Fluor 405 goat anti-Mouse IgG antibody, Alexa Fluor 488 donkey anti-Rat IgG, Alexa Fluor 555 donkey anti-Mouse IgG antibody, and Alexa Fluor 647 goat antiHamster IgG) in a complex geometry. Scale bar = 500 µm.

DNA-directed patterning of antibodies for label-free surface-marker screening

The ability to pattern antibodies also enables label-free screening of cell-surface markers using microfluidic techniques such as node-pore sensing[4]. As described previously, node-pore sensing is based on measuring the modulated current that is caused by a cell transiting a microfluidic channel that has been segmented by nodes (**Fig. 5-03**)[4,7]. If segments between nodes are functionalized with antibodies, a cell that expresses surface markers that can transiently interact with those antibodies will transit more slowly through these segments. Cell transit times are reflected in the duration of the subpulses that correspond to the cell transiting specific segments. Here, we designed and fabricated a next-generation, surface-marker screening NPS device in which we use DNA-directed patterning to pattern a saturating concentration of antibodies to the microfluidic channel segments (**Fig. 5-04**).

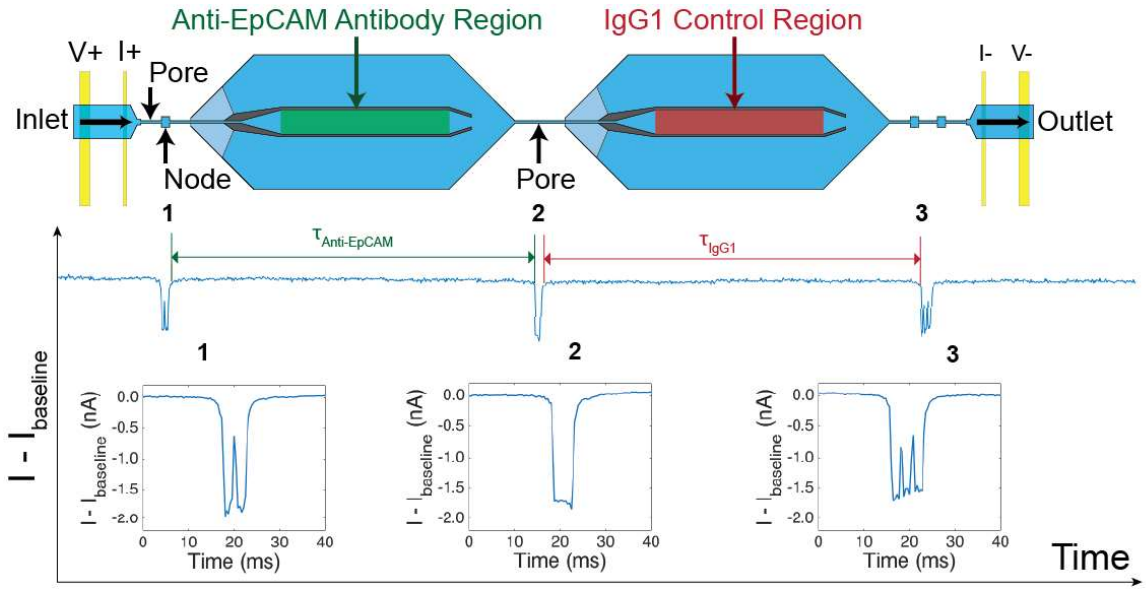

Figure 5-04: Top: Enlarged, top-down view of the NPS layout, including measurement electrodes spanning a microfluidic channel segmented with nodes and with two antibody functionalized regions (EpCAM and IgG1). Bottom: current pulses generated when a cell transits (1) the 2-pore, 1-node sequence before the first antibody region, (2) the single pore between antibody regions, and (3) the 3-pore, 2-node sequence after the second antibody region. Anti-EpCAM region transit time (τ_{EpCAM}) is defined as the time between pulses caused by a cell transiting between (1) and (2), and IgG1 control region transit time (τ_{IgG1}) is defined as the time between pulses caused by a cell transiting between (2) and (3). Inset: representative current traces as an MCF-7 cell passes through the different regions of the NPS device.

To demonstrate label-free surface-marker screening, we flowed MCF-7 and Jurkat cells through an NPS device that had been patterned with anti-EpCAM antibody and a mouse IgG1 isotype control antibody. Specific interactions between the EpCAM surface marker highly expressed on the surface of MCF-7 cells and patterned anti-EpCAM antibody led to significantly longer transit times ($p < 0.0001$) in the anti-EpCAM antibody region (677 ± 124 ms) as compared to those in the IgG1 control region (428 ± 110 ms) (**Fig. 5-05A**). In contrast, Jurkat cells, which do not express EpCAM, did not specifically interact with

the patterned anti-EpCAM antibodies and their transit times (1001 ± 396 ms) were not significantly different (p = 0.203) from those of the IgG1 control region (1112 ± 483 ms) (**Fig. 5-05A**). By normalizing EpCAM transit times to those of the isotype control, we were able to distinguish MCF-7 cells from Jurkat cells based on EpCAM expression (**Fig. 5-05B**). We derived a logistic regression model from this data and generated a receiver operating characteristic (ROC) curve, achieving an area-under-the-curve of 0.933 for MCF-7 (**Fig. 5-05C**). This statistic represents the probability of ranking an MCF-7 cell higher than a Jurkat cell, where high-ranking events are classified as EpCAM-positive.

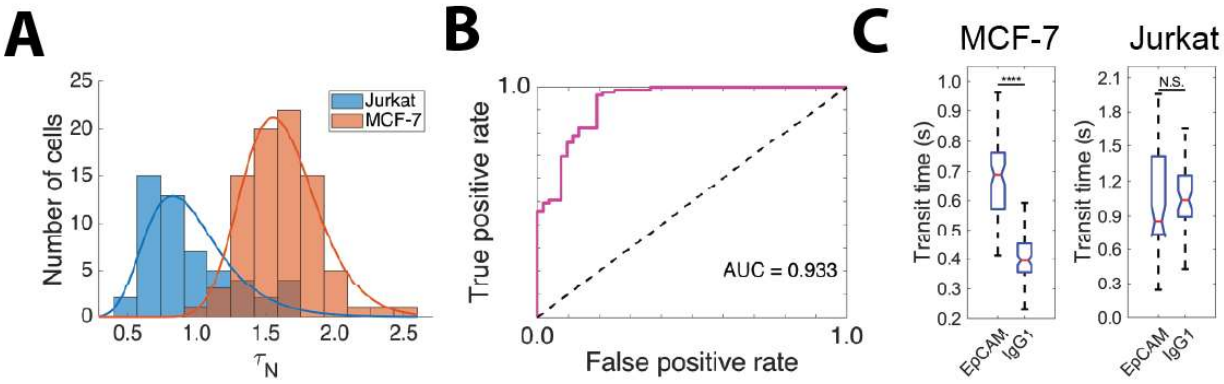

Figure 5-05: (A) Box plots of MCF-7 (left) and Jurkat (right) transit times as these cells traverse the anti-EpCAM-patterned and IgG1-patterned regions (MCF-7: n = 85 cells, p < 0.0001; statistical significance determined by a two-sample Student's t-test. Jurkat: n = 52 cells, p = 0.203; statistical significance determined by a two-sample Student's t-test). **(B)** Histogram of normalized transit times ($\tau_N = \tau_{EpCAM}/\tau_{IgG1}$) for MCF-7 (n = 85 cells) and Jurkat (n = 52 cells). Lines represent log-normal distributions fitted to MCF-7 and Jurkat data. **(C)** Receiver operating characteristic curve for a logistic regression model derived from transit time ratios. The curve demonstrates the trade-off between true positive and false positive rates of classifying cells as EpCAM-positive. An area-under-the-curve of 0.933 is indicative of excellent overall classifying performance.

To further display the multiplexing capabilities of our method, we used our next-generation NPS device to screen MCF-10A, MCF-7, and Hs 578T cells for EMT-associated surface markers. In EMT, epithelial proteins such as E-Cadherin are down-regulated and mesenchymal proteins such as N-Cadherin and integrin β1 are upregulated, conferring properties that are advantageous to the migration processes involved in development, wound healing, and metastasis[8]. In larger NPS devices that accommodated four antibody regions (**Fig. 5-06**), we patterned anti-E-cadherin, anti-N-cadherin, and anti-integrin β1 in the first three regions of each device, and a mouse IgG1 isotype control antibody as a negative control in the last region. **Fig. 5-07** shows the mean normalized transit times of MCF10A, MCF-7, and Hs 578T cells. As shown, MCF-7 cells showed significantly greater interaction with anti-E-cadherin antibodies (p < 0.0001), reflecting their more epithelial phenotype. Conversely, Hs 578T cells showed greater interaction with anti-N-cadherin antibodies (p = 0.0010 vs. anti-E-cadherin, p < 0.0001 vs. anti-integrin β1), reflecting their more mesenchymal phenotype. Finally, MCF10A cells did not show greater interaction with any of the three antibody types (p = 0.30 E-cadherin vs. N-cadherin; p = 0.21 E-cadherin vs. integrin β1; p = 0.97 N-cadherin vs. integrin β1).

It is expected that the transformed epithelial cell line MCF-10A would not express mesenchyme-associated N-cadherin. The lack of E-cadherin or integrin β1 expression may be due to specific culture conditions where the formation of cell-cell junctions and expression of ECM-adhesion proteins are not highly promoted as they would in a dense 3D culture system such as Matrigel[9]. **Fig. 5-08** shows the surface marker expression of single cells (MCF10A, MCF-7, and Hs 578T) as determined by NPS. Single cells show a wide range of expression for the three surface markers screened, with epithelial MCF-7 cells being more likely to express E-cadherin and mesenchyme-like Hs 578Ts being more likely to express N-cadherin. Our single-cell perspective revealed a subpopulation of epithelial MCF-10A cells that had a substantial interaction with anti-E-cadherin antibodies.

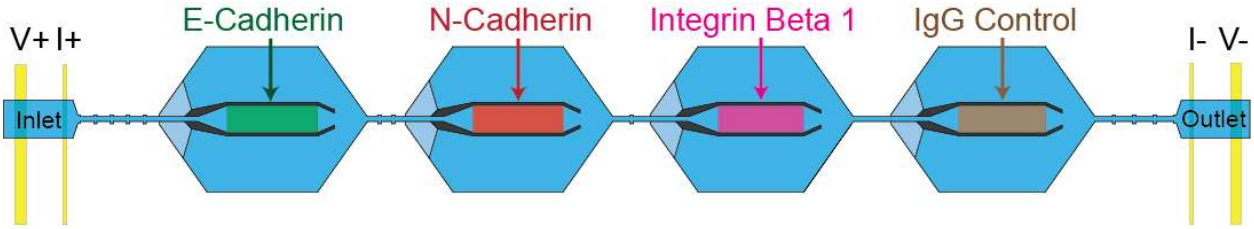

Figure 5-06: Top-down view of NPS device for EMT marker screening, including measurement electrodes and a microfluidic channel segmented with nodes and with four antibody functionalized regions (anti-E-cadherin, anti-N-cadherin, anti-integrin β1, and IgG1).

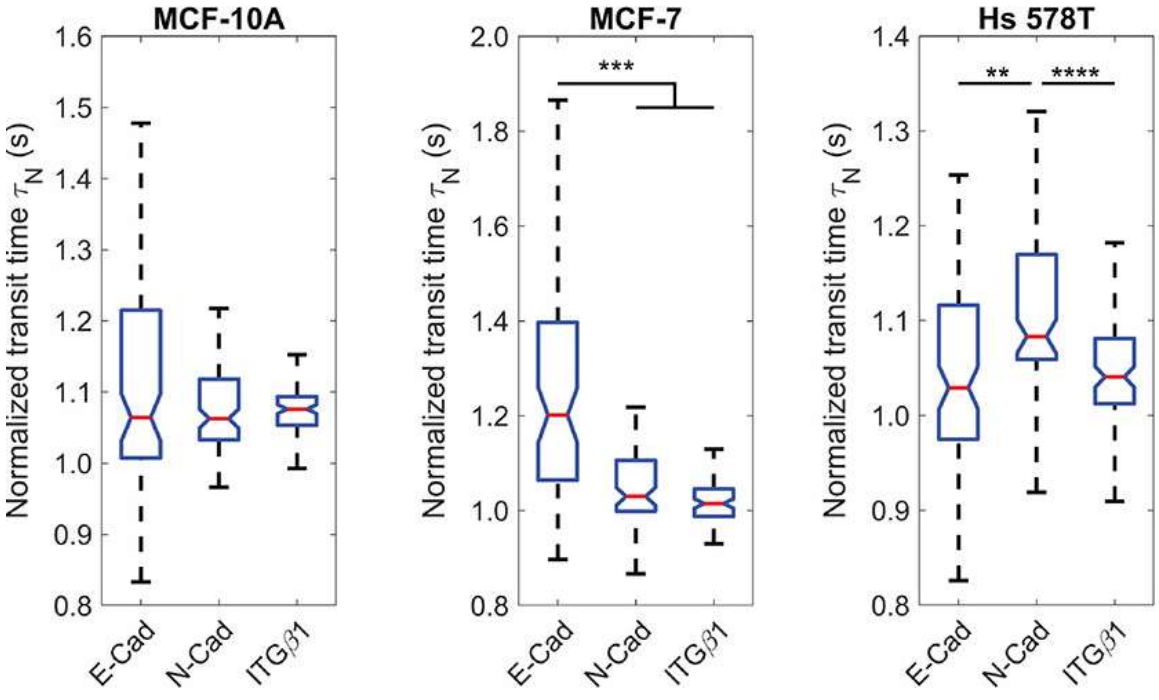

Figure 5-07: Box plots of normalized transit times of MCF-10A cells (left), MCF-7 cells (center), and Hs 578T cells (right) as they pass through E-cadherin, N-cadherin, and integrin β1 antibody regions. Statistical significance was determined by a Tukey method for multiple comparisons; ** $p < 0.01$, *** $p < 0.001$; **** $p < 0.0001$. (MCF-10A: n = 99 cells. MCF-7: n = 81 cells. Hs 578T: n = 96).

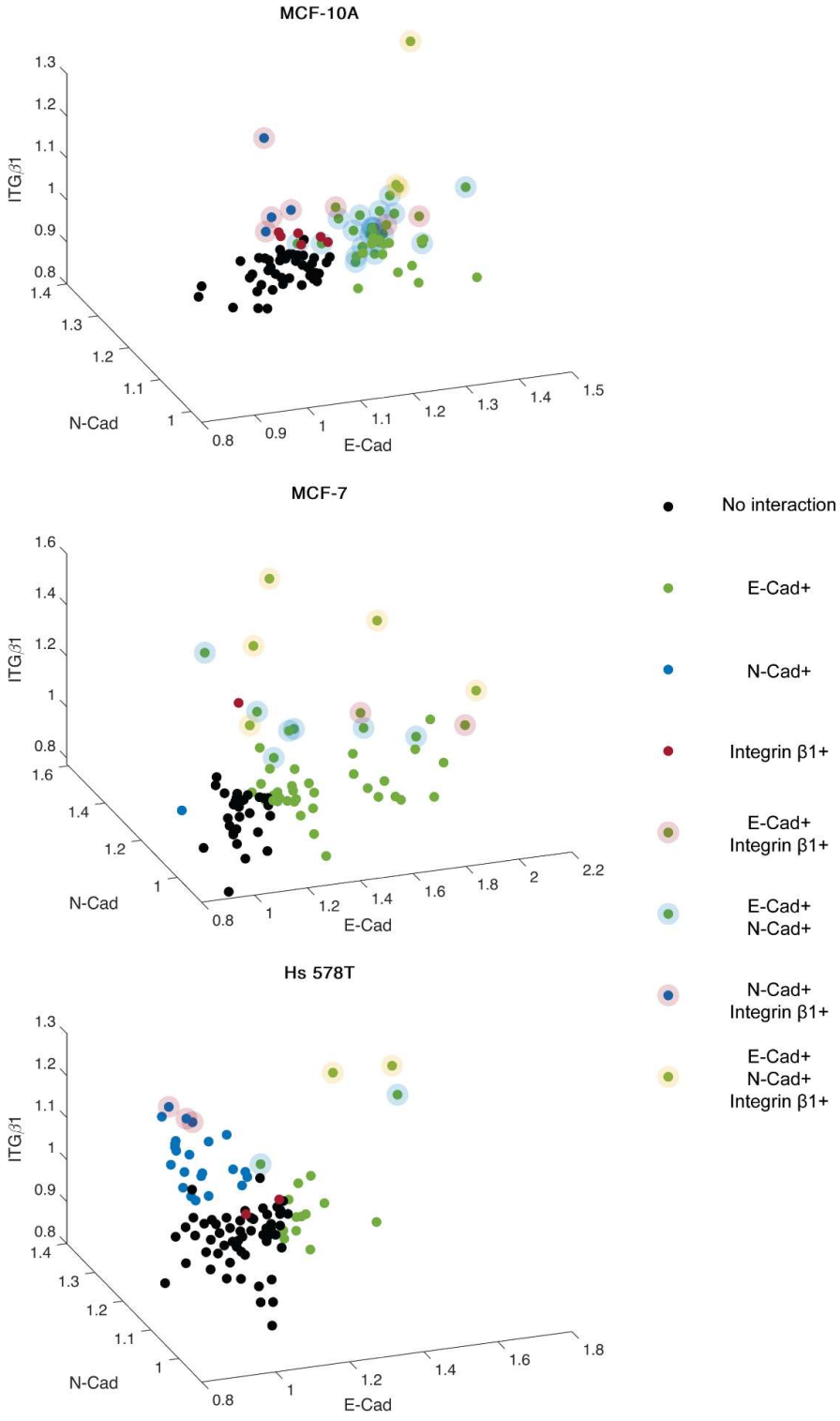

Figure 5-08: Scatter plots of single-cell transit times through E-cadherin, N-cadherin, and integrin β1 antibody regions for MCF-10A cells (top), MCF-7 cells (center), and Hs 578T cells (bottom). A single cell was considered to have a substantial interaction with an antibody if its transit time through the antibody-patterned region was slower than its transit time through the control region by more than one standard deviation. (MCF-10A: n = 99 cells. MCF-7: n = 81 cells. Hs 578T: n = 96).

Consequently, antibody patterning of NPS devices can be used as a label-free means to accurately determine the presence of particular surface markers on a single cell based on its normalized transit times through antibody-patterned regions. Given the ease with which we can pattern antibodies using DNA-directed patterning, antibodies can be sequentially patterned within the NPS microfluidic device to enable immunoscreening of multiple surface markers expressed by individual cells. Our results, thus, demonstrate the flexibility of DNA-directed antibody patterning in its ability to not only separate cell populations via cell capture but also to enable label-free screening of specific surface markers.

5.3 Materials and Methods

Cell culture: MCF-7, Jurkat, MCF-10A, and Hs 578T cell lines were obtained from the University of California, Berkeley Cell Culture Facility. Jurkat cells were cultured in RPMI 1640 with 10% FBS and 1% AA and maintained at 37°C with 5% CO_2. MCF-7, MCF-10A, and Hs 578T cells were cultured in DMEM with 10% FBS and maintained at 37 °C with 5% CO_2.

Preparation of oligonucleotide-antibody conjugate using dibenzocyclooctyne (DBCO)-PEG_5-N-hydroxysuccinimide (NHS) ester heterobifunctional crosslinker: Immediately before use, DBCO-PEG_5-NHS crosslinker was prepared as a 10 mM solution in anhydrous dimenthylsulfoxide, and 100 µg of the antibody-of-interest was buffer exchanged using a 50 kDa Amicon Ultra-0.5 mL Centrifugal in 200 mM sodium bicarbonate in 18 MΩ deionized (DI) water. For Tris-HCl quenching, a 4-fold molar excess of the sodium azide concentration (as listed by the vendor) was added to the antibody solution prior to buffer exchange. The crosslinker was added at a 32-fold molar excess to the solution containing the antibody of interest, and the reaction was allowed to proceed for 2 hours on a shaker at room temperature. Unreacted DBCO crosslinker was then removed using a Centri-Spin 40. A second reaction step was conducted by reacting the DBCO-antibody conjugate with an azide-terminated oligonucleotide at a 1:2 molar ratio overnight at room temperature on a tube rotator. The subsequent oligonucleotide-antibody complex was then purified from free azide-terminated oligonucleotide using a Centri-Spin 40.

Node-pore sensing device fabrication: Node-pore sensing (NPS) devices, designed by N. K. Liu, consist of PDMS-molded microfluidic channels bonded to glass substrates with microfabricated electrodes. The microfluidic channels were fabricated using soft lithography. Specifically, a negative-master mold consisting of two overlaid SU-8 resist feature layers was lithographically patterned onto a polished silicon (Si) wafer. The first layer was created by spin coating SU-8 3010 resist at 3000 RPM for 30s (to create a 10 µm-thick resist layer) and then soft baked for 3 min at 95°C. The SU-8-coated Si wafer was then patterned with a Mylar mask via UV light (365 nm; 27s at 9.5 mW/cm^2) and subsequently baked for 3 min at 95°C. Without developing this first layer, SU-8 3025 photoresist was then spin-coated onto the Si wafer at 2500 RPM for 30s (to create a 30 µm-thick resist layer) and soft baked for 10 min at 95°C. The wafer was again UV

patterned (365 nm; 27s at 9.5 mW/cm^2) with a different Mylar mask that had been appropriately aligned to the first mask using previously defined substrate alignment markers and baked for 4 min at 95°C. Both SU-8 layers were simultaneously developed in SU-8 developer for 6 min. After development, the negative master mold was hard-baked for 15 min at 150°C to increase the durability of the SU-8 features. Following the fabrication of the negative master, PDMS was mixed at a ratio of 10:1 Sylgard 184 prepolymer base to curing agent and degassed in a vacuum desiccator for 30 minutes. The PDMS was then poured onto a negative-master mold and subsequently cured in a convection oven for at least 4 hours at 85°C. Once cured, the PDMS was then peeled from the negative-master mold and inlet and outlet ports were punched using a 1.5 mm diameter biopsy punch.

Metal electrodes were patterned onto aldehyde-functionalized glass slides using standard microfabrication techniques. Microposit S1813 photoresist was spin-coated onto the slides at 3000 RPM for 30s and soft baked on a hotplate for 1.5 min at 100°C. The slides were then UV-exposed to a Mylar mask (365 nm; 34s at 9.5 mW/cm^2) and developed using MF-321 developer. Electron-gun evaporation was used to deposit a thin film of titanium (50 Å) and gold (400 Å). After excess metal was lifted off with acetone, the slides were cleaned with DI water and dried with dry N_2 gas. Surface patterning of oligonucleotides (see Section 2.5) was subsequently performed to pattern oligonucleotide-conjugated antibodies onto the slides. A protective layer of 1.3 µm S1813 photoresist was patterned over regions containing oligonucleotides prior to PDMS bonding.

To bond the NPS microfluidic channels to the electrode-antibody-patterned slides, both the PDMS channels and slides were exposed to an RF oxygen plasma (5 ccm O_2 flow rate, 420 mTorr chamber pressure, power = “high”; Harrick Plasma, PDC-001). Resist used to protect oligonucleotides was stripped using acetone prior to bonding. Permanent bonding was achieved by heating the PDMS-glass devices on a hotplate at 100°C for 10 min, thereby completing the NPS devices.

Statistical analysis: To compute the statistical significance of differences in transit time measured by NPS, we used a two-sample Student’s t-test (2-antibody region devices) or a Tukey method for multiple comparisons (4-antibody region devices). For logistic regression of transit time ratios, data from MCF-7 and Jurkat NPS measurements were assigned an “EpCAM-positive” and “EpCAM-negative” classification, respectively. Using MATLAB, we generated a logistic regression model on EpCAM expression classification data. From the classifier predictors, we then plotted a receiver operating characteristic (ROC) curve for classification of cell events as “EpCAM-positive.”

5.4 Conclusions

Here, we demonstrated a novel method for functionalizing microfluidic devices with antibodies. DNA-directed patterning enables one-shot immobilization of several antibodies along precise geometric patterns. Because of the specificity of DNA base-pairing, antibodies are confined to a single region with minimal cross-contamination into

other patterns. Since these antibodies are only immobilized just prior to cell surface marker analysis, this same DNA-directed patterning process can be used with any combination of antibodies for cell subpopulation analysis; all that is needed is to conjugate the antibodies of interest with the combination of ssDNA strands. We have demonstrated that this technology is ready for a broad variety of surface marker screening panels for label-free analysis via NPS.

5.5 References

1. Nagrath, S. *et al.* Isolation of rare circulating tumour cells in cancer patients by microchip technology. *Nature* **450**, 1235–1239 (2007).
2. Barriere, G. *et al.* Circulating tumor cells and epithelial, mesenchymal and stemness markers: characterization of cell subpopulations. *Ann. Transl. Med.* **2**, 109 (2014).
3. Scheideler, O. J. *et al.* Recapitulating complex biological signaling environments using a multiplexed, DNA-patterning approach. *Sci. Adv.* **6**, eaay5696 (2020).
4. Balakrishnan, K. R. *et al.* Node-Pore Sensing Enables Label-Free Surface-Marker Profiling of Single Cells. *Anal. Chem.* **87**, 2988–2995 (2015).
5. Baskin, J. M. *et al.* Copper-free click chemistry for dynamic in vivo imaging. *Proc. Natl. Acad. Sci.* **104**, 16793–16797 (2007).
6. Anderson, G. W., Callahan, F. M. & Zimmerman, J. E. Synthesis of N-Hydroxysuccinimide Esters of Acyl Peptides by the Mixed Anhydride Method. *J. Am. Chem. Soc.* **89**, 178–178 (1967).
7. Balakrishnan, K. R. *et al.* Node-pore sensing: a robust, high-dynamic range method for detecting biological species. *Lab Chip* **13**, 1302 (2013).
8. Dongre, A. & Weinberg, R. A. New insights into the mechanisms of epithelial–mesenchymal transition and implications for cancer. *Nat. Rev. Mol. Cell Biol.* **20**, 69–84 (2019).
9. Griffith, L. G. & Swartz, M. A. Capturing complex 3D tissue physiology in vitro. *Nat. Rev. Mol. Cell Biol.* **7**, 211–224 (2006).

Chapter 6: Conclusions and Future Work

6.1 Summary of presented work and principal findings

This dissertation presents a body of work wherein novel microfluidic technologies—all based on node-pore sensing—for biomarker discovery were discussed. In Chapter 2, we explained several theoretical considerations behind these techniques, where this theory drives both the operating principles and design criteria for the node-pore sensing devices we used. In Chapter 3, we described practical concerns of device design, operation, and optimization. We concluded Chapter 3 by presenting work where we tested the reliability and reproducibility of mechano-NPS devices, ultimately providing an example of critical characterization work and engineering analysis of our technology. In Chapter 4, we presented an unmet need in biomedicine where drug resistance (to ATRA) in acute promyelocytic leukemia (APL) could not be described with existing biomarkers. To tackle this problem, we analyzed APL cells and their responses to ATRA using mechano-NPS, looking for mechanical phenotypes associated with the drug resistant phenotype. We ultimately found that a positive response to this drug is associated with cell softening and investigated several potential mechanisms by which this softening is achieved. We proposed that the organization of the nucleus and packing density of chromatin may be major drivers of APL cell mechanical properties, and that the latter factor may also influence how the cells respond to ATRA. In Chapter 5, we presented a novel method for functionalizing microfluidic devices with antibodies. This new strategy is flexible, multiplexable, and highly specific, allowing for precise patterning of antibodies in specific geometric arrangements. We demonstrate the power of this new technique with two proof-of-concept experiments where we analyzed several cell populations for surface proteins.

Altogether, the work described in this dissertation demonstrates advancements in microfluidic technology that allow us to more readily analyze single cells for mechanical properties and the expression of surface proteins. With further validating work, both mechanical properties and surface proteins can become hallmark biomarkers of different phenotypes such as drug resistance, or transformations such as epithelial-to-mesenchymal transitions. Ultimately, these advancements in node-pore sensing will enable future exploration of biomarkers in the topics of drug resistance or cancer metastasis, as well as in other biomedically relevant topics.

6.2 Future work

6.2.1 Genomic screens for investigating the contribution of single genes to mechanical phenotype

While we presented one method of investigating the mechanical phenotypes of cells in Chapter 4, we unfortunately could not pinpoint a specific mechanism for how our APL cells softened or responded to ATRA, and how these two are related. We highlighted several transcriptional changes that occur due to ATRA or TSA treatment with RNA-Seq, however due to the sheer volume of data, this kind of measurement is inherently noisy. As such, it is difficult to draw concrete conclusions about how the differential expression

of certain genes might lead to cell softening or stiffening. A more granular measurement of how transcriptional regulation might affect cell mechanics could perturb individual genes. By modulating the expression of a single gene, we could then analyze those cells with mechano-NPS to determine how any gene affects mechanical phenotype.

To accomplish such a task, we devised a method using Cas9-based gene editing[1,2]. Cas9 has been used to great effect to specifically knock out individual genes, and the development of lentiviral, whole-genome libraries has allowed researchers to perform knock-out experiments across the entirety of the human genome [3]. Incorporation of this library into the lentiviral packaging process produces a pool of viruses capable of inserting transgenic complementary DNA into host cell genomes, where this DNA contains the instructions to prevent the expression of one host (human) gene per cell. This integration involves a few critical genes: (1) the Cas9 enzyme itself, (2) single-stranded guide RNA (sgRNA, or "guides"), and (3) an antibiotic selection marker. The first two components cause the host cell to express the components for Cas9 to cut DNA at a specific location determined by the sgRNA sequence. This nuclease activity is targeted toward a specific gene in the host cell's genome, and so the aforementioned library includes multiple guides to cover the whole genome. By cutting the host DNA at a specific gene, that gene is no longer capable of being transcribed into a functional gene product (i.e., protein), thus knocking it out.

To study how the knockout of individual genes affects the cells, each cell should have, at most, one integration event. The relationship between the dose of virus particles and how many genes are knocked out is described by Poisson statistics [4]. As such, to ensure that a sufficiently small number of cells experience two integration events, the viral dose is made such that in actuality, the majority of cells do not have viral DNA integrated at all. Since we are interested in studying the cells where a successful knockout occurred, an antibiotic selection marker (e.g., for puromycin) is included to selectively kill cells that did not also receive the Cas9-sgRNA DNA and have thus not knocked out any genes. With all of this in consideration, we applied these methods to a pool of MDA-MB-231 breast cancer cells and generated a cell line that stably expresses Cas9 and can be freely transfected with sgRNA through methods such as nucleofection[5].

Because the whole-genome library knocks out genes across the whole genome, there will be several thousand genes knocked out across all the cells that remain after antibiotic selection. To determine which of these genes are relevant to mechanical phenotype requires additional selection, as some of these knockout events may affect cell mechanical properties, and some may not. Fortunately, it is well-known that cell deformability is associated with cancer metastasis, and this relationship has even been directly measured in prior work[6–11]. Therefore, to separate those genes that affect mechanics vs. those that do not, we proposed to use a transwell migration assay, wherein cells that migrate are more likely to be softer, and cells that do not migrate are more likely to be stiffer. The physical separation of migratory vs. non-migratory cells allows us to make several important measurements.

First, we can directly measure the pool of migratory and non-migratory cells with mechano-NPS, and evaluate whether migrating cells are indeed, on average, softer than non-migrating cells. However, for such a measurement, it would not be known what gene was knocked out and whether this promotes or discourages migration. To answer this question, we can isolate the guides from the cells in each pool and sequence them to determine the relative abundance of specific sgRNA in the migratory vs. non-migratory pool. Through bioinformatic analysis, we can quantify which guides are the most enriched in both the migratory and non-migratory pools; these "hits" constitute the genes most likely to affect migration, and thus mechanical phenotype. As such, we can generate a list of genes that may be the most relevant to controlling cell mechanical properties, massively narrowing down the experimental space if we are indeed to analyze the contributions of individual genes to mechanical properties.

From here, we can generate new cell lines with lentivirus doses providing only one guide, allowing us to grow cells with only one gene knocked out. We can then go down our list of hits, knocking out individual genes as such, and analyzing each single-gene knockout line with mechano-NPS. At the end of this hit validation, we will have quantified how each of these genes alone affects mechanical phenotype – work that has never before been investigated, and would help reveal some of the mechanisms by which "mechanical biomarkers" can be associated with phenotypes/phenomena such as metastasis.

6.2.2 Quantification of tumor-associated extracellular vesicles via immunoprecipitation and lipid-inserting oligonucleotide labels

Another source of potential biomarkers are extracellular vesicles, or small, circulating, cell-derived vesicles that arise as a byproduct of endocytosis and are widely believed to be used for cell-to-cell signaling [12]. As these vesicles are derived from cell plasma membranes, they necessarily contain proteins from the membrane of their cell of origin. As such, there is great interest in using extracellular vesicles as a via to identifying cells that may be difficult to access, such as a deeply-embedded tumor where a direct biopsy is surgically dangerous [13].

Specific capture of extracellular vesicles, then, is accomplished much like specific capture of circulating tumor cells – often, some form of immunocapture is used to isolate tumor-derived cells or vesicles based on the expression of a tumor-associated protein. However, while cells are large enough to be easily analyzed after immunocapture, extracellular vesicles are approximately two orders of magnitude smaller than cells, making traditional methods of cell analysis incompatible with extracellular vesicles. In fact, even simple quantification of the number of vesicles captured is no simple task, and requires highly specialized instrumentation usually reserved for advanced characterization of synthetic nanoparticles.

One way to quantify the capture of vesicles was described by Kozminsky *et al.* wherein ssDNA labels are conjugated to cholesterol so that they readily insert into lipid bilayers [14–16]. Thus, following Carey *et al.*[15], we investigated whether we could use this strategy to quantify the immunocapture of extracellular vesicles. If so, using an antibody against a tumor-associated marker for immunocapture, we could then recognize an increase in

vesicle capture as a sign of a greater titer of tumor-associated markers, itself a hint as to the presence of some form of cancer.

As with most immunocapture and immunoprecipitation strategies, the pulldown of tumor-associated extracellular vesicles is accomplished with paramagnetic beads coated with streptavidin, to which a biotinylated antibody is attached. By mixing these antibody-coated beads with the sample, any particle or protein that the antibody targets will be bound to the paramagnetic bead. These beads can be isolated from the rest of the fluid sample with a magnetic field designed to immobilize the beads while the surrounding fluid is aspirated and exchanged, washing the immunoprecipitation product – in this case, beads that have captured extracellular vesicles containing the protein of interest on their surfaces.

Unique to this immunocapture workflow is the addition of cholesterol-conjugated ssDNA labels, which will nonspecifically embed themselves into the membranes of all vesicles. Assuming even labeling of every vesicle with DNA, downstream quantification of the DNA (via qPCR) on the immunoprecipitation product provides a proxy method for quantifying the number of vesicles captured with antibodies. Here, we present several noteworthy factors that affect the specificity of this assay.

We first observed that even in a negative control sample containing phosphate-buffered saline and no vesicles, there was a significant number of qPCR products, indicating non-specific binding of DNA labels to the immunocapture substrate. To minimize this, we first evaluated whether a small amount of Triton-X 100 surfactant would reduce this binding by disrupting non-covalent interactions. Performing this experiment, we eventually found that Triton-X 100 was only successful in preventing DNA label absorption if vesicles were isolated from culture media not containing serum (**Fig. 6-01**). This suggests to us that in the process of isolating extracellular vesicles (using the QIAGEN exoEasy kit), some component(s) of the serum used to supplement cell growth medium are eluted with the vesicles and promote non-covalent binding of DNA labels to the paramagnetic beads, where this binding can be disrupted with a surfactant. Interestingly, digestion of any serum-derived protein adsorbed to the beads via incubation with 0.25% trypsin had no effect on the absorption of DNA labels.

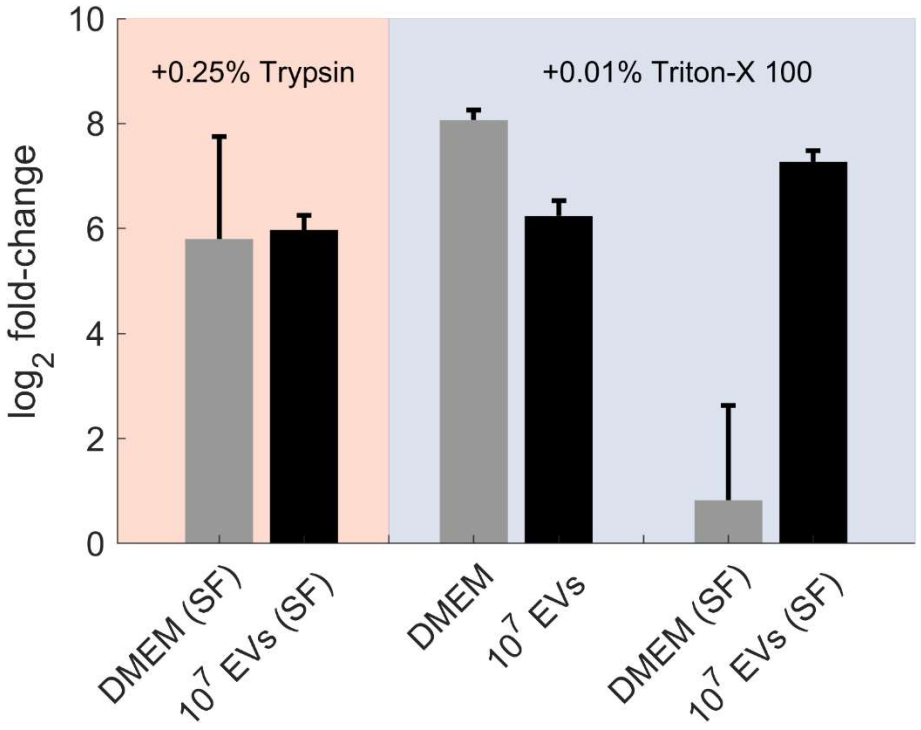

Figure 6-01: Log_2-fold change in qPCR products for conditions testing the absorption of DNA labels to immunocapture beads. Samples used for immunocapture were either serum-free culture media (DMEM (SF)), serum-supplemented culture media (DMEM), or 10^7 EVs isolated from culture medium with (10^7 EVs) or without (10^7 EVs (SF)) serum. Samples were either treated with 0.25% trypsin to digest fouling protein, or with 0.01% Triton-X 100 to disrupt non-covalent interactions.

We next evaluated the specificity of our immunocapture, or to what degree the antibody or beads absorbed vesicles not containing the protein targeted by the antibody. We first tested a situation where the antibody does indeed target a protein on the vesicles' cell line of origin, showing that the readout of qPCR products is dose dependent (**Fig. 6-02**). However, in repeating this test with the same antibody, but with a sample of vesicles isolated from cells not containing the protein of interest, we saw a similar number of qPCR products and the same dose-dependent change (**Fig. 6-02**). In fact, even when performing an identical experiment but with no antibody on the beads' surface, which should result in no specific or non-specific immunocapture, we saw similar results (**Fig. 6-03**).

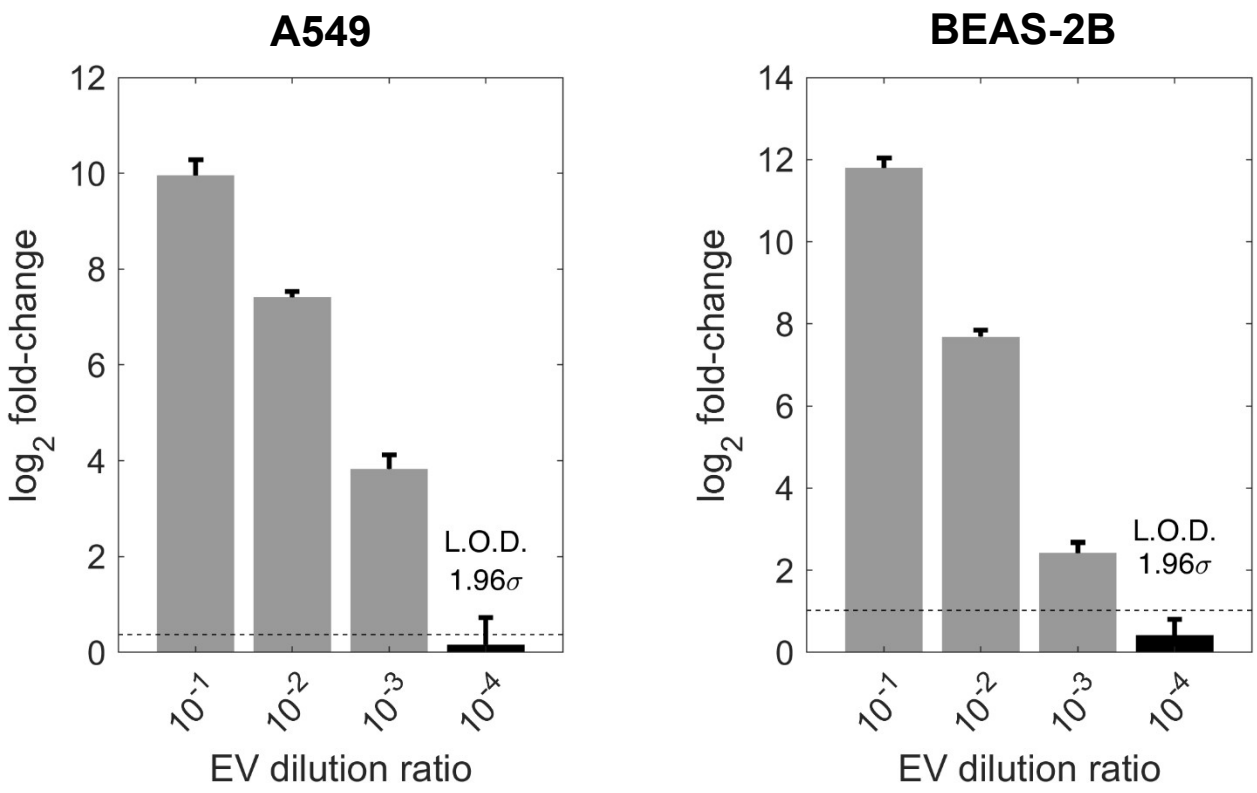

Figure 6-02: Log_2-fold change in qPCR products for conditions testing the specificity of immunocapture with beads functionalized with an antibody against CA12, a lung cancer-associated surface protein. (Left) qPCR results for a dilution series of EVs isolated from A549, a cell line expressing CA12. (Right) qPCR results for a dilution series of EVs isolated from BEAS-2B, a cell line not expressing CA12.

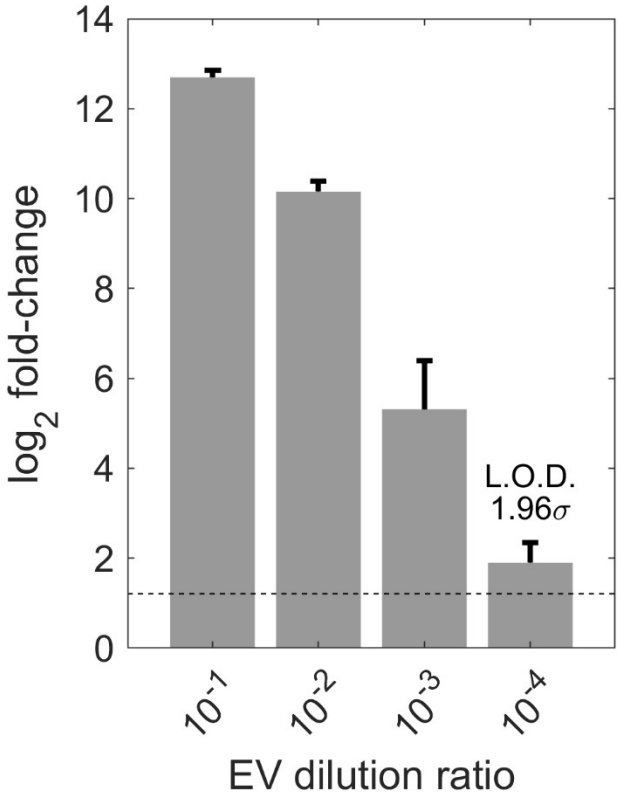

Figure 6-03: Log_2-fold change in qPCR products for a negative control for immunocapture, using beads not functionalized with any antibody, but still coated for streptavidin. EVs from BEAS-2B were isolated, diluted, labeled with ssDNA, and added to streptavidin-coated beads with the intention of observing the capture of labeled EVs or DNA labels not mediated by immunocapture.

Taken together, these results demonstrate that the amplification and quantification of qPCR products from the DNA labels is not associated with specific immunocapture of vesicles at all. This is not to say that *no* vesicles are specifically immunocaptured, but that the background of either labeled vesicles or free DNA labels overwhelms any signal that could be measured from immunocaptured vesicles. Based on these results, especially those in **Fig. 6-03** demonstrating that streptavidin-coated beads still have a substantial amount of absorbed labels, we recommend looking to other strategies to functionalize the immunocapture substrate with antibodies, and to further passivate the bead surface with a relatively inert species such as polyethylene glycol.

Finally, these two pieces of future work outlined in Chapter 6, Section 2 represent additional avenues of research to further explore the broader topic of biomarker discovery. The genomic screen we have begun constitutes supporting work for Chapter 4 and is a direct supplement to the use of mechano-NPS to analyze cells for mechanical biomarkers. The detection of extracellular vesicles with oligonucleotides and qPCR is in itself not directly related to a node-pore sensing technique, but instead constitutes another method of biomarker discovery, wherein the proteins of extracellular vesicles are

analyzed instead of those on the surface of cells. Nevertheless, these two directions represent future topics that can be more fully explored to either support or directly contribute to our knowledge of biomarkers.

6.3 References

1. Sanjana, N. E., Shalem, O. & Zhang, F. Improved vectors and genome-wide libraries for CRISPR screening. *Nat. Methods* **11**, 783–784 (2014).
2. Prolo, L. M. *et al.* Targeted genomic CRISPR-Cas9 screen identifies MAP4K4 as essential for glioblastoma invasion. *Sci. Rep.* **9**, 14020 (2019).
3. Shalem, O. *et al.* Genome-Scale CRISPR-Cas9 Knockout Screening in Human Cells. *Science (80-.).* **343**, 84–87 (2014).
4. Fehse, B., Kustikova, O. S., Bubenheim, M. & Baum, C. Pois(s)on – It's a Question of Dose…. *Gene Ther.* **11**, 879–881 (2004).
5. Distler, J. H. W. *et al.* Nucleofection: a new, highly efficient transfection method for primary human keratinocytes*. *Exp. Dermatol.* **14**, 315–320 (2005).
6. Byun, S. *et al.* Characterizing deformability and surface friction of cancer cells. *Proc. Natl. Acad. Sci. U. S. A.* **110**, 7580–7585 (2013).
7. Gossett, D. R. *et al.* Hydrodynamic stretching of single cells for large population mechanical phenotyping. *Proc. Natl. Acad. Sci. U. S. A.* **109**, 7630–7635 (2012).
8. Kim, J. *et al.* Characterizing cellular mechanical phenotypes with mechano-node-pore sensing. *Microsystems Nanoeng.* **4**, 1–12 (2018).
9. Tse, H. T. K. *et al.* Quantitative diagnosis of malignant pleural effusions by single-cell mechanophenotyping. *Sci. Transl. Med.* **5**, (2013).
10. Guck, J. *et al.* Optical deformability as an inherent cell marker for testing malignant transformation and metastatic competence. *Biophys. J.* **88**, 3689–3698 (2005).
11. Rianna, C., Radmacher, M. & Kumar, S. Direct evidence that tumor cells soften when navigating confined spaces. *Mol. Biol. Cell* **31**, 1726–1734 (2020).
12. Alberts, B. *et al. Molecular Biology of the Cell*. (W.W. Norton & Company, 2017). doi:10.1201/9781315735368.
13. Nanou, A. *et al.* Tumour-derived extracellular vesicles in blood of metastatic cancer patients associate with overall survival. *Br. J. Cancer* **122**, 801–811 (2020).
14. Kozminsky, M., Carey, T. R. & Sohn, L. L. DNA-Directed Patterning for Versatile Validation and Characterization of a Lipid-Based Nanoparticle Model of SARS-CoV-2. *Adv. Sci.* 2101166 (2021) doi:10.1002/advs.202101166.
15. Carey, T. R. Detection and Characterization of Lipid Bilayer Nanoparticles. PhD Thesis (University of California, Berkeley, 2021).
16. Carey, T. R. *et al.* Detecting Intact SARS-CoV-2 Using Exogeneous Oligonucleotide Labels. *medRxiv* (2021).

Appendices

Appendix 01: Lilliefors tests for mechanical phenotyping data to determine distribution normality.

wCDI

	p
Device 1	0.0029
Device 2	0.0011
Device 3	0.001*
Device 4	0.0047
Device 5	0.0278
Device 6	0.0446
Device 7	0.001*

Recovery time constant τ

	p
Device 1	0.0014
Device 2	0.3828
Device 3	0.001*
Device 4	0.001*
Device 5	0.001*
Device 6	0.1285
Device 7	0.0024

The whole-cell deformability index *wCDI* (left) and recovery time constant *τ* (right) of AP-1060 cells measured on three different mechano-NPS devices were tested for normality using a Lilliefors test. A p-value less than 0.05 indicates a failure to reject the null hypothesis that the distribution of *wCDI* or recovery time constant for that device came from a normal distribution with an unspecified mean and standard deviation. *The test statistic exceeded the tabulated values in the MATLAB R2020a implementation of the Lilliefors test.

Appendix 02: Two-sample Kolmogorov-Smirnov tests to compare *wCDI* distributions from replicate devices.

	Dev. 1	Dev. 2	Dev. 3	Dev. 4	Dev. 5	Dev. 6	Dev. 7
Dev. 1							
Dev. 2	0.8612						
Dev. 3	0.1799	0.0420					
Dev. 4	0.0482	0.0054	0.8266				
Dev. 5	0.1178	0.0329	0.0012	0.0004			
Dev. 6	0.6037	0.2560	0.1290	0.0436	0.0210		
Dev. 7	0.0083	0.0241	0.8606	0.2614	< 0.0001	0.0423	

The distributions of *wCDI* for cells analyzed by seven different mechano-NPS devices were tested pairwise to determine if the data from each device came from equivalent distributions. A significance criterion of $\alpha = 0.05$ was adjusted for multiple comparisons (21 pairwise comparisons) by a Bonferroni method. As such, any pairwise test with a p-value less than 0.0024 indicates that the data from the two devices tested are not sampled from the same distribution.

Appendix 03: Frequencies of MCF 10A cell recovery categories measured at Site A and Site B.

Recovery category	Time range	Number of recovered cells (% recovered cells)	
		Site A	Site B
Instantaneous	$\Delta T_r = 0$ ms	1519 (77.5)	404 (64.7)
Finite	$0 < \Delta T_r < 100$ ms	262 (13.4)	149 (23.8)
Prolonged	$\Delta T_r > 100$ ms	179 (9.1)	72 (11.5)

MCF-10A cells measured with mechano-NPS at Site A and Site B were classified according to whether they recovered from deformation instantaneously ($\Delta T_r = 0$ ms), within a finite time window ($0 < \Delta T_r < 100$ ms), or had prolonged recovery ($\Delta T_r > 100$ ms).

Appendix 04: Geometric dimensions of mechano-NPS devices.

Microfluidic feature	MCF-10A devices	AP-1060 devices
Channel height	22.3 μm	12.9 μm
Inline filter pore width	22 μm	20 μm
Pore width	22 μm	13 μm
Pore length	700 μm	800 μm
Node width	85 μm	85 μm
Node length	50 μm	50 μm
Contraction segment width	10.5 μm	7.0 μm
Contraction segment length	3000 μm	2000 μm
Recovery segment length	700 μm	290 μm
Targeted strain	0.30	0.35

Appendix 05: Power analysis for wCDI and recovery time constant by mechano-NPS experimental groups.

				wCDI			Recovery time constant (ms)		
Group 1	Group 2	N_1	N_2	Power	Min. effect size	Actual effect size	Power	Min. effect size	Actual effect size
AP-1060	NB4	246	124	1.00	N/A	N/A	1.00	N/A	N/A
AP-1060	+ ATRA	246	333	0.08	0.033	0.012	0.96	N/A	N/A
AP-1060	+ ATRA + ATO	246	424	1.00	N/A	N/A	1.00	N/A	N/A
AP-1060 + ATRA	+ ATRA + ATO	333	424	1.00	N/A	N/A	1.00	N/A	N/A
NB4	+ ATRA	124	402	1.00	N/A	N/A	0.01	27.7	1.09
NB4	+ ATRA + ATO	124	419	0.03	0.049	0.014	1.00	N/A	N/A
NB4 + ATRA	+ ATRA + ATO	402	419	1.00	N/A	N/A	1.00	N/A	N/A
AP-1060	+ Colcemid	614	236	1.00	N/A	N/A	0.13	33.6	9.64
NB4	+ Colcemid	123	167	1.00	N/A	N/A	1.00	N/A	N/A
AP-1060	S-phase	268	282	1.00	N/A	N/A	1.00	N/A	N/A
AP-1060	S-phase + Colcemid	268	209	1.00	N/A	N/A	1.00	N/A	N/A
AP-1060 S-phase	S-phase + Colcemid	282	209	0.80	0.032	0.032	0.90	N/A	N/A
NB4	S-phase	341	122	0.98	N/A	N/A	0.70	62.0	55.8
NB4	S-phase + Colcemid	341	151	0.95	N/A	N/A	0.07	55.7	16.3
NB4 S-phase	S-phase + Colcemid	122	151	0.05	0.10	0.02	1.00	N/A	N/A

AP-1060 Sync + LatA	+ TSA	155	84	1.00	N/A	N/A	0.27	81.4	54.1
AP-1060 Sync + LatA	+ ATRA	155	199	1.00	N/A	N/A	0.29	52.6	29.9
AP-1060 Sync + Lat A + TSA	+ ATRA	84	199	1.00	N/A	N/A	0.11	42.2	15.2
NB4 Sync + LatA	+ TSA	75	114	0.68	0.094	0.083	0.44	55.9	38.9
NB4 Sync + LatA	+ ATRA	75	95	0.79	0.103	0.101	0.47	61.3	43.8
NB4 Sync + LatA + TSA	+ ATRA	114	95	0.09	0.058	0.019	1.00	N/A	N/A
AP-1060, CD11b-	AP-1060, CD11b+	343	191	0.99	N/A	N/A	1.00	N/A	N/A
NB4, CD11b-	NB4, CD11b+	234	212	0.99	N/A	N/A	0.25	25.2	13.4
AP-1060	+ LatA	268	327	0.05	0.023	0.002	1.00	N/A	N/A
NB4	+ LatA	341	239	0.13	0.055	0.016	0.80	38.2	38.0
NB4 DNA Low	NB4 DNA High	125	123	0.92	N/A	N/A	1.00	N/A	N/A
HL-60	+ ATRA	184	252	1.00	N/A	N/A	1.00	N/A	N/A

Post-hoc power analysis was performed on all statistical tests for mechano-NPS measurements of *wCDI* and recovery time constant. Table rows correspond to specific comparisons made between experimental Group 1 and Group 2 with respective sample sizes N_1 and N_2. Bonferroni corrections to the default significance criterion $\alpha = 0.05$ were made for experiments with multiple comparisons. For tests with statistical power equal to or less than 0.80, a minimum effect size for $\pi = 0.80$ and actual effect size are reported.